

DETERMINING ORGAN DOSES FROM COMPUTED TOMOGRAPHY SCANNERS  
USING CADAVERIC SUBJECTS

By

THOMAS M. GRIGLOCK

A DISSERTATION PRESENTED TO THE GRADUATE SCHOOL  
OF THE UNIVERSITY OF FLORIDA IN PARTIAL FULFILLMENT  
OF THE REQUIREMENTS FOR THE DEGREE OF  
DOCTOR OF PHILOSOPHY

UNIVERSITY OF FLORIDA

2012

© 2012 Thomas M. Griglock

To Angela and G

## ACKNOWLEDGEMENTS

This research project and dissertation would never have occurred without the long-term support and guidance of Dr. Manuel Arreola. The simple fact that he did not ask me to leave his office when I asked him if we could spare a few thousands of dollars to purchase cadavers is a testament to that. His knowledge, advice, and encouragement throughout my journey have been absolutely unbelievable, and I whatever I could write here could never fully express how thankful I am to have had him as my advisor. I am especially grateful for his willingness to let each of his students have a degree of freedom that fosters professional growth, personal responsibility, and enthusiasm for our work. I could not have asked for anything more.

I owe a great deal of gratitude to Dr. Lynn Rill and Dr. Libby Brateman. Both have always shown an unbelievable willingness to help with anything. Dr. Rill has always had an open door for any questions, concerns, or personal diatribes, and has played a huge part in my professional development. Dr. Brateman has served as a model for taking pride in one's work, and has shown a degree of care on both personal and professional levels that could never be equaled. They have both had a huge impact on my life, and have shown me many characteristics I will do my best to replicate.

I would also like to thank the other members of my committee: Dr. David Hintenlang, Dr. Wesley Bolch, Dr. Scott Banks, and Dr. Bruce Welt. Without their guidance, I would probably be writing this five years from now. In all seriousness, the guidance that the members of a committee provides is often undervalued, and the guidance that they have repeatedly provided caused me to focus and better define what I wanted to accomplish. Without their help, this project would never have turned out so well.

There are many people in the Radiology department that have helped me throughout my journey. Jen Sirera and Melissa Byrd have helped me gain an understanding of the “behind the scenes” work that goes on in the department. Lindsey Lavoie, BoHyun Hartmann, Monica Ghita, and Carly Williams taught me everything I know about testing radiographic equipment. You could say they are partly responsible for my future employment. In addition to that, they have always been willing to answer questions and provide insight into the graduate student experience. Ryan Fisher has proven to be a good friend and co-worker in every way imaginable, from giving research advice to meeting for a beer and talking about the job search.

Several people have directly helped me with my research. Brian Cormack, Nancy Quinn, and Lori Gravelle provided the expertise needed to perform the CT exams and give technical information beyond anything I could have expected. Their willingness to aid with this project, despite the stranger aspects of it, exemplifies their work ethic. I am truly appreciative of their efforts on my behalf.

Anna Mench and Lindsay Sinclair helped me to make the measurements that made up this project. Anna traveled outside of her comfort zone on several occasions to help me, and I am grateful for it. Performing research with cadavers consistently puts the researchers in situations they’ve never imagined, and would probably rather forget. Lindsay was consistently willing to help in any way possible, even when we found ourselves in these situations. Her demeanor, support, and ability to laugh in rough spots made her a great person to work with. There is a saying that “Friends help you move; True friends help you move bodies”. Lindsay has helped me move bodies. Dozens of times.

I need to express my thanks to the three individuals whose bodies were utilized in this project. The act of donating your body to science is a completely unselfish one, and the willingness of individuals to give themselves to a cause after death is truly awesome. They allow students, doctors, and researchers to better understand the human body and the human experience every day. To these people I will be forever grateful.

I owe special thanks to my parents for the work ethic and patience which I have been blessed (and sometimes cursed) with. They have shown me throughout my life that I could do anything I wanted, I just needed to work. I strive every day to be more like them.

Finally, Angela Griglock has accompanied me on every step of this journey. She was willing to uproot and move our lives a thousand miles because I wanted to go back to school for a Medical Physics degree, and that willingness has made a world of difference in our lives. I owe her something big once I get a real job. Every bit of this degree is as much hers as it is mine, and it would not have happened without her.

## TABLE OF CONTENTS

	<u>page</u>
ACKNOWLEDGEMENTS .....	4
LIST OF TABLES.....	10
LIST OF FIGURES.....	13
ABSTRACT .....	15
CHAPTER	
1 INTRODUCTION .....	17
1.1 Optimization of Computed Tomography .....	17
1.2 Increased Use of Computed Tomography .....	18
1.3 The Need for Accurate Organ Doses.....	20
1.4 Specific Aims .....	22
2 OVERVIEW OF COMPUTED TOMOGRAPHY .....	27
2.1 Detector Arrays.....	28
2.2 Image Acquisition.....	29
2.2.1 Axial Scanning.....	30
2.2.2 Helical Scanning.....	30
2.2.3 Volumetric Scanning.....	31
2.3 Dose Reduction Techniques.....	32
2.3.1 Angular Tube Current Modulation .....	33
2.3.2 Longitudinal (z-axis) Tube Current Modulation.....	34
2.3.3 Combined (Angular and Longitudinal) Tube Current Modulation.....	35
2.4 Implications.....	35
3 DOSE MEASUREMENT IN COMPUTED TOMOGRAPHY .....	40
3.1 Dose Indices and the Dose Length Product.....	40
3.1.1 Variations of CT Dose Index.....	41
3.1.2 Dose Length Product.....	43
3.1.3 Considerations for CTDI and Dose Length Product .....	43
3.2 Effective Dose.....	45
3.3 Organ Dose .....	48
3.3.1 Computational Phantoms .....	48
3.3.1.1 Stylized computational phantoms .....	48
3.3.1.2 Voxel computational phantoms .....	48
3.3.1.3 Comments on computational phantoms.....	49
3.3.2 Tomographic Physical Phantoms .....	50
3.3.2.1 Material composition .....	50

3.3.2.2	Comments on tomographic physical phantoms .....	51
3.3.3	Human Cadaveric Subjects .....	52
4	OPTICALLY STIMULATED LUMINESCENT DOSIMETERS .....	59
4.1	Luminescent Dosimeters .....	59
4.1.1	The Luminescence Mechanism.....	59
4.1.2	Thermoluminescent Dosimeters.....	60
4.1.3	Optically Stimulated Luminescent Dosimeters .....	61
4.2	OSL Dosimetry System.....	62
4.2.1	Previous Characterization .....	63
4.2.2	Correction Factors.....	63
5	IN-SITU MEASUREMENT METHODOLOGY.....	68
5.1	Overview.....	68
5.2	Cadaveric Subjects .....	68
5.2.1	Medical Information .....	69
5.2.1.1	Subject 1 .....	69
5.2.1.2	Subject 2.....	69
5.2.1.3	Subject 3.....	69
5.2.2	Anatomical Differences.....	70
5.2.3	Radiographic Differences .....	70
5.3	Dose Measurement.....	71
5.3.1	Dosimeters .....	71
5.3.2	Dosimeter Placement System .....	72
5.3.2.1	Concept and usage.....	72
5.3.2.2	Tube placement .....	73
5.3.2.3	Dosimeter placement verification .....	73
5.3.3	Optimization of Scanning Methodology .....	74
5.3.3.1	Number of nanoDot measurements .....	74
5.3.3.2	Number of repeat computed tomography scans .....	75
5.3.3.3	Number of repeated nanoDot readouts.....	76
6	DIRECT ORGAN DOSE MEASUREMENTS .....	80
6.1	General Information .....	80
6.1.1	CT Scanner .....	80
6.1.2	Dose Reporting .....	81
6.2	CT Protocols .....	82
6.2.1	Helical Torso Exams.....	82
6.2.1.1	Chest-Abdomen-Pelvis (CAP).....	82
6.2.1.2	Chest.....	82
6.2.1.3	Abdomen.....	83
6.2.1.4	Pelvis .....	83
6.2.1.5	Three-phase liver .....	83
6.2.2	Cardiac Exams .....	84

6.2.2.1 Helical CT Angiography .....	84
6.2.2.2 Volume CT Angiography .....	85
6.2.3 Body Perfusion Exams .....	86
6.2.3.1 Chest perfusion .....	86
6.2.3.2 Liver perfusion .....	86
6.2.3.3 Pancreas perfusion .....	87
<b>7 RESULTS AND DISCUSSION .....</b>	<b>96</b>
7.1 Radiographic Differences in Cadaveric Subjects .....	96
7.2 Optimization of Scanning Methodology.....	97
7.2.1 Number of nanoDot Measurements.....	97
7.2.2 Number of Repeat CT Scans .....	98
7.2.3 Number of Repeated nanoDot Readouts .....	99
7.2.4 Summary of Methodology Optimization.....	99
7.3 Organ Dose Measurements .....	99
7.3.1 Helical Torso Exams.....	100
7.3.1.1 Chest-Abdomen-Pelvis (CAP).....	100
7.3.1.2 Chest.....	101
7.3.1.3 Abdomen.....	102
7.3.1.4 Pelvis .....	102
7.3.1.5 Three-phase liver .....	103
7.3.1.6 Comments on helical torso exam results .....	103
7.3.2 Cardiac Exams .....	105
7.3.2.1 Helical CT Angiography (CTA).....	105
7.3.2.2 Volumetric CTA.....	106
7.3.2.3 Comments on cardiac exam results.....	107
7.3.2.4 Comparison to previous studies.....	108
7.3.3 Body Perfusion Exams .....	110
7.3.3.1 Chest perfusion.....	110
7.3.3.2 Liver perfusion .....	110
7.3.3.3 Pancreas perfusion .....	110
7.3.3.4 Comments on body perfusion exam results .....	110
<b>8 SUMMARY AND CONCLUSIONS.....</b>	<b>144</b>
8.1 Summary .....	144
8.2 Future Work.....	146
8.2.1 Benchmark for Phantoms and Simulations.....	146
8.2.2 Size-specific Dose Estimates .....	147
8.2.3 Additional Cadaveric Subjects.....	148
8.2.4 Further Analysis .....	148
8.3 Final Thoughts .....	148
<b>LIST OF REFERENCES .....</b>	<b>150</b>
<b>BIOGRAPHICAL SKETCH.....</b>	<b>156</b>

## LIST OF TABLES

<u>Table</u>	<u>page</u>
1-1 Estimated number and collective doses from radiographic procedures in the United States in 2006. ....	25
3-1 ICRP Recommendations for tissue weighting factors. ....	58
3-2 Postembalming changes on postmortem CT scans .....	58
4-1 Summary of nanoDot characterization .....	66
4-2 Energy and scatter correction factors, $C_{E,S}$ , for x-ray beams used in clinical CT exams. ....	67
4-3 The calculated f-factor as a function of HVLs .....	67
5-1 Initial location and number of tubes and nanoDots for organ dose measurements. ....	79
6-1 Scan parameters for CAP protocol in Aquilion ONE scanner. ....	88
6-2 Scan parameters for chest protocol in Aquilion ONE scanner. ....	89
6-3 Scan parameters for abdomen protocol in Aquilion ONE scanner. ....	90
6-4 Scan parameters for pelvis protocol in Aquilion ONE scanner. ....	91
6-5 Scan parameters for three phase liver protocol in Aquilion ONE scanner. ....	92
6-6 Scan parameters for helical cardiac CTA protocol in Aquilion ONE scanner. ....	93
6-7 Scan parameters for cardiac volumetric CTA protocols in Aquilion ONE scanner. ....	94
6-8 Details of volumetric chest perfusion protocol. ....	95
6-9 Details of volumetric liver perfusion protocol. ....	95
6-10 Details of volumetric pancreas perfusion protocol. ....	95
7-1 Measured Hounsfield units for live patients, phantoms, and cadaveric subjects. ....	112
7-2 Comparison of Hounsfield Units. ....	112
7-3 Comparison of right and left side organ dose measurements. ....	112
7-4 Comparison of dose measurements within same placement tube. ....	113

7-6	Comparison of dosimeter readings.....	114
7-7	Finalized location and number of tubes and nanoDots for organ dose measurements.....	117
7-8	Organ doses for CAP protocol and small subject. ....	118
7-9	Organ doses for CAP protocol and medium subject.....	118
7-10	Organ doses for CAP protocol and large subject.....	118
7-11	Organ doses for chest protocol and small subject.....	120
7-12	Organ doses for chest protocol and medium subject.....	120
7-13	Organ doses for chest protocol and large subject. ....	120
7-14	Organ doses for abdomen protocol and small subject.....	122
7-15	Organ doses for abdomen protocol and medium subject. ....	122
7-16	Organ doses for abdomen protocol and large subject. ....	123
7-17	Organ doses for pelvis protocol and small subject. ....	124
7-18	Organ doses for pelvis protocol and medium subject.....	124
7-19	Organ doses for pelvis protocol and large subject.....	124
7-20	Organ doses for three-phase liver protocol and small subject.....	126
7-21	Organ doses for three-phase liver protocol and medium subject.....	126
7-22	Organ doses for three-phase liver protocol and large subject. ....	127
7-23	Organ doses for helical CTA protocol and small subject. ....	128
7-24	Organ doses for helical CTA protocol and medium subject.....	128
7-25	Organ doses for helical CTA protocol and large subject.....	128
7-26	Organ doses for prospectively-gated CTA protocol and small subject. ....	130
7-27	Organ doses for prospectively-gated CTA protocol and medium subject. ....	130
7-28	Organ doses for prospectively-gated CTA protocol and large subject.....	131
7-29	Organ doses for cardiac functional analysis protocol without dose modulation and small subject.....	132

7-30	Organ doses for cardiac functional analysis protocol without dose modulation and medium subject. ....	132
7-31	Organ doses for cardiac functional analysis protocol without dose modulation and large subject. ....	133
7-32	Organ doses for cardiac functional analysis protocol with dose modulation and small subject. ....	134
7-33	Organ doses for cardiac functional analysis protocol with dose modulation and medium subject. ....	134
7-34	Organ doses for cardiac functional analysis protocol with dose modulation and large subject. ....	135
7-35	Comparison of organ doses (mGy) for CFA without and with dose modulation for small subject. ....	136
7-36	Organ doses (mGy) for cardiac protocols and small subject. ....	136
7-37	Organ dose (mGy) comparison for volumetric cardiac protocols. ....	137
7-38	Organ doses for chest perfusion protocol and small subject. ....	138
7-39	Organ doses for chest perfusion protocol and medium subject. ....	138
7-40	Organ doses for chest perfusion protocol and large subject. ....	139
7-41	Organ doses for liver perfusion protocol and small subject. ....	140
7-42	Organ doses for liver perfusion protocol and medium subject. ....	140
7-43	Organ doses for liver perfusion protocol and large subject. ....	141
7-44	Organ doses for pancreas perfusion protocol and small subject. ....	142
7-45	Organ doses for pancreas perfusion protocol and medium subject. ....	142
7-46	Organ doses for pancreas perfusion protocol and large subject. ....	143

## LIST OF FIGURES

<u>Figure</u>	<u>page</u>
1-1 Number of CT procedures in the United States .....	24
1-2 Annual growth rate of CT procedures in the United States.....	25
1-3 Estimated organ doses and lifetime cancer risks from typical CT scans of the head and abdomen.....	26
2-1 Difference between SDCT and MDCT .....	37
2-2 Illustration of angular tube current modulation.....	37
2-3 Illustration of longitudinal tube current modulation.....	38
2-4 Illustration of combined angular and longitudinal (x-y-z axis) tube current modulation.....	39
3-1 CTDI body phantom (left), head phantom (right) and cylindrical rods (front). ....	55
3-2 CTDI <sub>100</sub> measurement efficiency as a function of collimated beam width.....	56
3-3 General stylized (left) and voxel (right) computational phantom.....	56
3-4 Adult male tomographic physical phantom. ....	57
4-1 The basis for optically stimulated luminescence.....	66
4-2 NanoDot dosimeters with active material exposed (top left), inside case (top right), and in microStar holder (bottom). ....	66
5-1 Components of the dosimeter placement system.....	77
5-2 nanoDot dosimeters in the holder.....	77
5-3 nanoDot dosimeters and holder in place at the distal end of the placement tube. ....	78
5-4 Dosimeter placement system in use with a cadaveric subject on the CT table. .	78
5-5 Final tube positions from verification scan.....	79
6-1 Scan range for CAP protocol.....	88
6-2 Scan range for chest protocol.....	89
6-3 Scan range for abdominal protocol.....	90

6-4	Scan region for pelvis protocol. ....	91
6-5	Scan range for three phase liver protocol.....	92
6-6	Scan region for helical cardiac CTA protocol.....	93
6-7	Cardiac ECG with tube current (yellow) as a function of cardiac cycle.....	94
7-1	Organ dose versus BMI for CAP protocol.....	119
7-2	Organ dose versus BMI for chest protocol. ....	121
7-3	Organ dose versus BMI for abdomen protocol. ....	123
7-4	Organ dose versus BMI for pelvis protocol.....	125
7-5	Organ dose versus BMI for three-phase liver protocol. ....	127
7-6	Organ dose versus BMI for helical CTA protocol.....	129
7-7	Organ dose versus BMI for prospectively-gated CTA protocol.....	131
7-8	Organ dose versus BMI for cardiac functional analysis protocol without dose modulation.....	133
7-9	Organ dose versus BMI for cardiac functional analysis protocol with dose modulation.....	135
7-10	Organ dose versus BMI for chest perfusion protocol.....	139
7-11	Organ dose versus BMI for liver perfusion protocol.....	141
7-12	Organ dose versus BMI for pancreas perfusion protocol.....	143

Abstract of Dissertation Presented to the Graduate School  
of the University of Florida in Partial Fulfillment of the  
Requirements for the Degree of Doctor of Philosophy

DETERMINING ORGAN DOSES FROM COMPUTED TOMOGRAPHY SCANNERS  
USING CADAVERIC SUBJECTS

By

Thomas M Griglock

May 2012

Chair: Manuel Arreola  
Co-chair: Lynn Rill  
Major: Biomedical Engineering

The use of computed tomographic (CT) imaging has increased greatly since its inception in 1972. Technological advances have increased both the applicability of CT exams for common health problems as well as the radiation doses used to perform these exams. The increased radiation exposures have garnered much attention in the media and government agencies, and have brought about numerous attempts to quantify the amount of radiation received by patients. While the overwhelming majority of these attempts have focused on creating models of the human body (physical or computational), this research project sought to directly measure the radiation inside an actual human being.

Three female cadaveric subjects of varying sizes were used to represent live patients. Optically-stimulated luminescent (OSL) dosimeters were used to measure the radiation doses. A dosimeter placement system was developed, tested, and optimized to allow accurate and reproducible placement of the dosimeters within the cadaveric subjects. A broad-beam, 320-slice, volumetric CT scanner was utilized to perform all CT exams, including five torso exams, four cardiac exams, and three organ perfusion

exams. Organ doses ranged in magnitude from less than 1 to over 120 mGy, with the largest doses measured for perfusion imaging.

A methodology has been developed that allows fast and accurate measurement of actual organ doses resulting from CT exams. The measurements made with this methodology represent the first time CT organ doses have been directly measured within a human body. These measurements are of great importance because they allow comparison to the doses measured using previous methods, and can be used to more accurately assess the risks from CT imaging.

## CHAPTER 1 INTRODUCTION

### 1.1 Optimization of Computed Tomography

The discovery, development, and utilization of radiation to provide accurate, timely, and often life-saving medical diagnoses and treatment is without question one of the greatest achievements of the last one-hundred years. Nowhere is this success more obvious than in the realm of computed tomography (CT). CT scanners are often the workhorse in Radiology Departments, and their roles stretch from the routine (chest exam and virtual colonoscopy) to the remarkable (CT angiography and organ perfusion studies). However, this dependence on CT exams has led to an increase in both the overall number of exams and the exposure to the individual patients having those exams.<sup>1</sup> Recent publications, media reports, and even Congressional hearings have brought radiation exposures from CT exams to the attention of the general public.<sup>2,3,4,5</sup> Due to this increase in usage and widespread attention, the medical community as a whole, and the radiology and medical physics communities in-particular, have accepted renewed responsibilities in the realm of CT. These include, but are not limited to, the following: minimizing the amount of radiation exposure while maintaining diagnostic results, ensuring patient exposures do not surpass the aforementioned optimized levels once they are determined, ensuring the appropriate selection of patients undergoing CT exams, and providing practical yet accurate comparisons between radiation risks and clinical benefits. Together, these four objectives strive to optimize the usage of CT imaging throughout the medical community.

While each of these objectives may stand on their own, successful fulfillment of any singular objective relies on continued progress toward fulfilling the others. For

example, both minimizing radiation exposure and analyzing the risk-benefit ratios rely upon accurate dose measurements for common CT exams. These measurements then impact the appropriateness objective because low exposure, low risk exams could yield a larger window of applicability, while higher exposure, higher risk exams will result in more restricted application. In other words, it is impossible to satisfy one objective alone; successful implementation of any one of these four objectives should inherently lead to successful implementation of all of them. The key to this process lies in the determination of the actual risks presented by the radiation exposure during a CT exam, and accurate risk modeling depends most heavily upon accurate and reliable dosimetric measurements. It is the general purpose of this project to develop and implement a new methodology for directly measuring the doses received during a CT exam. The resulting doses that are measured with this method can be used as a point of reference for other measurements that rely upon simulations, whether they are computational or anatomical. Prior to addressing the specific goals of this work, it is imperative to first discuss the increasing importance for such measurements.

## **1.2 Increased Use of Computed Tomography**

Numerous studies have been performed over the last decade to track overall patterns of use for CT. The most widely accepted and referenced figures are collected and published annually by Information Means Value (IMV) Medical Information Division, Inc. (Des Plaines, IL). These reports analyze general medical imaging market trends, are commonly referred to as benchmarking reports, and rely on census data that IMV collects from hospitals and imaging centers nationwide.<sup>6</sup> Figure 1-1 summarizes the results of these reports, up to and including the data collected for 2006.<sup>7</sup>

The number of annual CT exams performed increased from 30.6 million in 1999 to approximately 62 million in 2006, an overall increase of nearly 77% in six years. Although there is no indication that CT usage will diminish in the coming years, it is interesting to note that the rate of increase has slowed over the last three years of the IMV Report (Figure 1-2). The average growth rate in the time period from 1999 to 2002 was 14.6% annually, while the average growth rate from 2004 to 2006 dropped to 7.4% annually. Even though more recent data has not yet been published, this analysis indicates, at the very minimum, a short-term slowing of the growth in CT usage.

Despite the possible decrease in growth, the long-term overall increase in CT usage has led to an increase in radiation exposure to patients. The National Council on Radiation Protection & Measurements Report Number 160 (NCRP 160),<sup>8</sup> *Ionizing Radiation Exposure of the Population of the United States*, states that the per capita dose from medical imaging exams (including radiography, fluoroscopy, CT, and nuclear medicine) has increased from 0.55mSv in 1980 to 3.0mSv in 2006, nearly a 6-fold increase. In addition, while this report shows that CT accounts for only 17% of all imaging procedures in the US, it accounts for 50% of the total dose (Table 1-1)<sup>9</sup>, and will most likely increase in the near future. Clearly, even though the total number of exams for all imaging modalities has increased in recent years, the immense increase in the number of CT exams is responsible for the largest portion of the overall increase in radiation dose.

This main conclusion of NCRP 160 was echoed and brought to the attention of the medical community as a whole in 2007 by Brenner and Hall.<sup>1</sup> In this study, the authors cite data from numerous sources, including the aforementioned IMV Benchmark

Reports and the most recent NEXT publication<sup>10</sup>, to break down the increase in CT scans into subsets and provide estimates for cancer risks from these exams. They report that the largest increases in CT exams have been in the areas of pediatric diagnosis and adult screening exams, such as virtual colonoscopy<sup>11</sup> and cardiac function.<sup>12</sup> In addition, Brenner and Hall report both estimated organ doses and lifetime attributable risks (LAR) of cancer mortality from these doses, the graphs of which are reproduced in Figure 1-3. It is important to recognize that these reported organ dose estimates came from a 2001 study<sup>13</sup> which relied upon dose estimates from Britain in 1991.<sup>14</sup> Thus, the numbers are essentially from a different era in CT imaging prior to the widespread implementation of helical scanning, and far before technological advancements such as multiple-detector CT (MDCT) and mA modulation.

Brenner and Hall are careful to point out that while the risk to any individual remains small, the concern comes from the small risk applied to an increasing number of people. They reference a 2004 study by Berrington *et al*<sup>15</sup>, which estimates a radiation-induced cancer level of 0.4% from the number of CT scans performed from 1991 to 1996. Using these numbers, Brenner and Hall estimate that up to 2.0% of all cancers could be attributable to the radiation from CT studies. The authors conclude their report by stating that “perhaps 20 million adults and, crucially, more than 1 million children per year in the United States are being irradiated unnecessarily.”

### **1.3 The Need for Accurate Organ Doses**

While the conclusions cited above may seem shocking, there are sensible reasons for the large increase in CT utilization. Technological advances that have been made to both increase the speed of CT image acquisition and decrease the amount of radiation needed to create the images have made CT the imaging modality of choice for a vast

number of indications and symptoms. Additionally, the simple fact that CT allows visualization of internal anatomy and physiological function has all but eliminated the practice of exploratory surgery, an advantage immediately recognized at the introduction of computed tomographic imaging.<sup>16</sup>

With all of this information readily accessible, and especially in the light of increased public awareness of the risks of radiation, the main question becomes, “At what point do the risks from CT outweigh the benefits?” Certainly, there are situations when a CT exam is warranted despite the amount of radiation exposure to the patient, such as the case of a patient presenting with signs of a stroke, in which case a Brain Perfusion CT exam would be the appropriate and most beneficial imaging exam.<sup>17</sup> Likewise, there are situations when a CT exam is not warranted, or when the radiation risk outweighs any potential benefit, as is the case for asymptomatic patients electing to undergo a whole-body CT screening exam.<sup>18</sup> However, there are numerous imaging exams where the risk-benefit analysis is not so clear-cut. It is for these cases that the Medical Physics community needs to provide guidance.

To this extent, organ dose measurements provide the most accurate and dependable metric for determining risk from a CT exam. Brenner and Hall even note that, “For risk estimation, the organ dose is the preferred quantity.”<sup>1</sup> But the methods for determining organ doses are varied, and, as discussed earlier, many studies reports doses that may be considered outdated and/or inaccurate. Both of these problems can yield conclusions that are not only misleading, but problematic in that they unintentionally bring about misconceptions in the general public about the severity of radiation risks from CT imaging.

In order to remedy these problems, organ doses that are reported and published need to not only be accurate and up-to-date, but they need to take all clinical aspects of modern CT imaging into account. With the speed at which CT technology is changing and advancing, this is a very difficult task to accomplish. However, the direct measurement of organ doses resulting from clinical CT scans would allow fulfillment of each of these goals. This is the main motivating factor for this project.

#### **1.4 Specific Aims**

The overall goal of this research project is to develop a robust methodology for directly measuring organ doses from clinical CT scans. As previously discussed, radiation doses resulting from CT scans are relevant not only due to the large number of scans being performed annually, but are also due to the increased radiation exposures from individual scans. To accomplish this goal, the following work was performed:

1. Acquisition of cadaveric subjects. Three cadavers were acquired from the Anatomical Board of the State of Florida and MedCure, Inc. (Orlando, FL). Each cadaver was embalmed, and anatomically intact so as to most closely resemble a live patient. Each cadaver varied in terms of height and weight to mimic a small, medium, and large patient.
2. Development of a system for radiation dosimeter placement within organs of interest (OIs). Radiotransparent plastic tubing was used to provide a pathway to the internal OIs. Smaller diameter, reinforced plastic tubing were used to act as holders and transporters for the optically stimulated luminescent (OSL) dosimeter “dots” within the larger diameter tubes.
3. Achievement of external access to internal organs. A radiologist with experience performing CT-guided biopsies was utilized to locate and access the internal OIs. Once the appropriate locations were accessed, the plastic tubing was inserted and fixed in position. As the dot dosimeters were placed at the sealed distal end of the tubes, fiducial markers were inserted into the tubes to verify and visualize the desired placement of the tubes and dosimeters.
4. Optimization of the scanning process. A different set of OSL dots was used to measure the doses resulting from increasing numbers of repeated chest-abdomen-pelvis (CAP) CT scans. The data was analyzed to determine the minimum number

of scans that yield the most accurate organ doses, and helped to determine the number of scans performed for every protocol.

5. Measurement of organ doses. Twelve clinical protocols were investigated to measure and associate the organ doses with the CT exams on a 320-slice scanner. An experienced CT technologist performed the scans to provide the most clinically accurate results. Patients were simulated using the cadaveric subjects, and the doses were measured with a commercially available OSL dosimetry system.
6. Comparison of organ doses. Four adult cardiac protocols (Prospectively-gated CTA, Functional Analysis with and without dose modulation, and 64-slice Cardiac CTA) have been previously investigated utilizing both MCNP5 Monte Carlo simulations and physical tomographic phantom estimates on the 320-slice scanner. These results were compared against the measurements made in this project.

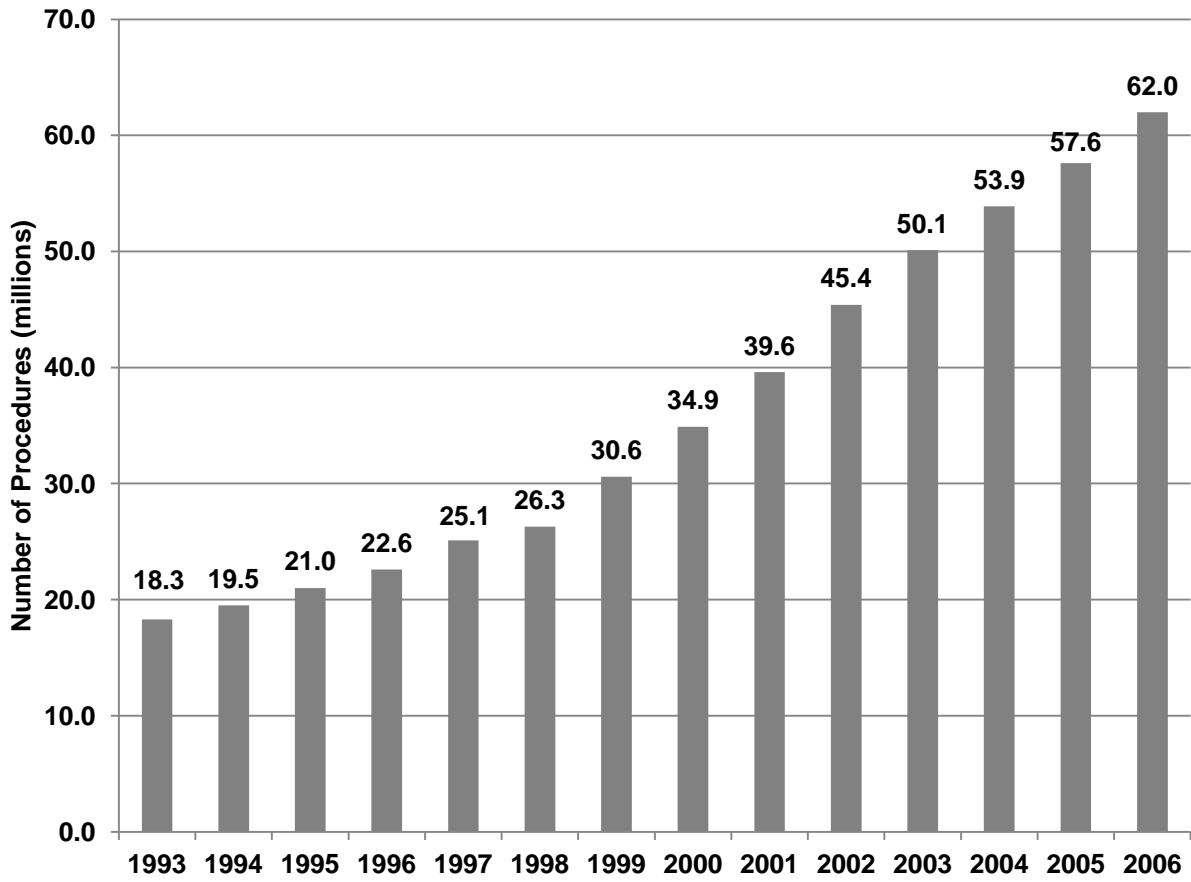


Figure 1-1. Number of CT procedures in the United States.

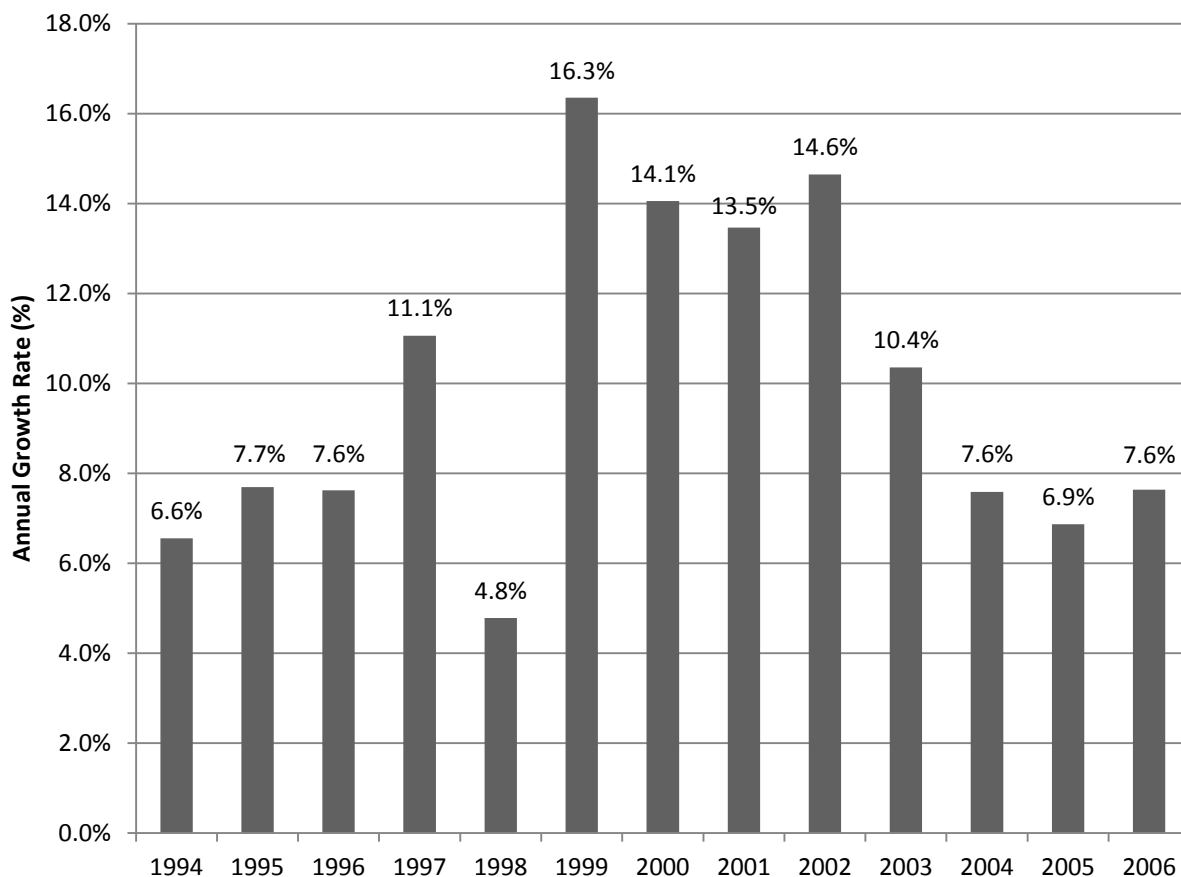


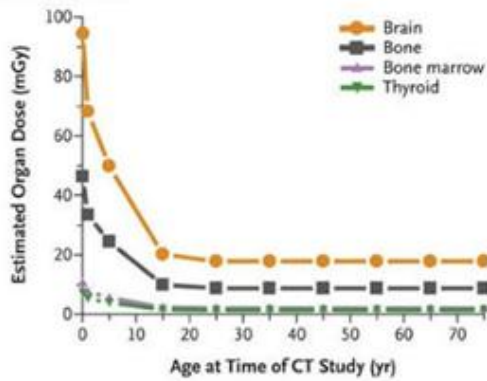
Figure 1-2. Annual growth rate of CT procedures in the United States.

Table 1-1. Estimated number and collective doses from radiographic procedures in the United States in 2006.

	Numer of Procedures (millions)	Percent of Total Procedures (%)	Collective Dose (thousand person-Sv)	Percentage of Total Collective Dose (%)
Radiography*	281	73.2%	96	10.7%
Interventional	17	4.4%	129	14.4%
CT	67	17.4%	440	49.1%
Nuclear Medicine	19	4.9%	231	25.8%

\*Dental excluded. Mammography (34.5 million) included.

A Head CT, 340 mAs



B Abdominal CT, 240 mAs

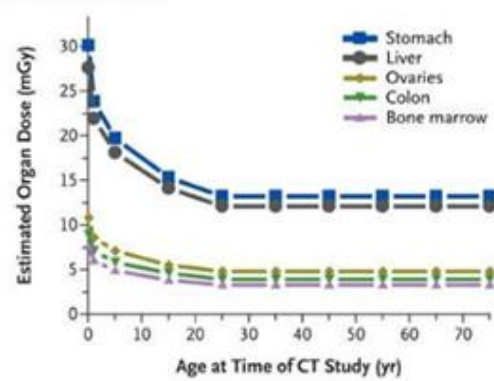


Figure 1-3. Estimated organ doses and lifetime cancer risks from typical CT scans of the head and abdomen. [Adapted from Brenner D, Elliston C, Hall E, Berdon W. Estimated risks of radiation-induced fatal cancer from pediatric CT. AJR Am J Roentgenol 2001;176:289-96.]

## CHAPTER 2 OVERVIEW OF CT

The first CT scanner, the EMI Mark 1, was built in 1972 by Godfrey Hounsfield. The initial purpose of CT was to eliminate the problems inherent in conventional planar radiography, namely the superposition of overlying anatomy that occurs when a three-dimensional object is depicted on a two-dimensional medium. CT was able to eliminate this problem by obtaining numerous individual projection images of a subject and then reconstructing the information using mathematical principles established by Radon in 1917.<sup>19</sup> The result of this work was a series of images (slices) corresponding to an axial segment of the subject being imaged. Although the individual images are still presented in two dimensions, the effect of the ordered slices (a stack) was to maintain three dimensions of information. When the subject being imaged was a patient, this technological achievement allowed radiologists to view internal anatomy in a way never before seen.

The first generation of CT scanners was known as rotate/translate scanners. These machines employed only two x-ray detectors, used pencil beam geometry, and obtained two slices for every 4.5 minutes of scanning time. By comparison, the latest generation of scanners utilize detector arrays comprised of hundreds of individual detectors, use fan beam (in x-y plane) and/or broad beam (relative to the z-axis) geometry, and are capable of obtaining up to 320 slices with only a half-second scan time. The detailed progression of CT is well documented<sup>20</sup>, and a complete history is beyond the scope of this paper. However, several of the technological advances in CT play significant roles in this research, and as such are discussed below.

## 2.1 Detector Arrays

All CT scanners can be classified as either single detector CT (SDCT) or multiple detector CT (MDCT). SDCT systems represent an earlier technology as opposed to the more advanced MDCT. The main difference between the two systems is the manner in which the detectors are arranged and used. SDCT scanners make use of a single, wide detector to capture the transmitted x-ray attenuation profiles used for image reconstruction. In this system, the slice thickness is dictated solely by the collimation, which limits the width of the x-ray beam incident on the patient. Scanners utilizing single detector configurations suffered from a lack of x-ray utilization at thinner slice thicknesses as well as poor heat-loading characteristics.

The implementation of MDCT systems proved to be a major transformation in CT imaging. As the name suggests, MDCT systems use a multiple detector array to acquire numerous slices within a single tube rotation. This is accomplished by segmenting the detector array into many individual elements in the z-dimension. With this arrangement, slice thickness is no longer controlled by beam collimation. Rather, collimation in MDCT scanners only acts to limit the overall anatomical thickness scanned per rotation. Slice thickness is determined by binning detector element rows into groups, with each group recording an average attenuation profile for that slice. For example, if each MDCT detector row is 1mm thick and the x-ray beam is collimated to 4mm wide, the scan may be performed to yield either four slices per rotation with 1mm slice thickness (called 4 x 1mm), two slices with 2mm thickness (2 x 2mm), or one slice with 4mm thickness (1 x 4mm). The differences in detector arrays, as well as the impact of collimation on slice thickness and binning of detector elements, can be seen in Figure 2-1.<sup>21</sup>

Clearly, these advancements in detector array technology allow for a greater range of scanning protocols depending on the diagnostic need of the particular CT exam. Clinically, if an exam needs to be performed quickly with lower z-axis resolution, as in the case of trauma patients, thicker slices may be obtained to speed both data acquisition and image reconstruction. On the other hand, if the radiologist requires high resolution along the z-axis, as is necessary for diagnosis of the cerebral blood vessels, thinner slices will be acquired. The downside of thin-slice scanning is that the resulting images may appear noisy when compared to thicker slices obtained with similar kVp and mAs techniques due to the lower number of photons collected per slice. The signal-to-noise ratio (SNR) may be improved for exams requiring thin slices by increasing the tube current, with the understanding that this adjustment increases the patient dose and should only be made when diagnostically necessary. This tradeoff will be discussed in more detail later in this chapter.

## **2.2 Image Acquisition**

A basic understanding of the process used to acquire the raw data necessary for CT image reconstruction is essential. In all modern CT scanners, the x-ray tube emits radiation through a given angle, creating a “fan beam” of x-rays which define the scanners’ x-y axis (also called the imaging plane), and are incident upon the anatomy to be imaged. The z-axis runs perpendicular to this plane through the midpoint of the gantry. The x-ray beam is collimated in the z-direction, limiting the extent to which the patient is exposed during each tube rotation. The x-rays that pass through anatomy unattenuated then impinge upon the detector array, where the intensity-modulated radiation profile is measured and then associated with the proper x-ray path through the patient anatomy in that imaging plane. Of course, CT relies on multiple projection

angles to reconstruct accurate anatomical maps, so the x-ray tube rotates around the patient in the imaging plane, and the detector array continually records the transmitted intensity at predetermined tube positions. The resulting data set is then processed to yield cross-sectional images of the corresponding anatomy.

### **2.2.1 Axial Scanning**

In the image acquisition process known as axial CT imaging, the tube performs one full revolution around the stationary patient. The data collected during that single revolution is used to create the image of that particular section, or axial “slice”, of the patient’s anatomy. The patient and table are then moved slightly along the z-axis, and another axial image acquisition is performed. This “step and shoot” process is repeated until the entire anatomical section of interest is imaged, and the result is a complete “stack” of axial cross-sections of the patient anatomy.

### **2.2.2 Helical Scanning**

While previous-generation CT scanners were limited to only axial scanning due to physical internal wiring restrictions, slip-ring technology brought about an advanced method of image acquisition known as helical scanning. During helical scanning, the x-ray tube rotates continuously while the patient and table are simultaneously moving along the z-axis. In this manner, the x-ray tube follows a helical path in the patient’s frame of reference, and the scanner is constantly obtaining intensity information. Helical CT represents an improvement beyond axial CT due to the elimination of the incremental patient movement and fractionated data collection, both of which result in greatly decreased scanning times with the same image quality.

The advent of helical scanning also brought about the need for a new imaging parameter to quantify how quickly the patient table is moving relative to the motion of

the x-ray tube. This quantity became known as pitch, and is defined as the ratio of the distance traveled by the table during one x-ray tube rotation to the width of the collimated x-ray beam at isocenter.<sup>20</sup> A pitch value less than unity indicates that there is some degree of scanning overlap during consecutive tube rotations. This condition is known as overscanning, and while it yields better image quality due to higher photon statistics, it also unnecessarily increases patient dose. Conversely, a pitch value greater than unity represents a situation where there is some spacing between consecutive rotations. Although this underscanning necessitates interpolation during image reconstruction, there is often no loss of diagnostic ability in the resulting images. In fact, many helical CT protocols are optimized with pitches greater than unity because they yield faster scanning times, lower patient doses, and often times decrease the amount of contrast agent necessary. For these reasons, several studies have been performed with the intention of determining the maximum pitch allowable while still maintaining accurate diagnoses.<sup>22,23,24</sup>

In addition, helical CT scanners implement multiple detector arrays, as were discussed previously. MDCT technology has advanced rather quickly in the last two decades, and the helical scanners using these detector arrays have progressed simultaneously. Multi-slice scanners have increased from four slices per rotation in 1998 to sixty-four slices per rotation in 2003. This larger z-axis coverage is possible due to increases in the number of rows in detector arrays and in the increased heat-dissipation capabilities of modern x-ray tubes.

### **2.2.3 Volumetric Scanning**

The latest generation of MDCT scanners extends the width of the x-ray beam well beyond that seen in the 64-slice scanners. These CT units are commonly referred

to as “volume CT scanners,” due to the large volume of anatomy they can image with a single rotation. At the time of this writing, the Toshiba Aquilion ONE (Toshiba America Medical Systems, Newport Beach, CA) boasts the highest scanning range. It features a 320 x 0.5mm detector array that spans 16cm in the z-direction, making it capable of creating 320 slices in a single 0.35s tube rotation.<sup>25</sup> The Aquilion ONE, along with its competing volume CT scanners, possesses the technology to image entire organs in one rotation without any patient table movement, while retaining the capability to perform all aspects of axial and helical CT scanning.

### 2.3 Dose Reduction Techniques

The inverse relationship between patient dose and image quality, particularly when quantified by either SNR or relative noise, constitutes an area of much discussion and constant tradeoffs throughout the various modalities of diagnostic imaging. The signal to noise ratio and relative noise are defined mathematically as:

$$SNR = \sqrt{N} \quad (2-1)$$

and

$$Relative\ Noise\ (\%) = \left(\frac{1}{\sqrt{N}}\right) \times 100, \quad (2-2)$$

where  $N$  represents the number of photons recorded in a single pixel or voxel.<sup>20</sup> As such, image quality increases as the number of photons incident on the detector increases. Unfortunately, patient dose exhibits a linear relationship with respect to the number of photons,  $N$ . This results in the fact that in order to double the SNR,  $N$  must be increased by a factor of four, thus quadrupling the exposure to the patient. For this reason, it is of the utmost importance that steps are taken to minimize  $N$  while keeping the SNR at a level sufficient to allow accurate diagnoses. This goal is accomplished in

different ways depending on the imaging modality involved. In general radiography, mAs is varied based on the anatomy to be imaged. In fluoroscopy, automatic brightness control (ABC) is utilized to automatically adjust the tube current to maintain a relatively constant noise level in every frame. In recent years, CT scanners have begun using two similar applications of tube current modulation that depend upon the x-ray attenuation of the anatomy.

### **2.3.1 Angular Tube Current Modulation**

In angular (x-y) tube current modulation, the current applied to the x-ray tube is sinusoidally modulated as the tube rotates around the patient.<sup>26</sup> As can be seen in Figure 2-2, there is a greater anatomical thickness in the lateral (y-axis) direction than in the anterior-posterior (x-axis) direction for an average patient. In fact, in many cases the patient anatomy is nearly twice the thickness in the lateral dimension (e.g. 15cm AP thickness versus 30cm lateral thickness). Clearly, this difference in anatomical thickness leads to a variation in photon attenuation, and the associated SNR, at different tube angles. For this reason, angular mA modulation was developed to maintain a nearly constant attenuation and SNR, regardless of the projection through the patient. This was accomplished by increasing the mA for increased patient thickness and attenuation, and decreasing the mA for projections with lower anatomical thickness and attenuation. Initial CT scanners utilizing this application would acquire a lateral and an AP projection radiograph prior to the actual CT scan. Attenuation information from these radiographs allows determination of the appropriate mA levels for the x- and y-axes, as well as the proper sinusoidal modulation between the two settings. Later scanners using angular mA modulation would eliminate the initial radiographs, shifting instead to a real-time, “online” mA modulation. In this method, the

detector would provide attenuation feedback during tube rotation, allowing for instantaneous mA modulation. Both methods result in more similar noise levels in the reconstructed images, as well as reduced patient doses. Several studies have investigated this form of angular (x-y) tube current modulation, and have shown that doses are reduced anywhere from 10%<sup>27</sup> to 40%<sup>28</sup> depending on the anatomical section being imaged with the initial modulation method. A similar study for the online mA modulation technique reported consistent dose reductions of approximately 20% for all areas of the torso.<sup>29</sup>

### **2.3.2 Longitudinal (z-axis) Tube Current Modulation**

As the name implies, longitudinal tube current modulation changes the current to the x-ray tube along the length (z-axis) of the patient, with the goal of keeping the relative noise consistent across all reconstructed images by maintaining a constant value for  $N$ . This method requires the acquisition of a pre-scan radiograph of the patient, which is used to predetermine how the mA should be modulated throughout the scan based on the changes in anatomical thickness along the z-axis. In most scanners, the operator can choose from a list of general mA values, corresponding to different relative noise levels, and the scanner will automatically modulate the current to maintain that relative noise.<sup>30</sup> An example of how the mA is varied according to patient thickness can be seen in Figure 2-3, where higher attenuating areas, such as the shoulders and hips, require a higher tube current. This method of dose reduction is especially useful in modern helical CT scans, although the extent of dose reduction varies greatly (anywhere from 18% to 58%) depending on the body section being imaged.<sup>31,32</sup>

### **2.3.3 Combined (Angular and Longitudinal) Tube Current Modulation**

It is also important to note that many CT manufacturers have combined both angular and longitudinal tube current modulation techniques to attain even larger dose reductions. This method is commonly referred to as x-y-z axis current modulation, and acts to vary the tube current based on anatomical differences both while the tube rotates around the patient (x-y axis) and as the patient and table translate through the CT gantry (z-axis). An example of how the mA varies is seen in Figure 2-4. In all cases, the scanner obtains two scout images for the z-axis modulation, but may or may not utilize online feedback for x-y axis modulation. This combined method results in dose reductions higher than either angular or longitudinal current modulation alone (anywhere from 2-3 times larger)<sup>27</sup>, and thus is generally considered the dose reduction method of choice.<sup>30</sup>

## **2.4 Implications**

The technological advancements outlined in this chapter have led to much of the increase in CT imaging discussed in Chapter 1. These improvements have led to wider applicability and better diagnostic ability for a huge number of indications, and as such have made the need for accurate dose measurement all the more important. This research project will focus on measuring organ doses from clinical CT exams performed on a Toshiba Aquilion ONE (AQ1) scanner. The ability of this unit to acquire images in axial, helical, and volumetric modes makes it appealing from both a clinical and academic point of view. It also allows straightforward comparison between doses from helical scans and those from volumetric scans. In addition, the default clinical protocols that the AQ1 uses implement Toshiba's Sure Exposure tube current modulation control, which is a combined technique, as outlined in Section 2.3.3. In this manner, the organ

doses measured in this project will provide realistic results from the latest technology as it is implemented in a clinical environment.

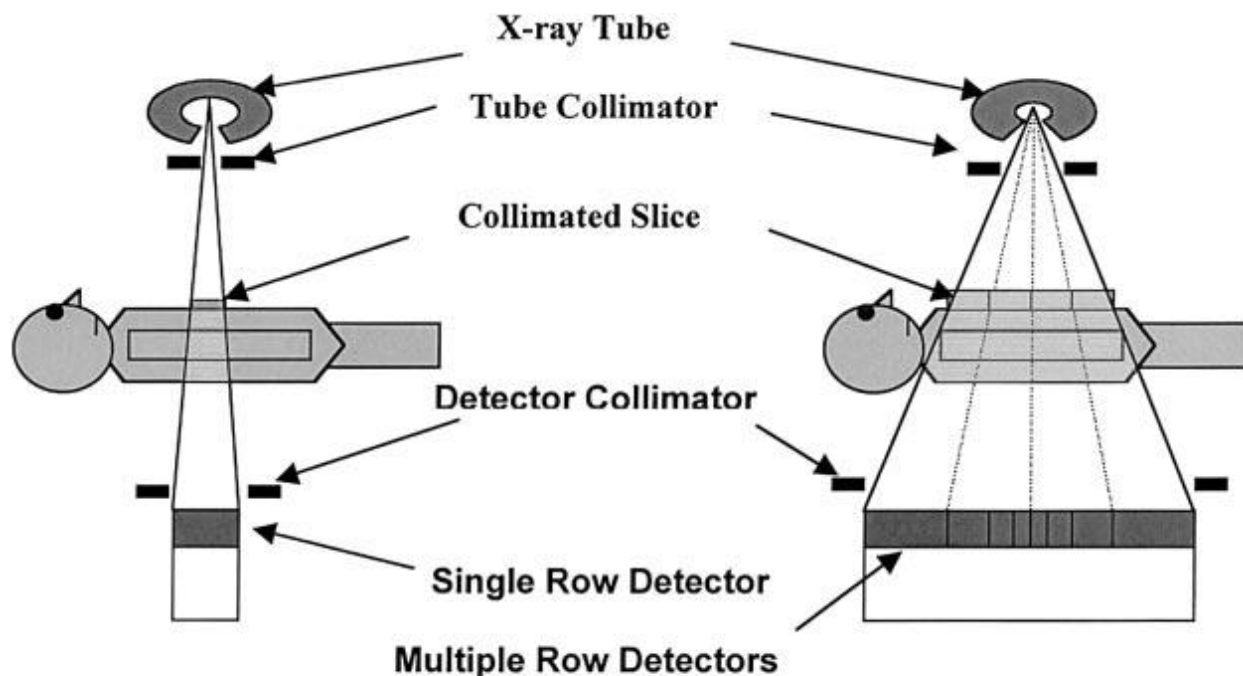


Figure 2-1. Difference between SDCT (left) and MDCT (right). [Adapted from Mahesh M. Search for isotropic resolution in CT from conventional through multiple-row detector. Radiographics 2002;22:949-62.]

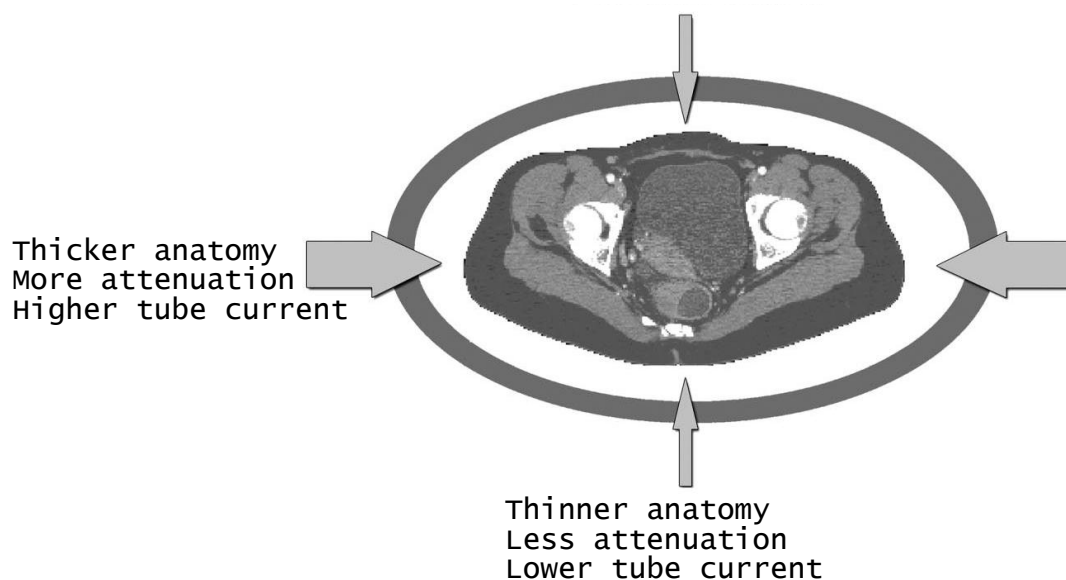


Figure 2-2. Illustration of angular tube current modulation. [Adapted from Kalra MK, Maher MM, Toth TL, et al. Techniques and applications of automatic tube current modulation for CT. Radiology 2004;233:649-57.]

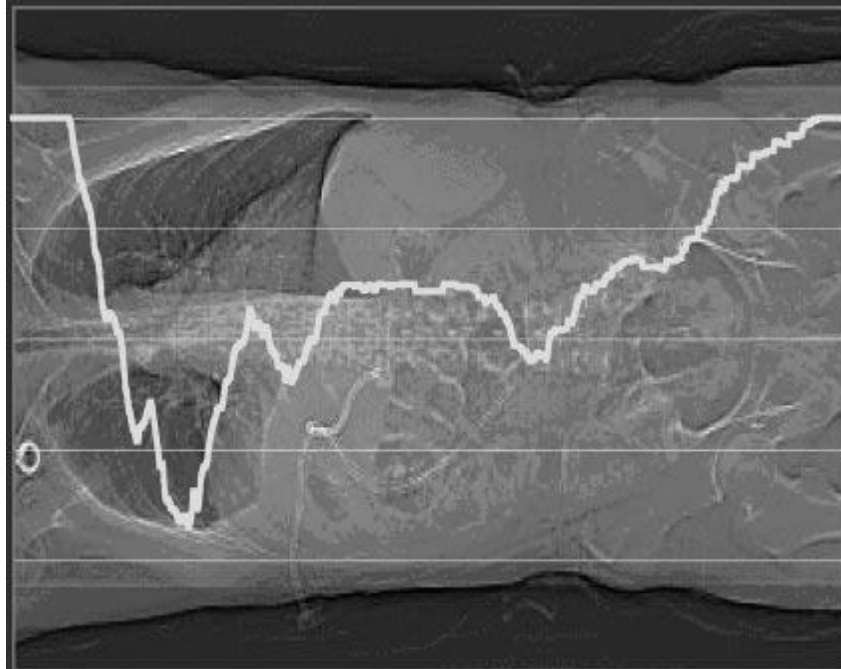


Figure 2-3. Illustration of longitudinal tube current modulation. White line illustrates relative tube current as a percentage of maximum current. [Adapted from McCollough CH, Bruesewitz MR, Kofler JM. CT dose reduction and dose management tools: overview of available options. Radiographics 2006;26:503-12.]

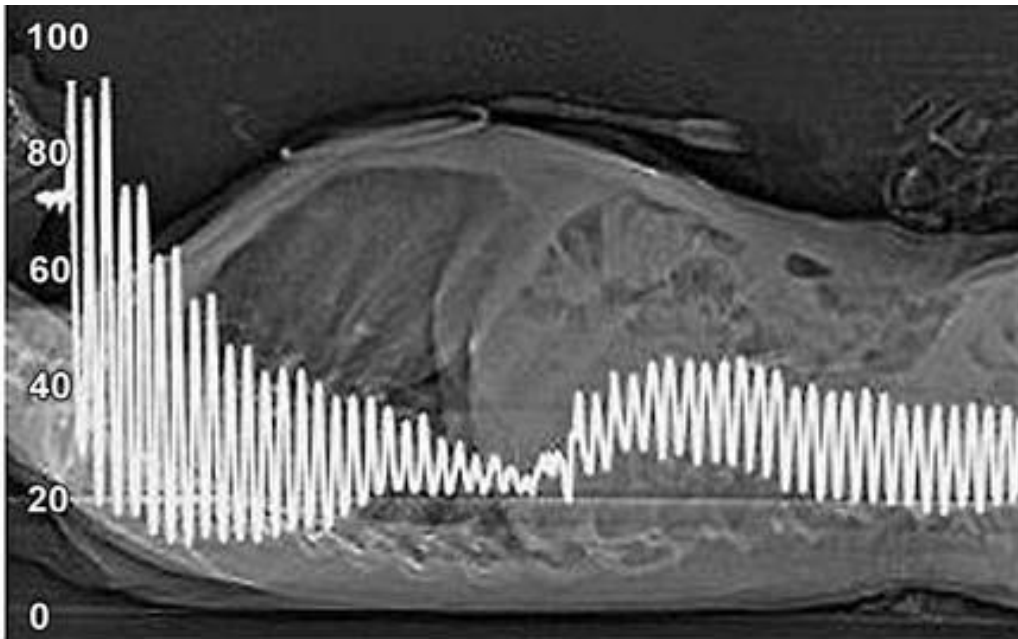


Figure 2-4. Illustration of combined angular and longitudinal (x-y-z axis) tube current modulation. White line illustrates relative tube current as a percentage of maximum current. [Adapted from McCollough CH, Bruesewitz MR, Kofler JM. CT dose reduction and dose management tools: overview of available options. Radiographics 2006;26:503-12.]

## CHAPTER 3 DOSE MEASUREMENT IN COMPUTED TOMOGRAPHY

While there is a general consensus in the medical community concerning the need to ensure that CT exams are used in a manner that minimizes the dose to the patient, the appropriate method by which to measure the radiation dose in CT is the subject of great contention. As compared to general radiographic projection imaging, in which the entrance exposure is the dose metric of choice, the standardization of CT dose reporting is difficult due to the manner in which the images are obtained. First, the x-ray beam is highly collimated during a CT scan, exposing only small anatomical regions at any given time. Second, since the x-ray tube rotates around the anatomy being exposed, the distance between the x-ray source and any patient anatomy not at the center of rotation varies during the exam. Third, several of the recent advancements in CT imaging discussed in Chapter 2, such as helical scanning, multi-slice acquisition, and mA modulation, have made it necessary to repeatedly alter and sometimes eliminate dose descriptors once thought to be sufficient. For these reasons, numerous quantities have been developed over the past three decades to attempt to best determine the dose delivered during a CT exam, with varying degrees of applicability and success.

### **3.1 Dose Indices and the Dose Length Product**

The most widely used dose descriptor for CT is the computed tomography dose index (CTDI). First defined by Shope *et al.* in 1981 for axial image acquisition, the original CTDI was defined to be “the average dose along the z-direction at the point (x, y) over the central scan of a series of scans” where the series is made up of a large number of contiguous scans.<sup>33</sup> Mathematically, this was defined as:

$$CTDI_{\infty} = \frac{1}{T} \int_{-\infty}^{\infty} D_1(z) dz \quad (3-1)$$

where T is the slice thickness and  $D_1(z)$  is the dose at (x, y) as a function of position along the z-axis for a single axial scan dose profile. In this format, the CTDI would determine the sum total of radiation exposure at a given point (x, y, z) from all axial scans along the z-axis. While the central slice scan (at which the CTDI is being determined) contributes to the CTDI because it is in the primary beam, all adjacent scans only contribute via scatter radiation, with the contributions converging to zero for more distant scans. This fact essentially equated this form of CTDI to what was known as the multiple scan average dose (MSAD), defined as “the dose to tissue that includes the dose attributable to scattered radiation emanating from all adjacent slices”.<sup>20</sup>

### 3.1.1 Variations of CTDI

Since this initial designation, numerous other forms of CTDI have been defined to make this quantity more applicable to the advancements in CT imaging. The first of these changes was introduced by the Food and Drug Administration (FDA). The new quantity was defined as:

$$CTDI_{FDA} = \frac{1}{NT} \int_{-7T}^{7T} D(z) dz, \quad (3-2)$$

where N is the number of slices obtained in the scan.<sup>34</sup> The limits of integration were changed because the previous limits of  $\pm\infty$  were not physical limits. In addition, it had been noted that the measured dose would depend upon the medium being imaged. To make measurements more consistent, the FDA also introduced two cylindrical polymethyl methacrylate (PMMA) phantoms (Figure 3-1) in which to make the measurements. Both phantoms were 14cm in length, corresponding to seven 1cm

slices in each direction from the central slice, and had a central bore for the placement of a 100mm active length pencil ionization chamber. The smaller phantom had a 16cm diameter, representing a head, while the larger phantom was 32cm in diameter, representing the torso and abdomen. These changes allowed meaningful comparisons to be made based on measurements taken from several scanners.

Due to the circular geometry of CT image acquisition, the dose profile is not uniform throughout the entire imaging field of view (iFOV). For this reason, another dose index was developed to account for differences in the dose at the periphery of the PMMA phantoms. This quantity was defined<sup>35</sup> as:

$$CTDI_W = \frac{1}{3}CTDI_{100,center} + \frac{2}{3}CTDI_{100,edge} \quad (3-3)$$

where

$$CTDI_{100} = \frac{1}{NT} \int_{-50mm}^{50mm} D(z) dz. \quad (3-4)$$

The center and edge subscripts indicate the dose measured in the center bore and the average of the doses measured in the four peripheral bores. The limits of integration for  $CTDI_{100}$  were changed to indicate the limits placed on the measurement by the 10cm length of the pencil ion chamber.

Finally, with the inception of helical CT scanning and the creation of the pitch parameter, it became necessary to define a dose index for non-contiguous image acquisition, as all previous definitions of CTDI yield the same result regardless of whether the helical scan under- or over-scanned. This new parameter was defined as:

$$CTDI_{vol} = \frac{NT}{I} \times CTDI_W = \frac{1}{pitch} \times CTDI_W, \quad (3-5)$$

where  $I$  is the table displacement per tube rotation. This formulation adjusts the CTDI measurement accordingly for scans where the slices overlap (pitch less than 1) or are not adjacent (pitch greater than 1).

### 3.1.2 Dose Length Product

All of the various CTDI measurements discussed above involve attempts to determine a normalized dose index for a single slice. None of the previously discussed CTDI definitions take the number of slices obtained during an actual CT exam into consideration. However, since clinical CT exams always involve acquisition of more than one slice, the total number of axial images acquired (which translates to the scanning range in the z-direction) has a large impact on the actual dose that a patient will receive from a given CT exam. For this reason, another quantity known as the dose length product (DLP) was developed. It is defined mathematically as:

$$DLP (mGy \cdot cm) = CTDI_{100} \times N \times T, \quad (3-6)$$

where  $N$  and  $T$  represent the number of slices acquired in a scan and the slice thickness, respectively.

### 3.1.3 Considerations for CTDI and DLP

Clearly, there are some limitations on these various parameters that justify discussion. It is a well-documented fact that  $CTDI_{FDA}$ , with the limits of integration set at seven slice thicknesses, does not account for all of the scattered radiation produced in subsequent slices.<sup>36,37</sup> In fact, the range of the scattered photons depends on their energy, and is independent of the slice thickness<sup>38</sup>, resulting in an underestimation of the dose along the central axis, especially for thinner slices.

Additionally, even for the measure used extensively at the present time,  $CTDI_{100}$ , underestimation of the dose remains a problem. Since the dose is only summed over a

total range of 100mm (the physical length of the pencil chamber used to measure the dose), any scanning or scatter beyond that extent is not taken into account. Dixon<sup>39</sup> found that, for a 20mm collimated beam width, CTDI<sub>100</sub> underestimates the central-axis dose by 20% and 10% for the body and head phantoms, respectively.

In addition, Boone<sup>40</sup> performed a study to determine the detection efficiency of CTDI<sub>100</sub>, which he defined as:

$$\varepsilon = \frac{CTDI_{100}}{CTDI_{\infty}}. \quad (3-7)$$

He utilized Monte Carlo simulations to determine both CTDI<sub>100</sub> and CTDI<sub>∞</sub> in the PMMA phantoms at increasing slice thicknesses and beam energies. Figure 3-2 shows his results for the 32cm diameter body phantom with a 120kVp x-ray beam energy. While the efficiency decreases by less than 2% for 4cm slice thicknesses, it is more surprising to note that the efficiency for thin (1mm) slices is only 88% at the periphery and 63% at the central position. With increases in the number of slices acquired per rotation, along with the much larger beam widths being used with volume CT scanners, this lack of efficiency will result in continued and vast underestimation of CT doses. These results illustrate the major problem with attempting to use any CTDI measurements as a type of dose descriptor.

While all CTDIs measure a dose index for a single slice, the DLP attempts to quantify a reference dose for an entire CT scan. Therefore, the DLP is a more clinically applicable dose index than CTDI alone. Unfortunately, it must also be realized that the problems inherent with the measurement of CTDI<sub>100</sub> are also problematic with the formulation of DLP, and represent an issue which cannot be resolved with the current methodology.

It is also worthwhile to note that both the DLP and the various CTDI values do not represent the radiation dose being given to a patient undergoing a CT exam. They represent a reference value, or a dose index, by which the radiation output during various CT scans may be compared. In this way, protocols may be optimized to yield sufficient image quality for diagnosis with minimized radiation levels. Similarly, different CT scanners may be compared based on these indices as well, so long as the measurement methodology is identical. However, these values yield no discernible information regarding the actual radiation dose to patient tissue, when defined as absorbed energy per unit mass (J/kg). More importantly, these units cannot be used to determine a radiation risk that a given CT exam represents, such as acute skin erythema or latent radiation-induced cancers. For these reasons, additional CT dose descriptors are needed.

### 3.2 Effective Dose

Throughout diagnostic radiology, the most widely used dose metric is effective dose. Despite its prevalence, the effective dose is not a directly measurable quantity. Rather, it must be calculated based on numerous other measurements of the absorbed dose to various organs and tissues, which are generally defined<sup>41</sup> as:

$$\text{Absorbed Dose} \equiv D_T = \frac{dE}{dm}. \quad (3-8)$$

By this definition the absorbed dose to any organ or tissue,  $D_T$ , is defined as the energy ( $dE$ ) deposited per unit mass ( $dm$ ) by ionizing radiation. The SI unit for absorbed dose is joules per kilogram (J/kg), also known as gray (Gy). For clarity and simplicity, the absorbed doses,  $D_T$ , will be referred to as organ doses from this point onward.

Before calculating the effective dose from organ doses, an intermediate unit known as the equivalent dose must be calculated. The equivalent dose uses various radiation weighting factors to account for differences in the biological damage done by equal quantities of different types of radiation. Mathematically, the equivalent dose can be expressed as:

$$H_T = \sum_R w_R \cdot D_{T,R}, \quad (3-9)$$

where  $w_R$  are the various radiation weighting factors defined by the International Commission on Radiological Protection (ICRP).<sup>42</sup> For the photons used in diagnostic imaging, the radiation weighting factor is 1, and therefore the magnitude of the equivalent dose and absorbed dose is the same. However, the SI unit for equivalent dose is the sievert (Sv). Consequently, for the ionizing radiations used in diagnostic imaging, 1Gy equals 1Sv.

From here, the effective dose is defined mathematically as:

$$E = \sum_T w_T \cdot H_T = \sum_T w_T \cdot \sum_R w_R \cdot D_{T,R}, \quad (3-10)$$

and since  $w_R$  equals 1 for photon radiations, this yields:

$$E = \sum_T w_T \cdot D_T, \quad (3-11)$$

which makes the effective dose for photon radiations independent of the equivalent dose conversion. Here, the  $w_T$  are known as tissue weighting factors and the  $D_T$  are the individual organ doses. The tissue weighting factors have been created with the knowledge that different tissues vary in their sensitivity to radiation. That is to say that the stochastic biological effects are more likely seen in one organ than another for an

identical absorbed dose. The tissue weighting factors attempt to quantify these relative susceptibilities, and work to define the effective dose as a risk index for various non-uniform radiation exposures. As technology advances, knowledge about tissue radiosensitivities improves as well, and the  $w_T$  values are periodically adjusted based on this information. The ICRP published the first set of tissue weighting factors in ICRP 26 (1977)<sup>43</sup>, and has revised them twice since then, in ICRP 60 (1991)<sup>42</sup> and ICRP 103 (2007).<sup>41</sup> The three sets of radiation weighting factors are seen in Table 3-1.

While some of the tissue weighting factors have been consistent over time (lungs and bone marrow), the majority have been altered to some degree, or have been added in the more recent revisions. These changes, regardless of the probability that they represent a more refined understanding of radiation risk and organ radiosensitivities, fundamentally alter the calculation of the effective dose. It is also interesting to note that different diagnostic imaging exams can result in the same effective dose. As a simplistic example, consider a Brain Perfusion CT exam resulting in 100mGy to the brain, and a basic pelvic CT resulting in 8.33mGy to the colon. According to the 2007 weighting factors each of these exams results in an effective dose of 1mSv, meaning that they theoretically pose an identical risk to the patient undergoing the exam. However, by only reporting the effective dose, the actual dose information is essentially “watered down”, and no longer gives a useful characterization of the patients’ exposure. Rather than reporting an effective dose of 1mSv, it is more accurate and relevant to report that a patient received 100mGy to the brain, or 8.33mGy to the colon. In this manner, it becomes clear that organ doses should be the dose metric of choice for CT imaging.

### **3.3 Organ Dose**

While direct in-vivo measurement of dose to the radiosensitive organs in patients undergoing CT exams is unattainable, numerous attempts at approximating these organ doses have been made and are outlined below.

#### **3.3.1 Computational Phantoms**

Many attempts at approximating organ doses from exposure to a radiation source have been made using computational anthropomorphic phantoms. This group of phantoms makes use of computer simulations (generally using Monte Carlo radiation transport algorithms)<sup>44</sup>, both of the patient and the radiation source, to model the dose distribution throughout the body. These phantoms fall into two main categories depending on how the human anatomy is modeled.

##### **3.3.1.1 Stylized computational phantoms**

The first group of phantoms is known as stylized computational phantoms. These phantoms represent the organs as various geometrical shapes and computationally model them using mathematical equations. Although these phantoms are not styled based on a particular patient, they may provide an acceptable “average” organ dose estimate. However, the generality with which the complex organ shapes are simplified (ie. the stomach as an oval or the lungs as ellipsoids) greatly limits the accuracy of the dose estimates.<sup>45</sup>

##### **3.3.1.2 Voxel computational phantoms**

The second group of phantoms is known as voxel computational phantoms. These phantoms differ from the stylized phantoms in that they are based off of either CT or magnetic resonance (MR) imaging data sets. The individual axial images are segmented to create the boundaries for certain tissues and organs, and the segmented

images are then “stacked” to form a three-dimensional voxel matrix. Within the matrix, each voxel is assigned to a particular organ with standardized composition and radiation interaction characteristics.<sup>46</sup> As such, voxellized phantoms more realistically model the shape, size, and location of patient anatomy than stylized phantoms, and are therefore thought to provide more accurate dose estimates. Figure 3-3 provides a visual comparison of stylized versus voxel phantoms.

### **3.3.1.3 Comments on computational phantoms**

While there are advantages and disadvantages to each group of computational phantoms, simulations performed with either stylized or voxellized phantoms rely upon accurately replicating the source of radiation exposure to the phantom. This task may be somewhat straightforward for certain situations, such as a nuclear medicine exam (where the radionuclide emits photons of discrete energies) or for a general x-ray exam (where the source is stationary and may be approximated by a point source). However, the radiation source for CT exams is much more complex than most situations, and any attempt to model a CT system needs to account for specific characteristics such as x-ray energy spectra, bowtie filtration, tube motion during the scans, etc.

Li *et al.*,<sup>47</sup> developed a program modeling a GE LightSpeed VCT scanner (GE Healthcare, Waukesha, WI). In order to validate this program, organ doses were measured using anthropomorphic pediatric and adult female phantoms. Comparison of these measurements to the simulations resulted in discrepancies of  $\pm 8.1\%$  for single axial scans and  $-17.2\%$  to  $13.0\%$  for helical scans. At the time of this writing, the specific details (CT exam or organ doses investigated) of Li’s study are yet to be published. It is worthwhile to note, however, that despite the reported discrepancies, which are by all means impressive, the methodology outlined in this study is only

applicable to the specific CT scanner and x-ray tube involved. Further application of this method of dose measurement using other CT units would require repeated studies on each unit in order to determine that units' specific radiation characteristics.

Numerous other studies have been performed in attempts to both more closely model CT exposures<sup>48,49</sup> and to make both types of computational phantoms more anatomically realistic when compared to the anatomy of a live patient.<sup>50,51</sup> While the methods for modeling patient anatomy have been improving greatly, the difficulty that is inherent in accurately modeling the radiation environment of a CT scan remains the main problem during simulations. It is for this reason that physical phantoms, in which measurements can be made rather than simulated, have been the subject of recent interest.

### **3.3.2 Tomographic Physical Phantoms**

Tomographic physical phantoms are phantoms constructed from materials that closely mimic the radiation characteristics of various human tissues. The phantoms are generally constructed in axial slices corresponding to the axial slices obtained from a CT exam. These slices of pseudo-human anatomy are then stacked on top of each other to construct the entire physical phantom. An example of an adult male physical phantom, constructed by a research group at the University of Florida (UF), can be seen in Figure 3-3.<sup>52</sup>

#### **3.3.2.1 Material composition**

Like computational phantoms, physical phantoms rely on image segmentation to differentiate between organs, soft tissue, and bone. Once segmented, the CT dataset slices are used to create the physical axial slices from various tissue equivalent materials. These materials have been developed and refined to closely mimic certain

characteristic coefficients (mass density, mass attenuation, and mass energy-absorption) of human bone, lung, and soft tissue at diagnostic energies.<sup>52</sup> A study by Jones *et al.*<sup>53</sup> has shown that the material coefficients of the tissue equivalent materials matches that generally accepted for the Oak Ridge National Laboratory (ORNL) computational phantom series within  $\pm 3\%$  for all three materials in the diagnostic energy range.

### **3.3.2.2 Comments on tomographic physical phantoms**

As an alternative means of estimating organ doses, tomographic physical phantoms provide a few advantages over computational phantoms. First, these phantoms allow measurement, not estimation, of doses resulting from clinical CT exams. Since the actual phantom may be placed on the CT table and scanned using a clinical scanner, the uncertainties inherent in modeling CT tube radiation output are eliminated. In this way, organ doses resulting from clinical CT exams may be measured using various types of dosimeters. Additionally, if organ doses need to be measured on several scanners, the physical phantom may simply be moved from scanner to scanner, and doses may be measured each time for comparison.

Conversely, tomographic physical phantoms also exhibit a few disadvantages compared to computational phantoms. First, the physical phantoms may not be altered once they are constructed whereas a computational phantom may continually be changed via several parameters that affect phantom size, weight, organ location, etc. Second, a physical phantom lumps all anatomic tissue into three categories: lung, bone, and soft tissue, while computational phantoms take into account not only these differences but the differences between soft tissues such as adipose tissue versus muscle tissue, liver versus kidney, etc. Third, physical phantoms need to be scanned

on an actual CT scanner. In a clinical environment, where CT units are the workhorse for radiology departments, this often creates difficulty in actually being able to use the scanners on the physical phantoms. While this may be a small disadvantage, it must be considered when comparing these two methods for measuring organ doses.

### **3.3.3 Human Cadaveric Subjects**

The above methods for attempting to determine organ doses resulting from CT exams illustrate the difficulties inherent in such a task. While models and simulations of human anatomy may provide good estimates for some clinical situations, it is clear that they are both limited in several aspects when compared to the overwhelming complexity of an actual human body. Simplifications must be made in order to construct both the computational and physical phantoms, and these simplifications necessitate a departure (of varying degrees) from anatomical accuracy.

The only definite way to obtain the most accurate organ doses to a live human patient would be to actually implant dosimeters into a patient who is undergoing a CT exam. Clearly, this is impossible from both practical and ethical considerations. However, it is possible to implant dosimeters into and scan a deceased human patient.

While there are certain postmortem changes that take place to deviate from living anatomy, an embalmed cadaver could certainly be considered more anatomically realistic than a phantom. Chew *et al.*<sup>54</sup> performed whole body CT exams on cadavers being used for the gross anatomy course taught at Wake Forest University School of Medicine. The images of 18 subjects were read by an experienced radiologist, as well as musculoskeletal and neuroradiology fellows; the reports and images were passed along with the subjects to the medical students to enhance their learning experience. The postmortem and postembalming changes to anatomy are listed in Table 3-2. The

two main major changes that may impact the organ doses measured inside a cadaver are the pleural effusions found in 16 of the 18 subjects, and also, as Chew points out, the postmortem “diffusion of water throughout soft tissues can also be expected to reduce differences in x-ray attenuation.” These soft tissue changes do represent a variation from living tissue, although the impact on dose measurements is not currently known. Additionally, although the degree of the pleural effusions varied greatly between subjects, it could be argued that this finding is not clinically uncommon, especially in elderly patients, and does not represent a major change to normal living anatomy.

While there clearly are a few definite differences between living and embalmed anatomy, the large and small scale similarities far outweigh these differences. For this reason, it is the purpose of this research project to investigate the usage of cadaveric subjects to determine organ doses from clinical CT exams. A methodology will be developed to implant radiation dosimeters inside various organs of interest (OIs) to directly measure the doses received. This methodology will need to fulfill the following criteria:

- Verification and reproducibility of dosimeter placement
- External access to internal organs
- Numerous measurement locations for larger OIs, or for any OI that is only partly irradiated in a scan
- Minimal disturbance to all anatomical structures
- Versatility of use for any cadaver and on any scanner

Appropriate fulfillment of these criteria will yield a robust methodology that will allow quick and straightforward measurements of organ doses on any CT scanner. It

will eliminate the difficulties inherent in modeling various CT x-ray tubes found in computational simulations. It will also eliminate the simplifications to anatomy found in physical phantoms. Finally, it will give past and future phantom studies benchmark measurements with which to compare their estimations.

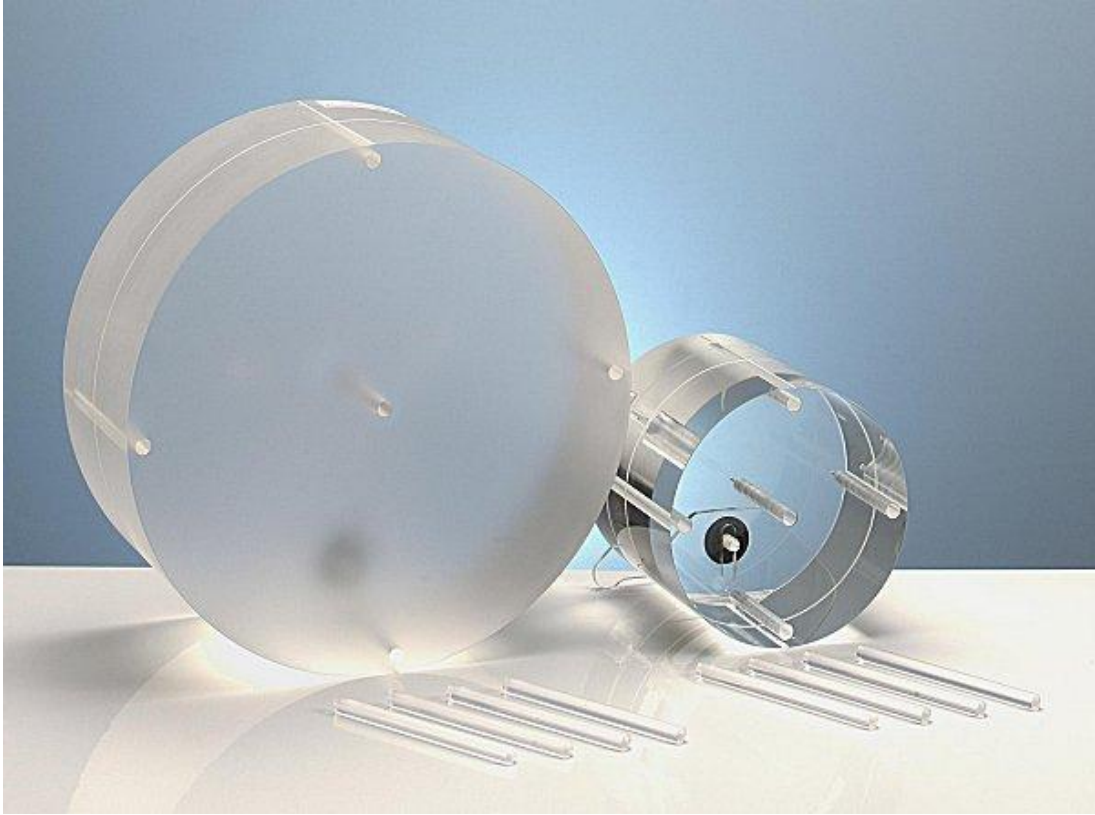


Figure 3-1. CTDI body phantom (left), head phantom (right) and cylindrical rods (front).

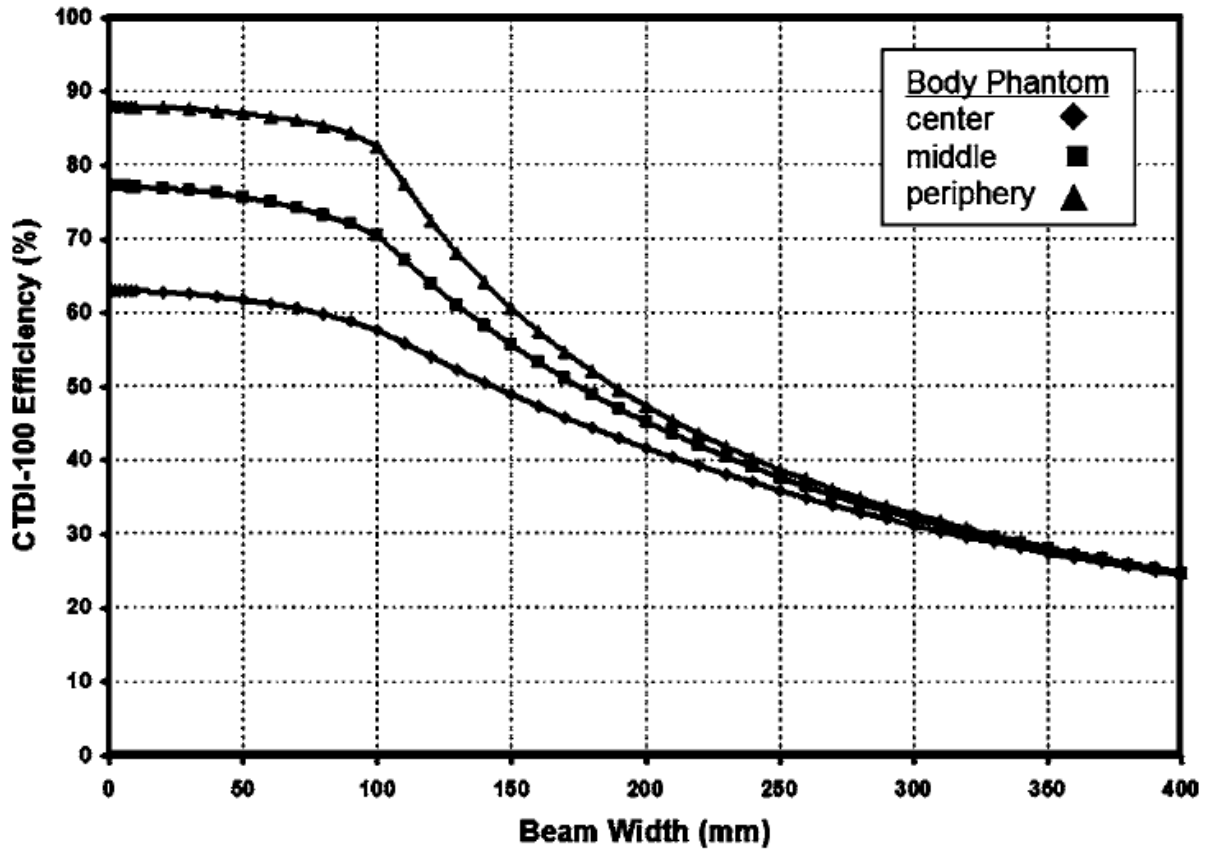


Figure 3-2. CTDI<sub>100</sub> measurement efficiency as a function of collimated beam width.

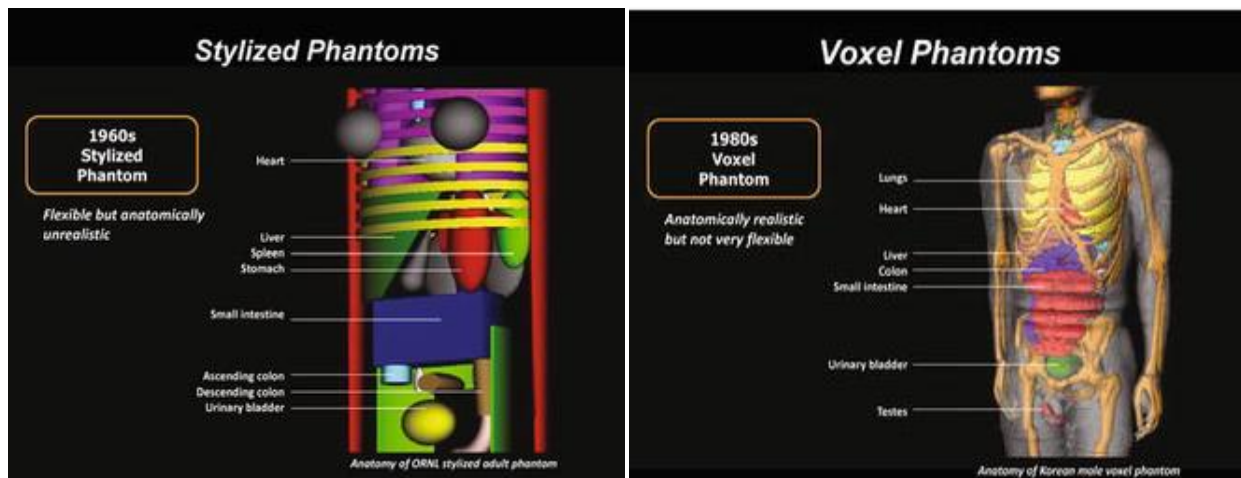


Figure 3-3. General stylized (left) and voxel (right) computational phantom. [Adapted from Bolch W, Lee C, Wayson M, Johnson P. Hybrid computational phantoms for medical dose reconstruction. Radiat Environ Biophys 2010;49:155-68.]



Figure 3-4. Adult male tomographic physical phantom.

Table 3-1. ICRP Recommendations for tissue weighting factors.

Organ/Tissue	Tissue Weighting Factor, $w_T$		
	1977	1991	2007
	<i>Publication 26</i>	<i>Publication 60</i>	<i>Publication 103</i>
Bone Surface	0.03	0.01	0.01
Bladder	--	0.05	0.04
Brain	--	--	0.01
Breast	0.15	0.05	0.12
Colon	--	0.12	0.12
Gonads	0.25	0.20	0.08
Liver	--	0.05	0.04
Lungs	0.12	0.12	0.12
Oesophagus	--	0.05	0.04
Red Bone Marrow	0.12	0.12	0.12
Salivary Glands	--	--	0.01
Skin	--	0.01	0.01
Stomach	--	0.12	0.12
Thyroid	0.03	0.05	0.04
Remainder*	0.30	0.30	0.12

\*Remainder organs changed definitions from "five most highly irradiated organs and tissues" in Publications 26 and 60 to an average dose to a list of 14 tissues in Publication 103.

Table 3-2. Postembalming changes on postmortem CT scans. [Adapted from Chew FS, Relyea-Chew A, Ochoa ER. Postmortem computed tomography of cadavers embalmed for use in teaching gross anatomy. J Comput Assist Tomogr 2006;30:949-54.]

Location	Anatomical Changes
Head	Right carotid artery cut down
Chest	Airspace filling, pleural effusions, fluid in the tracheobronchial tree
Abdomen	Free peritoneal fluid, air-fluid levels in bowel
Vascular tree	Clotted blood in heart, great vessels, and veins, hyperattenuation of aortic wall

## CHAPTER 4 OPTICALLY STIMULATED LUMINESCENT DOSIMETERS

### 4.1 Luminescent Dosimeters

Luminescence is a naturally occurring physical phenomenon in which a material releases light at relatively cold temperatures. In radiation dosimetry, two forms of luminescence have been utilized to construct radiation dosimeters: thermoluminescence (TL) and optically stimulated luminescence (OSL). Both thermoluminescent dosimeters (TLDs) and optically stimulated luminescent dosimeters (OSLDs) are constructed from inorganic materials and act as radiation dosimeters due to their crystalline lattice structure. The main difference between TLDs and OSLDs has to do with the source used to release the energy that the dosimeters trap when exposed to radiation, as described below.

#### 4.1.1 The Luminescence Mechanism

It is important to note that, from a microscopic material viewpoint, the OSL mechanism is nearly identical to the TL mechanism. An example of the general OSL or TL material structure is seen in Figure 4-1.<sup>55</sup> Basically, radiation incident on any crystalline material will impart energy to negatively charged electrons in the valence band, moving them from the valence band into the conduction band while leaving a positively charged “hole” behind. The hole will then reside in what is termed a “hole trap” that is slightly above (at higher energy level than) the valence band. Most of the excited electrons will quickly recombine with the holes and return the material to its normal ground state. However, in materials that exhibit OSL or TL, the crystalline lattice contains specific defects (either natural lattice defects or engineered through doping) which create electron traps near the conduction band. In these materials, some of the

energized electrons will move from the conduction band and get “stuck” in these traps. In this way, the number of trapped electrons provides a means to determine how much radiation exposure the material has received.

In order to actually determine how much radiation the material has received, the material, or more precisely the trapped electrons, must be “read out.” This can be done in two main ways, depending on the material structure. Basically, the trapped electrons need an additional amount of energy,  $E_a$ , to move from the trap back to the conduction band, at which point it releases a characteristic amount of energy (equal to the energy difference between conduction band and hole traps) in the form of light. This light is then captured and measured in the material “reader” and is directly proportional to the amount of radiation incident on the material.

#### **4.1.2 Thermoluminescent Dosimeters**

In the past, TLDs were widely used for dosimetry in various diagnostic and therapeutic applications.<sup>56-59</sup> The TLD materials respond to radiation as described above, resulting in a number of trapped electrons near the conduction band. In TLDs, the energy ( $E_a$ ) between the trapped electrons and conduction band is relatively small, and is provided by simply heating the material. Once the TLD material is heated to a certain point, the trapped electrons gain enough thermal energy and are elevated to the conduction band, and subsequently recombine with a trapped hole and release the excess energy in the form of an emitted photon. The photons are then read using a photomultiplier tube (PMT), and the radiation exposure may be reported.<sup>60</sup>

Despite the widespread use of TLDs, there exist numerous disadvantages concerning their applicability and ease of use for clinical CT dosimetry. TLD measurements exhibit a large dependence on x-ray beam quality, the angle of incident

radiation, and the time between irradiation and readout. In addition, TLDs display a non-linear dose response<sup>58</sup>, sensitivity to light, and each individual TLD requires a long annealing process before each use.<sup>61</sup> Finally, there are also disadvantages arising from the act of heating the material for readout, as the rate of heating greatly impacts the sensitivity of a TLD (higher heating rates yield greater loss of sensitivity), which can clearly yield a loss of accuracy in measurement. McKeever<sup>62</sup> states that the difficulties in heating a TLD in a reliable, uniform, and repeatable manner inherently flaw the TL mechanism as a radiation dose measurement option, given the ability to use other materials.

#### **4.1.3 Optically Stimulated Luminescent Dosimeters**

In recent years, OSLDs have gained more widespread usage and attention as an easy to use and accurate radiation dosimeter in a variety of clinical settings.<sup>63-67</sup> OSL materials differ from TL materials in that the OSL materials exhibit a larger  $E_a$ , and consequently require a larger amount of stimulation energy to release the trapped electrons. In OSLDs this energy is in the visible light range, and in most instances the stimulation light is provided by a light emitting diode (LED). Once stimulation occurs, the recombination, energy emission, and light detection process mirrors those used for TLDs.

Since OSLDs use an optical rather than thermal stimulus, several of the problems intrinsic to the TL mechanism are nonexistent for OSLDs.<sup>62</sup> The most common material used in the manufacture of OSLDs is carbon-doped aluminum oxide ( $Al_2O_3:C$ ). Yukihiro *et al.*<sup>66</sup> state numerous reasons for the appeal of OSL technology. Some of these reasons are: the high sensitivity of the material, the ability to read out the dosimeters very quickly and in an easily controlled and reproducible manner, and the

possibility to re-read the dosimeters since only a small amount of the trapped charges are released during a single reading.

These characteristics make OSL dosimeters a good choice for a number of dose measurement applications. The high sensitivity allows OSLDs to be smaller than most other dosimeters, and therefore allows high spatial localization of the measurements. The ability to reproduce the LED readout method gives confidence in the accuracy of OSLD measurements. The quick readout increases the number of measurements that could be made, which is extremely beneficial in both clinical and research environments. The ability to readout an OSLD numerous times without majorly depleting the stored dose information also allows for better statistical certainty in measurements, if that is required. Finally, the fact that OSLDs, like TLDs, are sensitive to visible light, allows complete erasure of the dosimeter using any visible spectrum light source. It is for all of these reasons that OSLDs were selected for use in this research project.

#### **4.2 OSL Dosimetry System**

A commercial OSL dosimetry system (microStar, Landauer, Glenwood IL) was selected for measuring doses from the CT scans investigated in this project. The microStar reader provides a means to read and report the doses measured using the corresponding OSLDs manufactured by Landauer, simply termed nanoDot dosimeters. When these dosimeters are read, the microStar reader reports the shallow dose commonly termed  $H_p(0.07)$ .<sup>68</sup> The active area of these dosimeters consists of a round 5mm-diameter disk of  $Al_2O_3:C$ . The dosimeter material is then encased within a 10mm x 10mm x 2mm light-tight black plastic case, which is marked with a two-dimensional bar code for tracking purposes. An example of these “dot” dosimeters is seen in Figure

4-2. The manufacturer specifies a radiation detection sensitivity of 0.91 and an accuracy of  $\pm 2\%$  for the screened nanoDots used in this project.<sup>69</sup> In addition, Landauer claims an energy dependence within 10% over the entire diagnostic energy range and a linear dose response up to 300cGy for the microStar reader.<sup>70</sup>

#### 4.2.1 Previous Characterization

The microStar system to be used for measurements in this project has previously been utilized for dose measurements in other research projects.<sup>48,71,72</sup> While this system had previously been extensively characterized for the high energy beams used in radiation therapy,<sup>73</sup> no such work had been done in the lower energy diagnostic range until the work performed by Lavoie.<sup>72</sup> In that study, she had investigated using nanoDots for CT dose measurements, and included assessments of dosimeter erasure, linearity and reproducibility of dose response, and angular and energy response in and out of scattering media. The results of her study, which will be used in conjunction with the measurements made in this project, are summarized in Table 4-1.

#### 4.2.2 Correction Factors

Lavoie also determined two factors necessary to convert the dose reported by the microStar reader into an actual dose to the organ or tissue in which the nanoDot was placed. The first of these factors was energy and scatter correction factors,  $C_{E,S}$ . These factors were determined by comparison of the dose reported by the nanoDots to those measured with a 0.6cc ionization chamber which had been calibrated by a National Institute of Standards and Technology (NIST) approved laboratory, as expressed by Equation 4-1:

$$C_{E,S} = \frac{\text{Raw dosimeter dose (mGy)}}{\text{Ion chamber dose to air (mGy)}} \quad (4-1)$$

Table 4-2 reports the results of this comparison, along with the resulting calibration factors. While these factors are not determined using various thicknesses of living tissue, it is a widely accepted practice to utilize PMMA to mimic the scatter and attenuation characteristics of human tissue. In utilizing these data correction factors, it must be noted that for surface measurements such as those made on the skin and eyes, the ratio reported for no acrylic will be used, as reported in the first row of Table 4-2. Similarly, for any internal measurements, the mean ratio will be utilized regardless of depth, as these ratios exhibit minimal depth dependency. This average value is reported in the bottom row of Table 4-2.

The second of these factors reported by Lavoie converts the dose to air measured by the ionization chamber into a dose to tissue. These f-factors are ratios of mass attenuation coefficients for effective energies, and are expressed explicitly as:

$$f = \frac{\left(\frac{\mu_{en}}{\rho}\right)_{tissue}}{\left(\frac{\mu_{en}}{\rho}\right)_{air}} \quad (4-2)$$

Since the attenuation coefficients are dependent upon the effective energy of the x-ray beam, Lavoie's methodology consisted of measuring the half-value layers (HVLs) for the CT scanners being investigated and converting these to effective energies using data published by Bushburg *et al.*<sup>20</sup> This data is illustrated in Table 4-3. It should be noted that, for the purposes of this research project, all of the HVL and effective energies utilized correspond to an f-factor of 1.06.

Using the energy and scatter correction factor,  $C_{E,S}$ , and the f-factor, it is possible to convert the dose reported by the microStar reader into a dose deposited in a given

tissue or organ. To do this, the raw reader dose,  $D_{raw}$ , is divided by the correction factor and multiplied by the f-factor, as expressed in Equation 4-3:

$$D_{tissue} = \frac{D_{raw}}{C_{E,S}} \times f \quad (4-3)$$

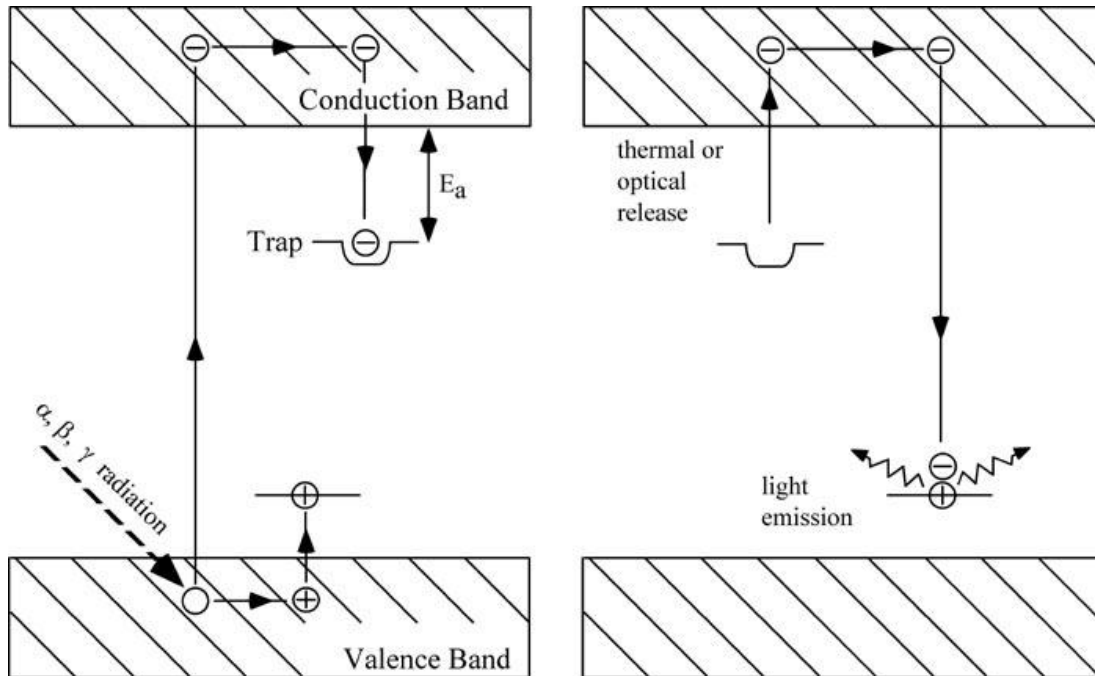


Figure 4-1. The basis for optically stimulated luminescence. [Adapted from Trapped Charge Dating. 2007. Accessed May 11, 2011, at [http://rses.anu.edu.au/research/ee/resources/index.php?p=trapped\\_charge](http://rses.anu.edu.au/research/ee/resources/index.php?p=trapped_charge).]

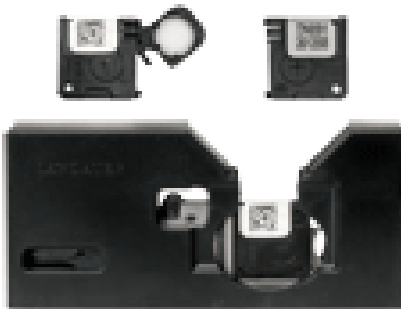


Figure 4-2. NanoDot dosimeters with active material exposed (top left), inside case (top right), and in microStar holder (bottom).

Table 4-1. Summary of nanoDot characterization.

Characteristic	Recommendation
Erasure	24 hours under fluorescent room light; "background" dose level less than 1 mGy

Linearity	Linear dose response up to 1 Gy
Reproducibility	Variation less than 2%
Angular Response	Less than 7% variation at all angles other than 90°

Table 4-2. Energy and scatter correction factors,  $C_{E,S}$ , for x-ray beams used in clinical CT exams.

Thickness of acrylic (cm)	Ratio of dose measured by nanoDot to dose measured by ionization chamber		
	80kV	100 kV	120kV
0.00	1.01	0.95	0.86
2.54	0.99	0.90	0.86
5.08	0.96	0.91	0.86
7.62	0.97	0.89	0.87
10.16	0.97	0.90	0.85
Mean	0.97	0.90	0.86

Table 4-3. The calculated f-factor as a function of HVLs. [Adapted from Lavoie, L.K. 2009. Organ dose measurements from multiple-detector computed tomography using a commercial dosimetry system and tomographic, physical phantoms. Ph.D. dissertation (Page 162, Table 10-13). University of Florida, Gainesville, Florida.]

HVL (mm Al)	Effective energy (keV)	$(\mu_{en}/\rho)_{tissue}$ (cm <sup>2</sup> /g)	$(\mu_{en}/\rho)_{air}$ (cm <sup>2</sup> /g)	f-factor
3.87	37.2	9.68E-02	9.18E-02	1.05
4.65	40.5	7.07E-02	6.69E-02	1.06
4.84	41.3	6.85E-02	6.48E-02	1.06
4.88	41.5	6.80E-02	6.44E-02	1.06
5.8	45.2	5.74E-02	5.42E-02	1.06
5.91	45.6	5.61E-02	5.30E-02	1.06
6.09	49.5	4.50E-02	4.23E-02	1.06
6.84	46.4	5.40E-02	5.09E-02	1.06
6.85	49.4	4.52E-02	4.25E-02	1.06
7.16	52.5	4.09E-02	3.84E-02	1.06
7.53	50.8	4.27E-02	4.01E-02	1.07
7.92	53.1	4.02E-02	3.77E-02	1.07

## CHAPTER 5 IN-SITU MEASUREMENT METHODOLOGY

### 5.1 Overview

The original concept for this work was fairly straightforward. It stems from the idea that the only true way to actually know for certain how much radiation a patient received from a CT exam would be to measure the doses inside the actual patient during the exam. Unfortunately, while the idea is simple, performing such in-vivo measurements are impossible. The question then became: What is the closest and most realistic representation of human anatomy that could be used to make such measurements? The answer, at least to the author, is an anatomically intact human cadaver. Obviously there have been numerous attempts at constructing phantoms (both computational and physical) for use in making these dose measurements, as outlined at length in Chapter 3. While each type of phantom has been utilized to make estimations and report the organ doses, there has never been a study to provide comparison data actually measured in-situ, or in the normal place within a human body. It is with that in mind that this research was initiated.

### 5.2 Cadaveric Subjects

Three cadaveric subjects were utilized for this project. One fully intact and embalmed cadaveric subject was obtained through the Anatomical Board of the State of Florida. Two other embalmed cadaveric subjects were obtained from MedCure (Orlando, FL), a non-transplant tissue bank that specializes in providing human tissues for medical research. The latter two subjects were embalmed torso specimens. That is, the head is removed at the C7 vertebrae, the arms are disarticulated at the shoulder, and the legs are cut mid-femur, which leaves the hip joints and proximal femur fully

intact. Although these changes represented a clear departure from a living patient, the changes made no impact on the dose measurements because none of the removed anatomy was in the primary beam during the clinical CT exams that were investigated.

## **5.2.1 Medical Information**

### **5.2.1.1 Subject 1**

Subject 1 was an embalmed female torso obtained from MedCure. The donor was 5'5" tall and had a full body weight of 100 pounds at the time of death. The cause of death was cardiorespiratory arrest at the age of 75. The donor had a history of chronic tobacco use and moderate alcohol use. She had previously undergone a minor lung resection due to lung cancer, a radical mastectomy on the left side due to breast cancer, an appendectomy, and colon surgery. She also suffered from an aortic aneurysm.

### **5.2.1.2 Subject 2**

Subject 2 was an embalmed female torso obtained from MedCure. The donor was 5'8" tall and had a full body weight of 143 pounds at the time of death. The cause of death was complications from lung cancer at the age of 75. The donor had a history of chronic tobacco use and light alcohol use. She had previously undergone a hysterectomy, and also suffered from pneumonia and dyspnea.

### **5.2.1.3 Subject 3**

Subject 3 was an embalmed, fully intact female subject obtained from the Anatomical Board of the State of Florida. The donor was 5'7" tall and had a body weight of 170 pounds at the time of death. The cause of death and any previous medical conditions were unknown (not provided by the anatomical board). No obvious medical conditions or resections were observed, and all anatomy was fully intact. For

all scans performed on this subject, the arms were placed above the head to mimic clinical patient positioning and eliminate any deviation from normal protocols.

### 5.2.2 Anatomical Differences

Cadaveric specimens differ from living tissue in several ways, arising both from postmortem and postembalming changes. These changes have been investigated at length by Chew *et al*,<sup>54</sup> and were previously discussed in section 3.3.3. Despite the two main changes that occur, pleural effusions and the diffusion of water throughout soft tissue, it is not believed that these differences have greatly impacted the organ doses measured.

### 5.2.3 Radiographic Differences

In order to quantify the extent to which the embalmed cadaveric tissues deviate from those in a living patient, a comparison between the CT images of live patients and the specimens was performed. For this comparison, the Hounsfield units (HUs) of six separate tissues were determined for CT scans performed by the Toshiba Aquilion ONE on live patients, tomographic physical phantoms, and cadaveric subjects. For consistency, the chest-abdomen-pelvis protocol was utilized with a nominal tube voltage of 120kVp with the large focal spot.

A Hounsfield unit represents the percent difference in linear attenuation coefficient between any materials and water. They are defined mathematically as:<sup>20</sup>

$$HU = \left( \frac{\mu - \mu_{H_2O}}{\mu_{H_2O}} \right) \times 1000. \quad (5-1)$$

Therefore, a change of one HU represents a change of 0.1% of the attenuation coefficient of water. To compare the live patient tissues to those of the cadavers,

equation 5-1 could be rearranged to yield the linear attenuation coefficient of tissue as a percentage of that of water. That is:

$$\mu_T = \left(1 + \frac{HU_T}{1000}\right) \times \mu_{H_2O}, \quad (5-2)$$

where  $\mu_T$  and  $HU_T$  represent the linear attenuation coefficient and Hounsfield unit of any tissue, respectively.

Hounsfield units were measured using a region of interest (ROI) tool and a CT image viewer. HUs were measured for lung, fat, muscle, bone, kidney, and liver tissue. Five sets of live patient data were gathered, along with two sets from tomographic physical phantoms, and two from cadavers. In all cases, at least three measurements were taken for each tissue type from each exam using the largest ROI possible based on the anatomical characteristics of the patient, phantom, or cadaver. Average HUs were calculated for each exam type, and the HUs for the tomographic phantom and cadaveric tissues were compared to those of live patient tissues using a percent difference calculation, i.e.:

$$\% \text{ Difference}_{\text{Cadaver}}^{\text{Lung}} = \frac{|\mu_{\text{cadaver}}^{\text{lung}} - \mu_{\text{live}}^{\text{lung}}|}{\mu_{\text{live}}^{\text{lung}}} \times 100. \quad (5-3)$$

## 5.3 Dose Measurement

### 5.3.1 Dosimeters

For the entirety of this research project, the commercially-available microStar OSL dosimetry system produced by Landauer and thoroughly characterized at diagnostic energies by Lavoie<sup>72</sup> was used. This system utilizes small (1 cm<sup>2</sup>) nanoDot screened

dosimeters to measure the radiation dose, and has been thoroughly described in Chapter 4.

### **5.3.2 Dosimeter Placement System**

In order to make repeated measurements inside the cadaver, a system to place the nanoDots needed to be developed and tested. Figure 5-1 shows the end result of numerous trials, and illustrates the general dosimeter placement system used. The system consists of three sets of plastic tubing of decreasing diameter and thickness. The outer tube is a clear 13mm inner diameter (19mm outer diameter) polyvinyl chloride (PVC) plastic tubing that has been permanently sealed at one end. It is this tube that was affixed permanently inside the cadaver, with the sealed end within the anatomy of interest and the open end outside the surface of the skin. In this manner, proper initial positioning of these PVC tubes allows external access to internal organs, a main requirement for this system. The second tube is a thin-walled white plastic straw with a 5mm diameter. The purpose of this tube is simply to reinforce the innermost tube, which serves as the nanoDot holder. The third tube is a thin-walled plastic straw with a 4mm diameter. These tubes were used to hold the nanoDots in place by overlapping the tube at the distal end and sealing off the section to allow insertion of the nanoDot. This is seen in Figure 5-2.

#### **5.3.2.1 Concept and usage**

Altogether, this dosimeter placement system works as follows. The larger PVC tube is placed inside the cadaver, with its distal (sealed) end located inside the desired organ (specifics of placement to follow). Then the nanoDot is placed in the holder of the innermost tube, and the middle reinforcement tube is slid over the smaller tube. This entire set is then inserted into the open end of the larger tube until the distal end

reaches the sealed end of the PVC tube, at which point the dosimeter is in place (Figure 5-3). In order to standardize the dose point measurement location, all holders were constructed to position the active area of the nanoDot 1cm from the distal end of the PVC tube. For the holders constructed to position more than one dosimeter, the spacing between dosimeters was set at 3cm. In this way, the dosimeter placement system fulfills the requirement for reproducible positioning of all nanoDots. Figure 5-4 shows this system being used with a cadaver.

### **5.3.2.2 Tube placement**

Prior to placing the actual tubes in the cadaver, consideration of which organ doses would be measured was necessary. In addition to measuring doses to the most radiosensitive organs, it was also deemed necessary to measure dose to those organs that may experience deterministic biological effects, such as the eyes and skin. A summary of the initial location and number of tubes and dosimeters places is found in Table 5-1.

A radiologist with experience performing CT-guided biopsies was recruited to perform the tube placement. Care was taken to minimize the size of the incisions and the impact on nearby anatomy. In order to eliminate the possibility of x-ray photons passing down the placement tubes and hitting the dosimeters unattenuated, all tubes were placed non-axially whenever possible.

### **5.3.2.3 Dosimeter placement verification**

Once all tubes were positioned where desired, a set of verification tubes were inserted into each placement tube. The verification set consisted of the nanoDot holders with 2mm metal fiducial markers in place of the dosimeters. A whole body CT scan was then performed, which allowed visualization of the placement tubes and

measurement points. If any of the tube positions were not acceptable, the tube was repositioned and another verification scan was performed. This was repeated twice, until all tubes and measurement locations were deemed acceptable. Figure 5-5 demonstrates the final positions of placement tubes, as seen from the final verification scan.

### **5.3.3 Optimization of Scanning Methodology**

Since numerous CT exams were to be investigated for this project, it was necessary to initially work to optimize the scanning, measurement, and nanoDot readout methodology. This optimization consisted of three separate components as outlined below.

#### **5.3.3.1 Number of nanoDot measurements**

To maximize the number of CT protocols investigated, it was necessary to determine the minimum number of dosimeter measurements per protocol that would still yield sufficient organ dose data. This required two separate analyses. First, for organs that appear in pairs (i.e., lungs, breasts, gonads, etc), it was desirable to investigate the dose differences in the right side versus the left side. For example, if for a given exam the doses to the individual sides are within  $\pm 5\%$  of each other, then it could be argued that measurements would need to only be made on one side. Secondly, for larger organs, such as the stomach and liver, it was of interest to investigate the difference between dosimeters that were located in the same tube, but placed 3cm apart in the holders. Once again, if the reported doses from neighboring nanoDots were within 0.5mGy, it would be reasonable to decrease the number of measurements because the dose gradients within those organs are low.

A total of 47 nanoDot dosimeters were positioned on and in the cadaver using the dosimeter placement system previously described. The Toshiba Aquilion ONE 320-slice CT scanner was used to perform a series of three consecutive chest-abdomen-pelvis (CAP) exams, each with a set of scout images, as this would irradiate nearly all dosimeters with the primary beam. Once all three exams were completed, the dosimeters were removed from their tubes and holders and read out using the microStar reader.

Each nanoDot was read three consecutive times, following the procedure set by Lavoie, and each readout was corrected for 0.2% signal depletion. The average was then calculated. The appropriate scatter and energy correction factors (Table 4-2) and f-factors (Table 4-3) were also applied. Finally, all doses were divided by 3 to give the organ dose per CAP exam.

### **5.3.3.2 Number of repeat CT scans**

In line with minimizing the number of dosimeters used per scan, it was also necessary to determine the minimum number of repeat scans that were needed to obtain a reliable “average” dose. Clearly, if a given exam is repeated 10 times, the doses reported would be more accurate in relation to the “true” doses, as opposed to only performing a single exam. Therefore, it is advantageous to determine how many scans are necessary to approach that “true” dose.

To accomplish this, the chest-abdomen-pelvis (CAP) protocol was selected once again because it would place nearly all dosimeters in the primary beam, and it is a commonly-used clinical procedure. The procedure was simplified by using four different sets of 15 nanoDots, each placed in 7 different organs, and exposed to 1, 2, 3, and 5

complete CAP exams. Once all scans were completed, all dosimeters were readout three times and corrected exactly as outlined in the previous section.

### **5.3.3.3 Number of repeated nanoDot readouts**

The final step in optimizing the scanning methodology used in this project was to investigate the number of times it was necessary to read out the nanoDot dosimeters following an exposure. Similar to the argument for repeated CT scans, it is reasonable to believe that an increased number of readouts would yield a better average reported dose, once the correction is made for signal depletion. Previous studies utilizing the microStar reader and nanoDots<sup>71,72</sup> implemented a methodology involving three reads per dot, although no formal investigation into what impact this made had been performed.

To determine the extent to which additional readouts improve the accuracy of dose measurements, 95 nanoDots were selected from those exposed during the research described in the previous two sections. The microStar data that was reported was then analyzed in two separate ways. All dosimeters were read three times, but in one instance only the first dose reported was taken. After this, the data from all three readouts was analyzed, each subsequent reading was adjusted for signal depletion, and the three reading average was taken. For each dosimeter, the percent difference between the doses for a single reading and three readings was calculated.



Figure 5-1. Components of the dosimeter placement system. From top: PVC placement tube, nanoDot holder and reinforcement tube, nanoDot dosimeters.

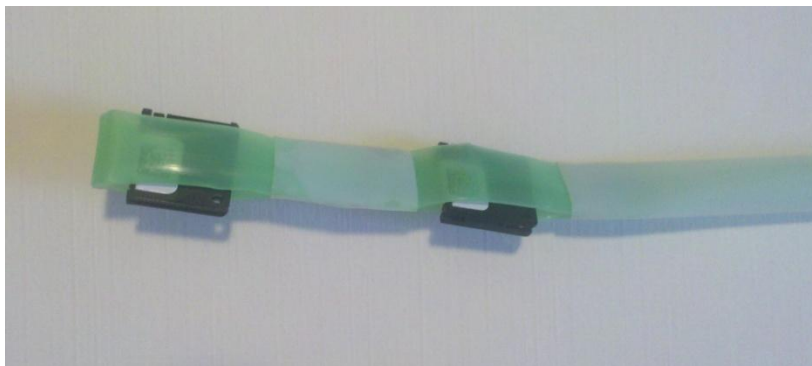


Figure 5-2. nanoDot dosimeters in the holder.



Figure 5-3. nanoDot dosimeters and holder in place at the distal end of the placement tube.



Figure 5-4. Dosimeter placement system in use with a cadaveric subject on the CT table.

Table 5-1. Initial location and number of tubes and nanoDots for organ dose measurements.

Organ	Number of Tubes	Number of Dosimeters
Breast	4	6
Breast - Skin	--	10
Colon	2	2
Eyes	--	2
Liver	3	6
Lung	4	8
Ovaries	2	2
Skin - central scan axis	--	3
Skin - surface*	--	3
Small Intestine	1	1
Stomach	1	2
Thyroid	2	2

\*For each scan, a dosimeter was placed on the skin at a position on the chest, abdomen, and pelvis.

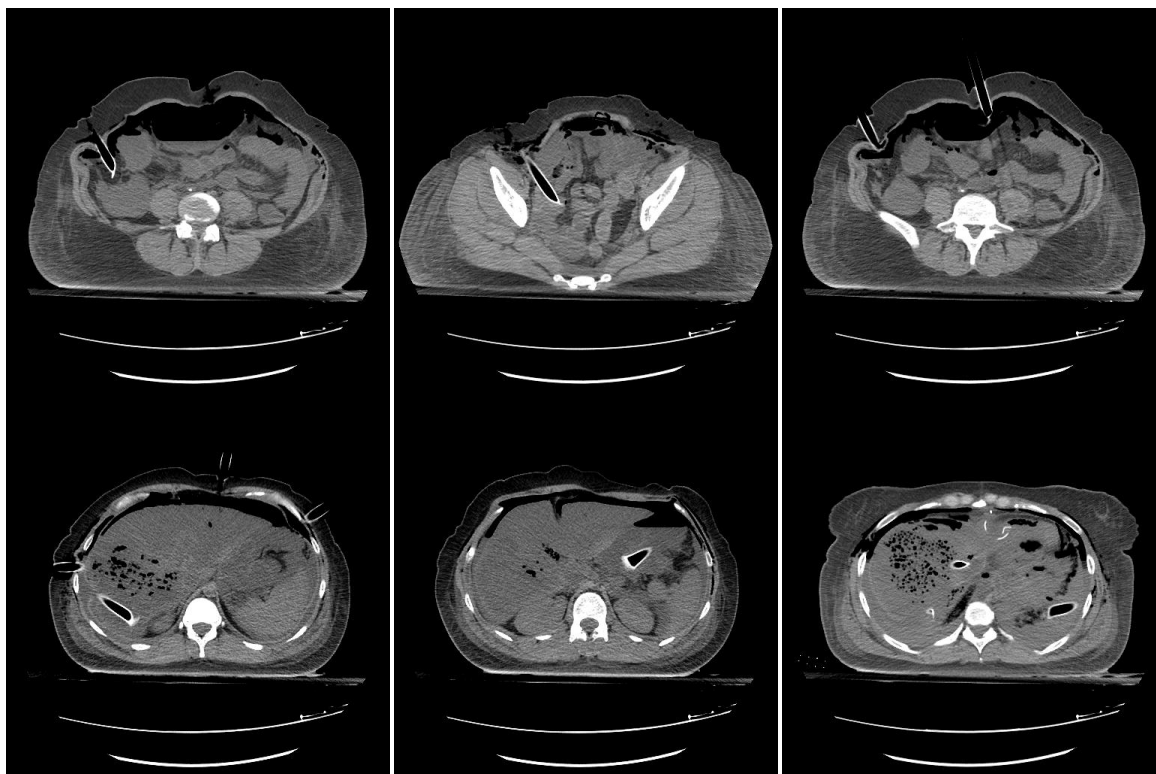


Figure 5-5. Final tube positions. Organ doses being measured, from upper right to lower left: ascending colon, right ovary, small intestine, right lower lobe of the liver, stomach, left lower lobe of the lung and left upper

## CHAPTER 6 DIRECT ORGAN DOSE MEASUREMENTS

The purpose of this chapter is to provide the details, both clinical and technical, of all CT protocols investigated during this research project. While it was not the goal of this project to determine the organ doses from every clinical CT protocol (which would be well over one hundred), it also was not the goal to investigate only one or two protocols. The goal was to develop a robust methodology that enables relatively efficient and accurate organ dose measurements that could be utilized regardless of the type of protocol selected. For this reason, twelve separate protocols were chosen and split into four main groups. The protocols, groupings, and reasons for selection are outlined below.

### **6.1 General Information**

#### **6.1.1 CT Scanner**

All protocols investigated during the course of this study were performed on a Toshiba Aquilion ONE 320-slice CT scanner (AQ1). This selection was made for numerous reasons. First among these is the ability of the AQ1 to perform image acquisitions in both helical and volume modes. This increases the number of protocols able to be investigated, and allows research to be done on the most clinically advanced perfusion protocols. Second, the AQ1 represents a state-of-the-art CT unit which has created much clinical and academic interest from the viewpoint of what it is capable of (i.e., the aforementioned organ perfusion studies) and from the concern of increased doses corresponding to increased scanning ranges. Third, previous research has been performed with this unit that allowed organ dose comparisons between the results of this project to those obtained with both physical and computational phantoms, direct

comparisons that have not been possible before. All of these reasons made the AQ1 the clear choice for the purposes of this project.

### **6.1.2 Dose Reporting**

The nanoDot dosimeters, described in Chapter 4, were used to make all organ dose measurements utilizing the methodology described in Chapter 5. Placement of all dosimeters was made using the previously described dosimeter placement system. The methodology was optimized to allow investigation of the maximum number of protocols, and the results of this optimization, along with the final dosimeter placement locations, are reported in section 7.2.

All CT exams were performed by an experienced CT technologist to provide the most accurate and realistic imaging environment. For all scans, the subject was placed on the CT table, the dosimeters were positioned in and on the subject, and the CT exam (including two localizing “scout” images) was performed. The nanoDot dosimeters were read, and the reported organ doses resulting from each protocol were separated into maximum, minimum, and average dose for each organ or tissue. The maximum dose provides a more conservative figure, and can be used to typify a “worst case” scenario. The average dose provides a more realistic “whole organ” dose, while the minimum dose is included to illustrate the variation in exposure across an organ. In addition, the standard deviation of measurements was calculated for all organs containing more than one dosimeter. For organs experiencing only partial primary-beam irradiation, an additional standard deviation was calculated using only the measurements from dosimeters in the primary beam.

## **6.2 CT Protocols**

### **6.2.1 Helical Torso Exams**

This group consists of five separate protocols: chest-abdomen-pelvis (CAP), individual chest, abdomen, and pelvis, and a three-phase liver exam. These protocols were selected simply because they are extremely common protocols throughout diagnostic CT imaging. The scanning techniques utilized in the first four standard protocols are also common to other protocols (i.e., body trauma, various CTAs, acute GI bleed, etc); therefore, obtaining general organ dose data for the torso protocols would yield information that is applicable to other protocols as well.

The three-phase liver protocol was selected for two main reasons. First, it is used for a wide variety of indications, such as cirrhosis, liver masses, and viability of transplants, which makes it a relatively commonly used protocol. Second, the fact that it requires three repeated scans of the same anatomy yields higher doses to the organs in the primary beam.

#### **6.2.1.1 Chest-Abdomen-Pelvis (CAP)**

The chest-abdomen-pelvis (CAP) protocol is utilized for numerous indications, including lymphoma, fever of unknown origination, colorectal cancer, etc. The scan begins at the thoracic inlet and terminates at the lesser trochanter (Figure 6-1), resulting in the irradiation of nearly all major internal organs by the primary beam. The scan parameters for the CAP protocol are listed in Table 6-1.

#### **6.2.1.2 Chest**

The chest protocol is mainly utilized to evaluate anatomical abnormalities or malignancies in the lungs or thoracic vasculature. The scan begins at the thoracic inlet

and terminates at the top of the kidneys (Figure 6-2). The scan parameters for the chest protocol are listed in Table 6-2.

#### **6.2.1.3 Abdomen**

The abdomen protocol is used for many indications, ranging from general abdominal pain to abscess evaluation and postoperative follow-ups. The scan begins at the diaphragm and terminates at the iliac crests (Figure 6-3). The scan parameters for the abdomen protocol are listed in Table 6-3.

#### **6.2.1.4 Pelvis**

The pelvis protocol is primarily used for masses, cysts, or inflammation in the pelvic region. The scan begins at the iliac crests and terminates at the lesser trochanter (Figure 6-4). The scan parameters for the pelvis protocol are listed in Table 6-4.

#### **6.2.1.5 Three-phase liver**

The three-phase liver protocol is used mainly to evaluate liver masses or liver function, both in patients with various liver diseases or in candidates for transplantation. The exam consists of three different scans utilizing a contrast solution, all beginning at the dome of the diaphragm and terminating at the iliac crests (Figure 6-5).

The first scan produces images with the contrast in the arterial phase, and utilizes a bolus-tracking trigger to begin the scan when a predetermined concentration of contrast arrives in the aorta. This normally occurs approximately five seconds after the scan begins, and although no contrast media was utilized with the cadaveric subjects, a five second delay was employed to mimic the clinical exam. The second scan produces images with the contrast in the venous phase, and begins seventy seconds after injection. The third phase, known as the equilibrium phase, begins three minutes after injection and produces images after most of the contrast has left the liver

and vasculature. The scan parameters are constant for all three phases, and are listed in Table 6-5.

## **6.2.2 Cardiac Exams**

One of the main rationales for the implementation of broad-beam volume CT scanners is their ability to image entire organs very rapidly, often within one rotation of the x-ray tube. Since cardiac motion often degrades image quality in conventional helical CT, the ability to greatly decrease imaging time has a large impact in this area. For this reason, four cardiac studies were selected for investigation. These include: helical cardiac CT angiography (CTA), prospectively-gated CTA, and functional analysis with and without dose modulation. The helical exam was selected to provide comparison between it and the more technologically advanced volume scans. The latter three cardiac volume exams were selected because organ dose data has previously been published for studies performed utilizing tomographic physical phantoms<sup>72</sup> and computational phantoms with MCNP code.<sup>48</sup> In this manner, the organ dose data measured in this study will be directly comparable to that previously published.

### **6.2.2.1 Helical CTA**

Helical cardiac CT angiography is a general term for a CT protocol that utilizes contrast material to produce images of the heart and surrounding blood vessels. It is mainly utilized to evaluate patients with coronary artery disease (CAD) or mild chest pain, although it can be used to visualize anatomy prior to surgery. A cardiac CTA normally begins 2 cm above the carina and terminates 2 cm below the bottom of the heart (Figure 6-6). The scan parameters for a helical cardiac CTA protocol are listed in Table 6-6. Additionally, because contrast material is used to visualize the cardiac

anatomy, bolus-tracking is utilized to trigger clinical exams. For the purposes of this project, a five second tracking delay was utilized to mirror the clinical scenario.

#### **6.2.2.2 Volume CTA**

The Aquilion ONE utilizes three basic volume acquisition protocols for cardiac CTA studies: prospectively gated cardiac, cardiac functional analysis, and cardiac functional analysis with dose modulation. While all three protocols utilize electrocardiogram (ECG) gating, the manner and timing by which they acquire images differs, as can be seen in Figure 6-7.<sup>72</sup>

When it is necessary to obtain images concerning cardiac function, information may be obtained throughout the entire cardiac cycle using the cardiac functional analysis (CFA) protocol with or without dose modulation. Both of these protocols allow image reconstruction at any point during the cardiac cycle, but the CFA with dose modulation reduces dose to the patient by decreasing the tube current throughout the cardiac cycle, only briefly increasing the current prior to the QRS complex, as illustrated in Figure 6-7B. For the prospectively gated CTA protocol, functional (time-varying) information is not obtained, and for heart rates below 65 beats per minute (bpm) the exam may be completed with a single 0.35 second exposure obtained prior to the QRS complex, when the heart is filled with contrast-enhanced blood (Figure 6-7C).

For each of these cardiac protocols, the range of the volume acquisition is 16cm wide and is placed to include images from the carina through the bottom of the heart, similar to that for helical cardiac CTAs and seen in Figure 6-6. The scan parameters for these volume CTA protocols are listed in Table 6-7. Since these protocols are gated based on ECG information, an electrical pulse generator was utilized to imitate a 60bpm heart rate.

### **6.2.3 Body Perfusion Exams**

Perfusion imaging refers to the ability of imaging technologies to provide images of blood flow, volume, and permeability throughout various organ systems. The broad beam technology described in Chapter 2 has made perfusion CT imaging more widely accepted, and has exponentially increased interest in its applicability, most notably in cancer treatment and tracking.<sup>74-78</sup> Currently, the AQ1 scanners installed at Shands Hospital at the University of Florida (SUF) have three separate body perfusion protocols programmed: chest, liver, and pancreas. Because these protocols require multiple scans over the same anatomy, they may deliver high doses to the anatomy in the primary beam. For this reason, these protocols were chosen for investigation.

Each of the three perfusion scans utilizes the AQ1's volumetric scanning capability. As such, each scan uses the large focal spot, large field of view, an acquisition thickness of 0.5 mm x 360 slices, and a total scanning range of 16 cm. Prior to beginning a perfusion scan, the 16cm range is centered over the organ being imaged, with care taken to include the superior and inferior portions of each organ.

#### **6.2.3.1 Chest perfusion**

The details of the chest perfusion protocol are listed in Table 6-8. This protocol consists of 31 separate volume acquisitions obtained at various time intervals throughout the arterial and venous contrast phases. The DLP for all subjects was 1522.1 mGy·cm.

#### **6.2.3.2 Liver perfusion**

The details of the liver perfusion protocol are listed in Table 6-9. This protocol consists of 27 separate volume acquisitions obtained at various time intervals

throughout the arterial and venous contrast phases. The DLP for all subjects was 1696.2 mGy·cm.

### **6.2.3.3 Pancreas perfusion**

The details of the pancreas perfusion protocol are listed in Table 6-10. This protocol consists of 19 separate volume acquisitions obtained at various time intervals throughout the arterial and venous contrast phases. The DLP for all subjects was 1182.2 mGy·cm.

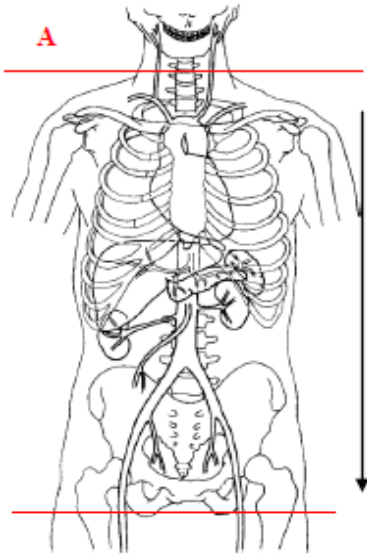


Figure 6-1. Scan range for CAP protocol.

Table 6-1. Scan parameters for CAP protocol in Aquilion ONE scanner.

Scan Parameter	
Nominal Tube Voltage	120 kV
Tube Rotation Time	0.5 sec
Helical Pitch	0.828
Acquisition Thickness	0.5 mm x 64
Focal Spot	Large
Filter	Medium - M
Scan Range (mm)*	620, 745, 700
Effective mAs*	173, 292, 332
DLP (mGy·cm)	628, 1185.7, 1790.2

\*Scan range and effective mAs vary based on patient anatomy. Numbers reported for these factors are reported as Subject 1, Subject 2, Subject 3.

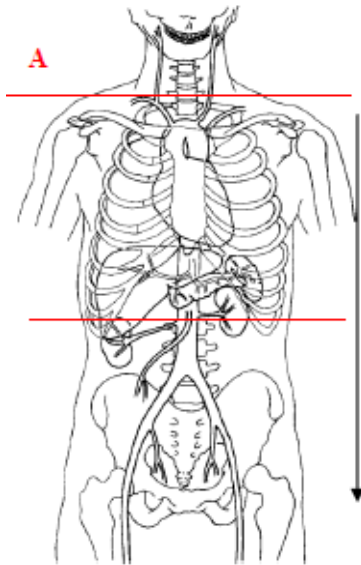


Figure 6-2. Scan range for chest protocol.

Table 6-2. Scan parameters for chest protocol in Aquilion ONE scanner.

Scan Parameter	
Nominal Tube Voltage	120 kV
Tube Rotation Time	0.5 sec
Helical Pitch	0.828
Acquisition Thickness	0.5 mm x 64
Focal Spot	Large
Filter	Medium - M
Scan Range (mm)*	333, 360, 300
Effective mAs*	139, 169, 179
DLP (mGy·cm)	269.6, 470.35, 752.15

\*Scan range and effective mAs vary based on patient anatomy. Numbers reported for these factors are reported as Subject 1, Subject 2, Subject 3.

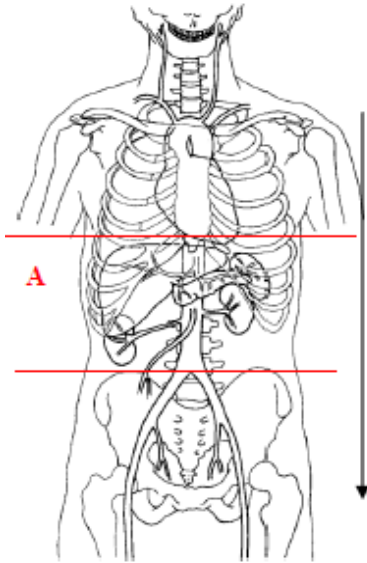


Figure 6-3. Scan range for abdominal protocol.

Table 6-3. Scan parameters for abdomen protocol in Aquilion ONE scanner.

Scan Parameter	
Nominal Tube Voltage	120 kV
Tube Rotation Time	0.5 sec
Helical Pitch	0.828
Acquisition Thickness	0.5 mm x 64
Focal Spot	Large
Filter	Medium - M
Scan Range (mm)*	220, 300, 350
Effective mAs*	157, 170, 185
DLP (mGy·cm)	227.3, 710.5, 934.7

\*Scan range and effective mAs vary based on patient anatomy. Numbers reported for these factors are reported as Subject 1, Subject 2, Subject 3.

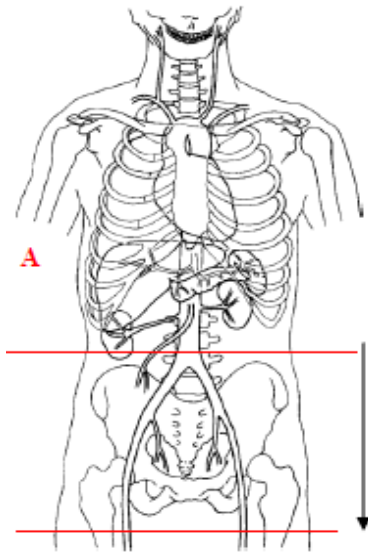


Figure 6-4. Scan region for pelvis protocol.

Table 6-4. Scan parameters for pelvis protocol in Aquilion ONE scanner.

Scan Parameter	
Nominal Tube Voltage	120 kV
Tube Rotation Time	0.5 sec
Helical Pitch	0.828
Acquisition Thickness	0.5 mm x 64
Focal Spot	Large
Filter	Medium - M
Scan Range (mm)*	240, 250, 240
Effective mAs*	133, 175, 192
DLP (mGy·cm)	212.6, 584.1, 696.9

\*Scan range and effective mAs vary based on patient anatomy. Numbers reported for these factors are reported as Subject 1, Subject 2, Subject 3.

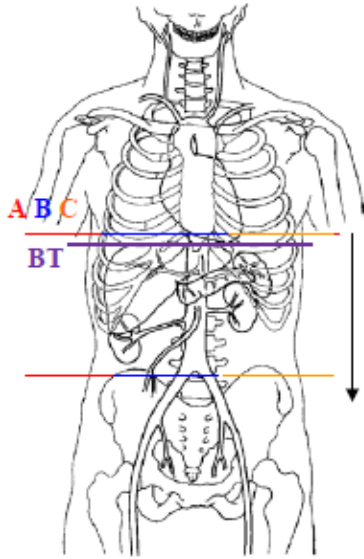


Figure 6-5. Scan range for three phase liver protocol. BT represents the level utilized for bolus-tracking.

Table 6-5. Scan parameters for three phase liver protocol in Aquilion ONE scanner.

Scan Parameter	
Nominal Tube Voltage	120 kV
Tube Rotation Time	0.5 sec
Helical Pitch	0.828
Acquisition Thickness	0.5 mm x 64
Focal Spot	Large
Filter	Medium - M
Scan Range (mm)*	225, 240, 260
Effective mAs*	157, 175, 190
DLP (mGy-cm)	713.1, 1766.85, 2973.7

\*Scan range and effective mAs vary based on patient anatomy. Numbers reported for these factors are reported as Subject 1, Subject 2, Subject 3.



Figure 6-6. Scan region for helical cardiac CTA protocol.

Table 6-6. Scan parameters for helical cardiac CTA protocol in Aquilion ONE scanner.

Scan Parameter	
Nominal Tube Voltage	120 kV
Tube Rotation Time	0.35 sec
Helical Pitch	0.828
Acquisition Thickness	0.5 mm x 64
Focal Spot	Small
Filter	Small - S
Scan Range (mm)*	280.5, 280.5, 235.5
Effective mAs*	534, 652, 700
DLP (mGy·cm)	788.55, 1025.6, 704.66

\*Scan range and effective mAs vary based on patient anatomy. Numbers reported for these factors are reported as Subject 1, Subject 2, Subject 3.

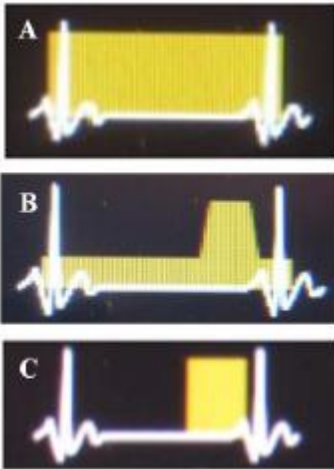


Figure 6-7. Cardiac ECG with tube current (yellow) as a function of cardiac cycle for A) cardiac functional analysis without dose modulation, B) cardiac functional analysis with dose modulation, C) prospectively gated CT angiography.

Table 6-7. Scan parameters for cardiac volumetric CTA protocols in Aquilion ONE scanner.

Scan Parameter	
Nominal Tube Voltage	120 kV
Tube Rotation Time	0.35 sec
Helical Pitch	--
Acquisition Thickness	0.5 mm x 360
Focal Spot	Large
Filter	Medium - M
Scan Range	160 mm
Effective mAs	140
DLP (mGy·cm) – PG CTA*	279.6, 309.5, 274.92
DLP (mGy·cm) – CFA w/o dose modulation	879.9, 974.5, 1181.2
DLP (mGy·cm) – CFA w/ dose modulation	533.85, 585.35, 645.81

Table 6-8. Details of volumetric chest perfusion protocol.

Scan Type	Delay (sec)	Tube voltage (kV)	Tube current (mA)	Rotation time (sec)	No. of volumes	Time b/w volumes (sec)
Dynamic Volume 1	0.0	100	100	0.5	18	2
Dynamic Volume 2	6.1	100	100	0.5	6	4
Dynamic Volume 3	6.2	100	100	0.5	4	8
Dynamic Volume 4	6.2	100	100	0.5	3	10

Table 6-9. Details of volumetric liver perfusion protocol.

Scan Type	Delay (sec)	Tube voltage (kV)	Tube current (mA)	Rotation time (sec)	No. of volumes	Time b/w volumes (sec)
Dynamic Volume 1	7.0	100	100	0.5	11	2
Dynamic Volume 2	2.0	100	300	0.5	1	--
Dynamic Volume 3	7.5	100	100	0.5	6	4
Dynamic Volume 4	1.5	100	300	0.5	1	--
Dynamic Volume 5	7.5	100	100	0.5	4	8
Dynamic Volume 6	7.5	100	100	0.5	3	8
Dynamic Volume 7	64.0	100	300	0.5	1	--

Table 6-10. Details of volumetric pancreas perfusion protocol.

Scan Type	Delay (sec)	Tube voltage (kV)	Tube current (mA)	Rotation time (sec)	No. of volumes	Time b/w volumes (sec)
Dynamic Volume 1	8.0	100	100	0.5	11	2
Dynamic Volume 2	2.0	100	300	0.5	1	--
Dynamic Volume 3	6.1	100	100	0.5	6	4
Dynamic Volume 4	3.5	100	300	0.5	1	--

## CHAPTER 7 RESULTS AND DISCUSSION

As stated in Chapter 1, the overall goal of this research project is to develop a robust methodology for the direct measurement of organ doses resulting from clinical CT scans. Chapters 2, 3, and 4 outlined the current technological state of CT, including advancements in scanning technology, various dose metrics used to quantify radiation exposure, and previous phantoms and methodologies used to estimate and measure organ doses in different ways. Chapter 5 summarized the development, testing, and optimization of this methodology, while chapter 6 provided the details for the twelve clinical CT scans that were investigated using this unique approach. This chapter serves to present the measurements and results obtained over the entire course of this project. All measurements were made utilizing the Toshiba Aquilion ONE CT scanner, Landauer nanoDot OSL dosimeters and microStar reader, and cadaveric subjects. The organ doses measured and reported in this chapter represent the first set of radiation dose measurements made inside a human body.

### **7.1 Radiographic Differences in Cadaveric Subjects**

Hounsfield units for six separate tissue types were measured from CT exams performed on live patients, tomographic physical phantoms, and cadaveric subjects, as outlined in section 5.2.3. The measured Hounsfield units are reported in Table 7.1, and a comparison of the results for different subjects is seen in Table 7.2.

For all six tissue types, the embalmed tissues of the cadaveric subjects more closely mimicked the linear attenuation coefficients of the tissues in live patients when compared to the physical phantom. The largest percent difference between the attenuation of living versus embalmed tissue occurred for the lungs, where the

cadaveric tissue differed by 9.6% (compared to 40.3% difference for the physical phantom), which is most likely due to the accumulation of embalming fluid and the partial collapse of the cadaveric lungs. It is also worthwhile to note that the lungs also showed the largest range of Hounsfield units in live patients. This is not a surprising result, as variations in the structure of lung tissue between patients can greatly impact the degree to which x-rays are attenuated. The adipose tissue of the cadaver only differed from living tissue by 3.0%, compared to 14.1% for the phantoms. All other cadaveric tissues differed from living tissue by no more than 1.0%, with the differences for muscle, bone, kidney, and liver determined to be 0.4%, 0.3%, 0.7%, and 1.0%, respectively. These results illustrate that the cadaveric subjects closely mirror the radiographic characteristics of living patients, and can therefore be utilized to accurately replicate a living patient in a clinical setting.

## **7.2 Optimization of Scanning Methodology**

### **7.2.1 Number of nanoDot Measurements**

The number of nanoDot dosimeters utilized per organ and per CT exam was minimized in two distinct ways (5.3.3.1). Table 7-3 shows the comparison of left versus right side organ dose. Nearly all organ pairs showed good agreement between the measurements. Only the breast dose (single dosimeter), colon, lower lung, and thyroid were over  $\pm 5\%$  different, with percent difference of  $\pm 7.46\%$ ,  $\pm 12.17\%$ ,  $\pm 7.12\%$ , and  $\pm 23.0\%$ , respectively. The largest of the differences occurred for the thyroid, but upon further investigation it was determined that the left dosimeter had moved outward to the surface from its initial position, thereby increasing its reported dose. Due to the degree to which these doses agreed, it was concluded that all organ pairs could be measured on a single organ within the pair, with the two exceptions of the thyroid and colon.

Table 7-4 shows the comparison of doses reported from neighboring dosimeters in the same placement tube. Based on these results, it was determined that the outer dosimeter could be removed from the tube accessing the right upper lobe of the liver, as well as the outer dosimeter from the tube accessing the stomach. This conclusion was based on the similarities of doses reported between these and the next closest dosimeters, with both being within 0.5mGy of each other.

It must be noted that during the scans performed with the third cadaver, the left-side thyroid position continued to be problematic due to an anatomical structure blocking the original incision site. This led to thyroid measurements only in the right thyroid position. In all, the number of nanoDots used per scan was reduced from 47 during this study to 29 after this study, a 38% reduction in dosimeters with minimal impact on data accuracy.

### **7.2.2 Number of Repeat CT Scans**

The number of repeat CT scans for any given protocol was minimized to allow the maximum number of protocols to be investigated (5.3.3.2). Table 7-5 lists the organ doses per scan for an increasing number of CAP scans. The far right column gives the average organ doses for all 11 CAP scans performed, and the bottom row of the table shows the average absolute differences, as determined by comparing the measured and average doses. As expected, the average differences decrease with an increasing number of repeated scans. After analyzing this data, it was determined that repeating the scans twice for each CT exam (and corresponding set of dosimeters) would be sufficient, as that yielded an average absolute difference of  $\pm 5\%$ .

### **7.2.3 Number of Repeated nanoDot Readouts**

The number of repeat nanoDot readouts for a single dosimeter was minimized to decrease the time needed to obtain dose measurements per CT exam (5.3.3.3). Table 7-6 contains the data and calculated values for each dosimeter. The average difference for all dosimeters analyzed was  $\pm 1.10\%$ , meaning that reading each dosimeter two additional times yielded an improvement in accuracy of no more than  $\pm 1.10\%$ . For this reason, it was determined that each dosimeter could be read out a single time for all dose measurements made during this project.

### **7.2.4 Summary of Methodology Optimization**

For clarity of procedure, it seems constructive at this point to summarize the overall changes discussed at length over the last few pages. The optimization of scanning protocols involves three main conclusions and methodological adjustments:

1. Number of organ dose measurements and dosimeters per organ. Table 5-1 listed the initial location and number of tubes and nanoDots to be used. After investigation, it was determined that it was possible to decrease the number of tubes and dosimeters without a perceivable impact on dose measurements. The final assignments for tube and dosimeter placement for all CT exams investigated throughout this research project are summarized in Table 7-7.
2. Number of repeated scans per CT protocol. It has been determined that repeating all scans twice yields a percent deviation for all organ dose measurements of  $\pm 5\%$ .
3. Number of repeated nanoDot readouts. It has been shown extensively that reading each nanoDot dosimeter three times increases the accuracy of the measurements by  $\pm 1.1\%$  at most. For this reason each nanoDot used to measure organ doses in this research project was read a single time.

## **7.3 Organ Dose Measurements**

The methodology described in chapter 5 was utilized to measure organ doses in three female cadaveric subjects. Subject 1 was a 100 lb specimen with a BMI of 16.6, and is referred to as the “small” subject. Subject 2 was a 143 lb specimen with a BMI of

21.7, and is referred to as the “medium” subject. Subject 3 was a 170 lb specimen with a BMI of 26.6, and is referred to as the “large” subject.

For each of the twelve CT protocols investigated, organ and skin doses were measured using nanoDot OSL dosimeters. The measurements were adjusted as required by Equation 4-3, with the appropriate energy and scatter correction factors listed in Table 4-2 and corresponding f-factors listed in Table 4-3. The minimum, maximum and average organ doses are reported for each protocol, along with an overall standard deviation and an “in-field” standard deviation, as explained in Section 6.1.2. In addition, for each protocol, graphs of organ dose as a function of BMI were produced to illustrate how organ doses vary with patient size.

### **7.3.1 Helical Torso Exams**

#### **7.3.1.1 Chest-Abdomen-Pelvis (CAP)**

The CAP protocol, described in Section 6.2.1.1, was investigated. The measured organ doses from the small, medium, and large subjects are reported in Table 7-8, Table 7-9, and Table 7-10, respectively. The organ doses as a function of BMI are plotted in Figure 7-1.

One main point of interest from the data reported for the CAP exams is the thyroid measurement for the medium subject. Figure 7-1 illustrates that this organ received less exposure than that seen in both the small and large subjects. Upon further review of the CT images, it was determined that the thyroid of the medium specimen was not in the range of the primary beam due to the standard positioning procedure for the CAP protocol. Clinically, this result is accurate, as the scanning range should be set to begin at the thoracic inlet. Because of this, the thyroid is often located at the edge of the scanning range, and the individual patient anatomy determines whether it is irradiated

by the primary beam. This result can also be seen for the chest exam (Figure 7-2) which also begins at the thoracic inlet.

It is also interesting to note that for all three subjects, the lungs received the lowest dose of any organ (excluding the thyroid), with lung doses of 12.33 mGy, 16.27 mGy, and 21.47 mGy for the small, medium, and large subjects, respectively. The highest doses were determined to be 18.8 mGy to the skin for the small subject, 30.15 mGy to the surface of the breast for the medium subject, and 43.11 mGy to the small intestine for the large subject. While the organ of maximum dose changes, it is important to note that all three dose measurements occur on or very near the surface of the body, with the small intestine measurement occurring at a depth of approximately 4 cm. This is an expected result, and the variation in the organs of maximum dose can be attributed to the position of, and distance between, the x-ray tube and these organs during the helical acquisition.

#### **7.3.1.2 Chest**

The chest protocol, described in Section 6.2.1.2, was investigated. The measured organ doses from the small, medium, and large subjects are reported in Table 7-11, Table 7-12, and Table 7-13 respectively. The organ doses as a function of BMI are plotted in Figure 7-2.

Other than the thyroid issue, which was previously discussed in section 7.3.1.1, the results for the chest exam are consistent with expectations. For all subjects, the doses to the lower anatomy (small intestine, colon, and ovaries) are under 10mGy, as none of these organs were exposed to the primary beam. For all other organs, the doses increased with increasing BMI, ranging from roughly 11 to 16 mGy for the small specimen, 14 to 19 mGy for the medium, and 22 to 32 mGy for the large.

### **7.3.1.3 Abdomen**

The abdomen protocol, described in Section 6.2.1.3, was investigated. The measured organ doses from the small, medium, and large subjects are reported in Table 7-14, Table 7-15, and Table 7-16, respectively. The organ doses as a function of BMI are plotted in Figure 7-3.

For this protocol, both the thyroid and ovaries received only scatter radiation for all subjects. Interestingly, all of the measurement points within the lungs and small intestine of the small subject were also outside of the scanning range due to the organ location within that subject. Additionally, the lungs of both the medium and large subjects were only partially irradiated by the primary beam, resulting in a large difference between the doses to the lower lung (in scanning range) and upper lung (outside of scanning range). Finally, similar to the chest protocol, for organs that were in the primary beam, the dose increased with BMI, ranging from roughly 12 to 16 mGy for the small specimen, 18 to 28 mGy for medium, and 20 to 32 mGy for the large. These organ doses are slightly higher than those seen from the chest protocol, which is expected due to the thicker anatomy and corresponding higher effective mAs values used (Tables 6-2 and 6-3).

### **7.3.1.4 Pelvis**

The pelvis protocol, described in Section 6.2.1.4, was investigated. The measured organ doses from the small, medium, and large subjects are reported in Table 7-17, Table 7-18, and Table 7-19, respectively. The organ doses as a function of BMI are plotted in Figure 7-4.

Since the pelvis protocol has a scanning range starting at the iliac crests and ending at the lesser trochanter, only the small intestine, colon, ovaries, and skin are in

the primary beam. The measured organ doses reflect this, with doses for these organs ranging from 10 mGy to nearly 30 mGy (Figure 7-4), and generally increasing with BMI. For all other organs, none of which were in the primary beam, the doses were under 5 mGy for all subjects. It is also interesting to note that, despite the lower effective mAs utilized with the smaller subject (Table 6-4), the organ doses delivered to organs outside the primary beam were higher than those received by the organs of the medium and large subjects. This is due to the shorter distance between these organs and the primary beam in the small subject, and is a result that is theoretically sound, but is not often realized in the clinical setting.

#### **7.3.1.5 Three-phase liver**

The three-phase liver protocol, described in Section 6.2.1.5, was investigated. The measured organ doses from the small, medium, and large subjects are reported in Table 7-20, Table 7-21, and Table 7-22, respectively. The organ doses as a function of BMI are plotted in Figure 7-5.

For all subjects, the thyroid and ovaries were outside of the scanning range, and received less than 5 mGy. In addition, once again due to the smaller organ sizes, the lungs and small intestine of the small subject were also outside the scanning range. The organs irradiated with the primary beam received between 30 to 40 mGy for the small subject, 35 to 70 mGy for the medium subject, and 40 to 80 mGy for the large subject. These results are consistent with what is expected due to the increase in effective mAs with increasing patient size (Table 6-5).

#### **7.3.1.6 Comments on helical torso exam results**

Several observations can be made by observing the results that have been reported for the five helical torso exams. First, for the CAP exam and individual chest,

abdomen, and pelvis exams, the average organ doses for organs receiving primary beam irradiation do not vary greatly. For the small subject, doses ranged from 10 to 17 mGy for all exams, while the medium subject received doses ranging from 15 to 30 mGy, and the large subject's doses ranged from 20 to 32 mGy, with the exception of the small intestine in the CAP exam. While this result may not be entirely surprising given that each of these exams utilize similar techniques, it illustrates the impact that tube current modulation has on the organ doses, especially as a function of BMI. In addition, comparing the dose to individual organs for each exam illustrates the importance of utilizing the appropriate protocol and a limited scanning range. An example of this would be the tendency (in some situations) to utilize a combined abdomen-pelvis protocol, when the diagnostic information needed could be obtained with only a pelvis CT exam. In that situation, the additional abdomen exam would result in unnecessary irradiation of the breast, lung, liver, and stomach.

Another interesting observation is the parabolic nature of some of the organ dose curves. These curves occur when the doses measured in the medium subject are larger than those measured in the large subject. Examples of this can be seen in the curves for the colon in the chest protocol (Figure 7-2), the liver in the abdomen protocol (Figure 7-3), and the small intestine in the pelvis protocol (Figure 7-4). This phenomenon is due to the fact that as the patients' height increases, the distance between the organs can become larger. This results in less exposure to the organs that are outside the scanning range simply because the scattered radiation needs to pass through more tissue, and therefore undergoes more attenuation in the larger (taller) patient.

## 7.3.2 Cardiac Exams

### 7.3.2.1 Helical CT Angiography (CTA)

The helical CTA protocol, described in Section 6.2.2.1, was investigated. The measured organ doses from the small, medium, and large subjects are reported in Table 7-23, Table 7-24, and Table 7-25, respectively. The organ doses as a function of BMI are plotted in Figure 7-6.

As expected, the largest organ doses resulting from the helical CTA protocol were to the breasts (gland and skin), lungs, and skin. For all three organs, the doses were actually larger for the small patient (34.5, 33.3, 33.1, and 40.5, respectively) than for the large patient (31.3, 27.9, 23.3, and 34.4, respectively), with the medium patient falling between the two with the exception of the lung dose. While this result is not expected, it can be partially explained by considering the DLP values reported for this exam (Table 6-6). Although the scanning range for each patient adhered to the recommended anatomical markers of 2cm above the carina to 2cm below the bottom of the heart, the range and DLP for the large patient was the smallest of the three. This result illustrates the importance of, and potential issues stemming from, setting a range based upon anatomical markers versus one set by width of the scanning range.

Another interesting result for this exam is the parabolic curves for the stomach and liver doses versus BMI (Figure 7-6). While this curve shape was previously seen for some of the helical torso protocols, in this instance this result stems from the larger scanning range (and subsequent larger DLP value) utilized in scanning the medium subject, as was previously discussed.

### 7.3.2.2 Volumetric CTA

Three CTA protocols utilizing the Aquilion ONE's broad-beam volumetric image acquisition capability were investigated. Each volumetric CTA protocol was described in Section 6.2.2.2, and their image acquisition parameters are listed in Table 6-7. The first was the prospectively-gated CTA protocol. The measured organ doses from the small, medium, and large subjects are reported in Table 7-26, Table 7-27, and Table 7-28, respectively, and the organ doses as a function of BMI are plotted in Figure 7-7. The second volumetric CTA protocol was cardiac functional analysis (CFA) without dose modulation. The measured organ doses from this protocol are reported in Table 7-29, Table 7-30, and Table 7-31, and the organ doses as a function of BMI are plotted in Figure 7-8. The third and final volumetric protocol investigated was CFA with dose modulation. The measured organ doses for this protocol are reported in Table 7-32, Table 7-33, and Table 7-34, while the organ doses as a function of BMI are plotted in Figure 7-9.

For all volumetric cardiac protocols, the breast (skin and gland), lung, and skin organ doses were highest, as was expected due to the scan range used. The prospectively-gated CTA protocol was found to deliver the lowest organ doses for all measurements, with the lungs and breasts receiving between 10 and 20 mGy, and the skin receiving between 17 and 27 mGy, depending on the subject size utilized. All other organs received less than 10mGy from the prospectively-gated CTA protocol.

The CFA protocol without dose modulation delivered consistently higher organ doses than the CFA protocol with dose modulation. This is not surprising, as the main impetus behind dose modulation is the ability to reduce the tube current for thinner or less-attenuating anatomical sections, resulting in lower doses. Table 7-35 provides a

comparison of the organ doses for these two protocols, measured with the small subject. While the organ doses measured for the small intestine and ovary were actually larger for the CFA protocol with modulation, these two results are not considered significant, as they represent the smallest doses recorded for these protocols, and the differences between both sets of measurements are less than 0.5 mGy.

All other organ doses were reduced by using dose modulation with the CFA protocol. The average dose reduction for the small subject was 35.01% (Table 7-35). Similar calculations yield average organ dose reductions of 30.38% for the medium subject and 43.33% for the large subject across all organs. In addition, the dose reduction was greater for organs receiving primary beam irradiation (breast skin, breast tissue, lung, and skin). For these organs, the average dose reduction using the CFA protocol with dose modulation was 42.12%, 39.63%, and 47.59% for the small, medium, and large subjects, respectively. With these results in mind, it is interesting to note that the DLP values for the two CFA exams (Table 6-7) indicate similar dose reductions of 39.3%, 39.9%, and 45.3% when utilizing dose modulation. These values are within  $\pm 2.5\%$  of those determined from organ dose measurements for organs in the primary beam. This result is interesting in that it may indicate a direct correlation between the DLP values and the organs experiencing primary beam irradiation, although more work is needed to investigate this relationship.

### **7.3.2.3 Comments on cardiac exam results**

A comparison of the average organ doses resulting from cardiac CT exams is seen in Table 7-36. While this table shows the measurements made using the small subject, the results are consistent with those for the other two subjects as well. Overall,

the prospectively-gated CTA protocol yielded the lowest organ doses, followed by the CFA protocol with dose modulation. Both the helical CTA and CFA protocol without dose modulation delivered the highest organ doses, although which dose was higher actually depended on the organ of interest. In general, the CFA protocol without dose modulation gave higher doses to the organs in the primary beam, while the helical CTA protocol delivered higher doses to the organs receiving only scattered radiation. This is due to the fact that the scanning range for the helical CTA is nearly twice as long as that for any of the volumetric protocols, which results in nearly twice as many photons being scattered toward organs outside the primary beam.

Since the prospectively-gated CTA and CFA with dose modulation yield the lowest organ doses, these two protocols should be utilized when CT imaging of the heart and surrounding vessels is necessary. The combination of these two protocols covers a large range of clinical concerns and indications (Section 6.2.2.2). If information only concerning the structure of the heart and surrounding vessels is needed, the prospectively-gated CTA should be used. Similarly, if information about the function and competency of the heart and nearby vasculature is necessary, the CFA protocol with dose modulation should be used.

#### **7.3.2.4 Comparison to previous studies**

Previous research has been performed in attempts to determine the doses for cardiac exams on an Aquilion ONE CT scanner. Lavoie<sup>72</sup> utilized the same OSL dosimeters used in this project in conjunction with tomographic physical phantoms. Ghita<sup>48</sup> developed a code to simulate the 320-slice Aquilion ONE's image acquisitions, and this was used along with computational phantoms to obtain dose estimates using Monte Carlo simulations. Table 7-37 shows the comparison of their results with the

measurements made in this project. The cadaveric results are reported as both the measurements made using the medium subject (BMI 21.7), as well as data extrapolated from Figures 7-7, 7-8, and 7-9 corresponding to a BMI of 23.5. The latter data was included to provide an exact comparison (in terms of patient BMI) to the work done by Lavoie and Ghita.

While there are differences between cadaveric organ doses and those reported for both phantom measurements and Monte Carlo simulations, a few observations can be made. Primarily, for the thyroid and lung doses, both phantom measurements and simulations seem to overestimate the dose when compared to the cadaveric measurements, although only by a few milligray. Second, stomach doses seem to be underestimated by the phantom and simulations by as much as a factor of 2. One possible explanation could be an irregularly low stomach position or measurement point in the phantom/simulated patient. While it could be argued that the measurement point for stomach doses within the cadavers was too high (or too close to the heart), this rationale is not as likely because the cadaveric stomach measurements are consistently almost twice as large as those reported from the phantom and simulations. Third, the skin doses, although difficult to determine an “average” dose, are in good agreement with the doses reported for the phantom and simulation. While the phantom and MC skin doses had a higher variation than those reported for other organs, the cadaveric measurements generally fell between the two. Finally, these results show one of the strengths of the direct measurement methodology. By comparing the results obtained directly to those obtained indirectly (either through estimation or simulation via computer

programming), it is possible to gain insights into how the phantoms or models could be altered to more accurately represent living human anatomy.

### **7.3.3 Body Perfusion Exams**

#### **7.3.3.1 Chest perfusion**

The chest perfusion protocol, described in Section 6.2.3.1, was investigated. The measured organ doses from the small, medium, and large subjects are reported in Table 7-38, Table 7-39, and Table 7-40, respectively. The organ doses as a function of BMI are plotted in Figure 7-10.

#### **7.3.3.2 Liver perfusion**

The liver perfusion protocol, described in Section 6.2.3.2, was investigated. The measured organ doses from the small, medium, and large subjects are reported in Table 7-41, Table 7-42, and Table 7-43, respectively. The organ doses as a function of BMI are plotted in Figure 7-11.

#### **7.3.3.3 Pancreas perfusion**

The pancreas perfusion protocol, described in Section 6.2.3.3, was investigated. The measured organ doses from the small, medium, and large subjects are reported in Table 7-44, Table 7-45, and Table 7-46, respectively. The organ doses as a function of BMI are plotted in Figure 7-12.

#### **7.3.3.4 Comments on body perfusion exam results**

As expected, the highest doses from each perfusion exam are given to those organs in the primary beam. These organs are the lungs, breasts, and skin for the chest perfusion exam, the liver, stomach, and skin for the liver perfusion exam, and the stomach and skin for the pancreas perfusion exam. It is also worthwhile to draw attention to the fact that, as the patient size/height decreases, organs that may not be in

the primary beam for the larger patients are irradiated by the primary beam in the smaller patient. This is especially true for both the colon and breast in a liver perfusion exam (Figure 7-11) and for the liver in a pancreas perfusion exam (Figure 7-12).

Due to the number of repeat scans over the same anatomy for body perfusion exams (Tables 6-8, 6-9, and 6-10), it is not surprising that the highest doses recorded for this entire research project came from these exams. The chest perfusion protocol resulted in skin doses over 100 mGy and doses over 50 mGy for the breast and lungs for the medium and large patients. The liver perfusion exam also yielded skin doses over 100 mGy and doses of at least 80 mGy to the liver and stomach for all subjects. Finally, the pancreas perfusion protocol resulted in skin doses between 70 and 80 mGy, with organ doses over 50 mGy for the stomach and liver for the small and medium patients, and also for the colon and small intestine of the large patient. These differences are once again attributed to the different anatomical position of the various organs, especially as the subjects increase in size.

While these exams certainly do result in larger organ doses, it needs to be noted that at the time of this writing these perfusion exams are not yet clinically utilized. It was previously stated that body perfusion imaging represents one of the very newest areas of CT imaging, and as such, the protocols are still considered works in progress and have not been cleared for use on patients. However, as the protocols and techniques are adjusted in the future, the organ dose data that has been collected will be available for comparison and risk assessment purposes.

Table 7-1. Measured Hounsfield units for live patients, phantoms, and cadaveric subjects.

Measurement Number	Live Patient					Tomographic Phantom		Cadaver	
	1	2	3	4	5	1	2	1	2
Lung	-820	-650	-730	-820	-840	-670	-690	-800	-700
Fat	-115	-90	-105	-105	-95	32	18	-70	-80
Muscle	40	60	65	48	40	32	18	47	63
Bone	550	600	575	500	550	630	570	520	580
Kidney	60	39	53	33	28	5	15	45	55
Liver	43	60	77	55	45	5	15	48	42

Table 7-2. Comparison of Hounsfield Units.

Tissue Type	Hounsfield Units			% Difference versus Patient	
	Patient	Phantom	Cadaver	Phantom	Cadaver
Lung	-772	-680	-750	40.3%	9.6%
Fat	-102	25	-75	14.1%	3.0%
Muscle	50.6	25	55	2.4%	0.4%
Bone	555	600	550	2.9%	0.3%
Kidney	42.6	10	50	3.1%	0.7%
Liver	56	10	45	4.4%	1.0%

Table 7-3. Comparison of right and left side organ dose measurements.

Organ		Organ Dose (mGy)				Percent Difference
		Left	Right	Average	Difference	
Breast*	double	24.44	24.46	24.45	0.02	0.08%
	single	23.18	24.98	24.08	1.80	7.46%
	skin	25.07	24.49	24.78	0.58	2.36%
Colon		26.23	29.64	27.93	3.40	12.17%
Eyes		1.32	1.35	1.33	0.03	2.22%
Lung	lower	22.99	24.69	23.84	1.70	7.12%
	upper	23.33	23.93	23.63	0.60	2.54%
Ovary		25.40	24.20	24.80	1.20	4.84%
Thyroid		33.34	26.47	29.90	6.88	23.00%

\*Breast doses were split into three sections. Double denotes the tube containing two dosimeters, single denotes the tube containing one dosimeter, and skin denotes the average of five dosimeters placed in a + pattern on the surface of the breast.

Table 7-4. Comparison of dose measurements within same placement tube.

Organ	Liver			Stomach			
Tube Location	Right Upper Lobe			Right Lower Lobe			
nanoDot Position	Inner	Middle	Outer	Inner	Outer	Inner	Outer
Dose (mGy)	24.11	26.25	26.01	26.65	27.79	31.67	31.12

Table 7-5. Organ dose per CAP exam as a function of number of repeated scans.

Organ	Location	Organ Dose per Scan (mGy)				Average
		1 Scan	2 Scans	3 Scans	5 Scans	
Colon	ascending	35.45	37.56	31.56	31.91	33.16
	descending	30.37	29.63	26.82	27.67	28.04
Breast	inner	25.04	25.99	25.17	24.29	24.91
	outer	26.45	24.55	24.39	23.74	24.31
	skin, center	24.23	24.40	23.28	20.85	22.47
	skin, outer	21.01	23.40	27.56	23.87	24.53
	skin, upper	28.62	25.18	25.31	26.18	25.98
Lung	inner	24.25	20.78	22.88	22.65	22.52
	outer	23.91	23.09	25.05	21.94	23.18
Liver	left lobe	32.33	33.71	29.92	29.75	30.75
	right lower lobe, inner	29.16	28.80	29.51	25.41	27.49
	right lower lobe, outer	31.45	31.02	28.51	31.86	30.76
Ovary	left	27.34	24.93	26.46	25.60	25.87
Skin	chest	28.43	28.58	29.43	26.71	27.95
Thyroid	right lower lobe	28.43	30.27	34.61	31.98	32.07
Average Absolute Difference*		6.7%	5.0%	4.8%	3.1%	

\*Average absolute difference measured between the 11 scan average and the organ dose per scan, averaged over all organs

Table 7-6. Comparison of dosimeter readings.

Serial Number	First Reading (mGy)	Three Reading Average (mGy)	Percent Difference
DN091314252	63.87	64.46	0.91%
DN09128428R	67.10	66.96	0.21%
DN09133268U	83.89	86.85	3.47%
DN091322081	23.03	23.06	0.12%
DN09135568M	101.34	102.14	0.78%
DN09131389Q	62.47	61.43	1.67%
DN091331446	58.47	58.83	0.61%
DN09132097Y	27.36	27.41	0.21%
DN09131987I	23.57	23.21	1.54%
DN09136119W	68.66	68.94	0.41%
DN09131396V	100.61	101.44	0.83%
DN091302546	21.21	20.93	1.35%
DN09135699F	65.97	64.51	2.25%
DN091331371	116.22	116.19	0.03%
DN09129425W	64.34	64.83	0.75%
DN09128385T	56.17	56.35	0.31%
DN09131437X	109.58	110.70	1.01%
DN091320845	106.24	105.51	0.69%
DN091313717	56.37	56.88	0.91%
DN091361609	98.58	96.44	2.19%
DN091361328	59.04	59.19	0.25%
DN09128338S	55.79	56.86	1.90%
DN091315052	64.86	65.34	0.73%
DN09131377V	19.67	19.65	0.12%
DN09128437S	106.18	102.98	3.06%
DN09131743Y	60.56	60.65	0.14%
DN091267104	96.14	97.42	1.32%
DN09128911W	23.93	23.82	0.46%
DN09131509U	65.78	65.39	0.60%
DN091322354	59.55	60.74	1.98%
DN09127722Y	83.06	83.09	0.03%
DN09128406X	57.62	57.91	0.50%
DN091358010	123.35	121.52	1.49%
DN09131653Z	82.93	81.63	1.58%
DN09136158U	52.32	52.73	0.78%
DN09133266Y	28.70	28.75	0.19%
DN09126578M	69.48	68.96	0.75%
DN091284231	67.39	69.28	2.76%
DN091360932	25.62	25.51	0.44%

Table 7-6. Continued

Serial Number	First Reading (mGy)	Three Reading Average (mGy)	Percent Difference
DN09136068V	26.40	26.22	0.67%
DN091306126	65.66	65.24	0.64%
DN09126604Z	54.87	55.42	1.01%
DN09131069Y	62.14	61.26	1.44%
DN09128378O	59.29	60.25	1.62%
DN09131904W	115.99	116.08	0.07%
DN09135927K	89.80	89.85	0.05%
DN09126716S	62.35	62.79	0.70%
DN09130526Z	64.96	65.17	0.31%
DN091271080	18.36	19.03	3.58%
DN091271626	57.67	59.90	3.80%
DN09128397O	19.83	19.67	0.81%
DN09127061A	69.95	71.80	2.61%
DN09128444X	3.62	3.57	1.42%
DN091266122	63.54	62.78	1.20%
DN09128457Q	87.60	87.63	0.03%
DN09136086X	97.62	98.56	0.96%
DN09135576P	59.22	58.78	0.75%
DN091332551	71.12	70.53	0.84%
DN09136138W	21.41	21.47	0.27%
DN09132746R	21.56	21.45	0.47%
DN091305631	19.61	19.39	1.14%
DN09133455X	22.19	21.94	1.12%
DN09126564V	13.63	13.42	1.57%
DN09134061B	23.09	23.33	1.06%
DN091331727	67.57	70.21	3.84%
DN09135483W	23.31	23.31	0.01%
DN09133212B	54.49	54.70	0.38%
DN09129383W	95.44	98.24	2.90%
DN091360263	104.38	105.11	0.70%
DN09133979D	23.70	23.65	0.20%
DN09136156Y	16.90	17.04	0.79%
DN09128477O	91.77	95.13	3.60%
DN091361253	58.96	58.77	0.32%
DN09133131D	76.97	76.07	1.18%
DN091360742	76.95	77.62	0.86%
DN09128395S	99.21	97.53	1.70%
DN091270909	60.53	59.59	1.56%
DN09135929G	86.01	83.96	2.40%

Table 7-6. Continued

Serial Number	First Reading (mGy)	Three Reading Average (mGy)	Percent Difference
DN09128841V	99.40	100.67	1.27%
DN09128862R	20.20	20.31	0.52%
DN09134021F	24.81	24.63	0.74%
DN09128865L	98.38	100.59	2.22%
DN09128871S	124.85	124.52	0.26%
DN091332056	64.88	63.97	1.42%
DN09132777M	72.85	72.85	0.00%
DN09131366Y	120.92	121.14	0.18%
DN09128884L	23.09	23.06	0.10%
DN091335042	61.12	61.27	0.25%
DN09131686Q	65.26	66.87	2.43%
DN091310838	59.34	59.15	0.31%
DN091262724	109.26	104.65	4.31%
DN09136101D	22.32	22.17	0.68%
DN091332650	59.56	59.72	0.26%
DN09128954M	3.59	3.63	1.12%
DN091284207	58.39	58.15	0.41%
Average			1.10%

Table 7-7. Finalized location and number of tubes and nanoDots for organ dose measurements.

Organ	Number of Tubes	Number of Dosimeters
Breast	3	4
Breast - Skin	--	5
Colon	2	2
Eyes	--	1
Liver	3	5
Lung	2	4
Ovaries	1	1
Skin - central scan axis	--	3
Skin - surface*	--	3
Small Intestine	1	1
Stomach	1	1
Thyroid	1	1

\*For each scan, a dosimeter was placed on the skin at a position on the chest, abdomen, and pelvis

Table 7-8. Organ doses for CAP protocol and small subject.

	Organ Dose (mGy)			
	Max	Min	Ave	St Dev
Thyroid	--	--	14.59	--
Breast (gland)	19.35	17.21	18.17	1.08
Breast (skin)	26.05	12.61	18.00	4.95
Lung	13.17	11.54	12.33	0.67
Liver	19.86	17.01	18.41	1.12
Stomach	--	--	15.03	--
Small Intestine	--	--	18.34	--
Colon	17.27	15.80	16.54	1.04
Ovary	--	--	15.41	--
Skin	19.73	17.59	18.80	1.10

Table 7-9. Organ doses for CAP protocol and medium subject.

	Organ Dose (mGy)			
	Max	Min	Ave	St Dev
Thyroid	--	--	10.49	--
Breast (gland)	26.31	22.98	24.14	1.88
Breast (skin)	35.06	24.22	30.15	3.96
Lung	23.36	11.24	16.27	5.42
Liver	31.53	19.55	24.93	4.77
Stomach	--	--	30.63	--
Small Intestine	--	--	28.51	--
Colon	25.95	20.37	23.16	3.95
Ovary	--	--	16.46	--
Skin	32.95	22.34	28.25	5.41

Table 7-10. Organ doses for CAP protocol and large subject.

	Organ Dose (mGy)			
	Max	Min	Ave	St Dev
Thyroid	--	--	29.48	--
Breast (gland)	27.77	24.38	25.99	1.52
Breast (skin)	28.26	23.34	25.47	1.91
Lung	22.76	20.47	21.47	1.06
Liver	33.00	27.94	29.99	2.03
Stomach	--	--	29.78	--
Small Intestine	--	--	43.11	--
Colon	36.34	29.41	32.87	4.90
Ovary	--	--	24.43	--
Skin	33.09	26.35	29.94	3.39

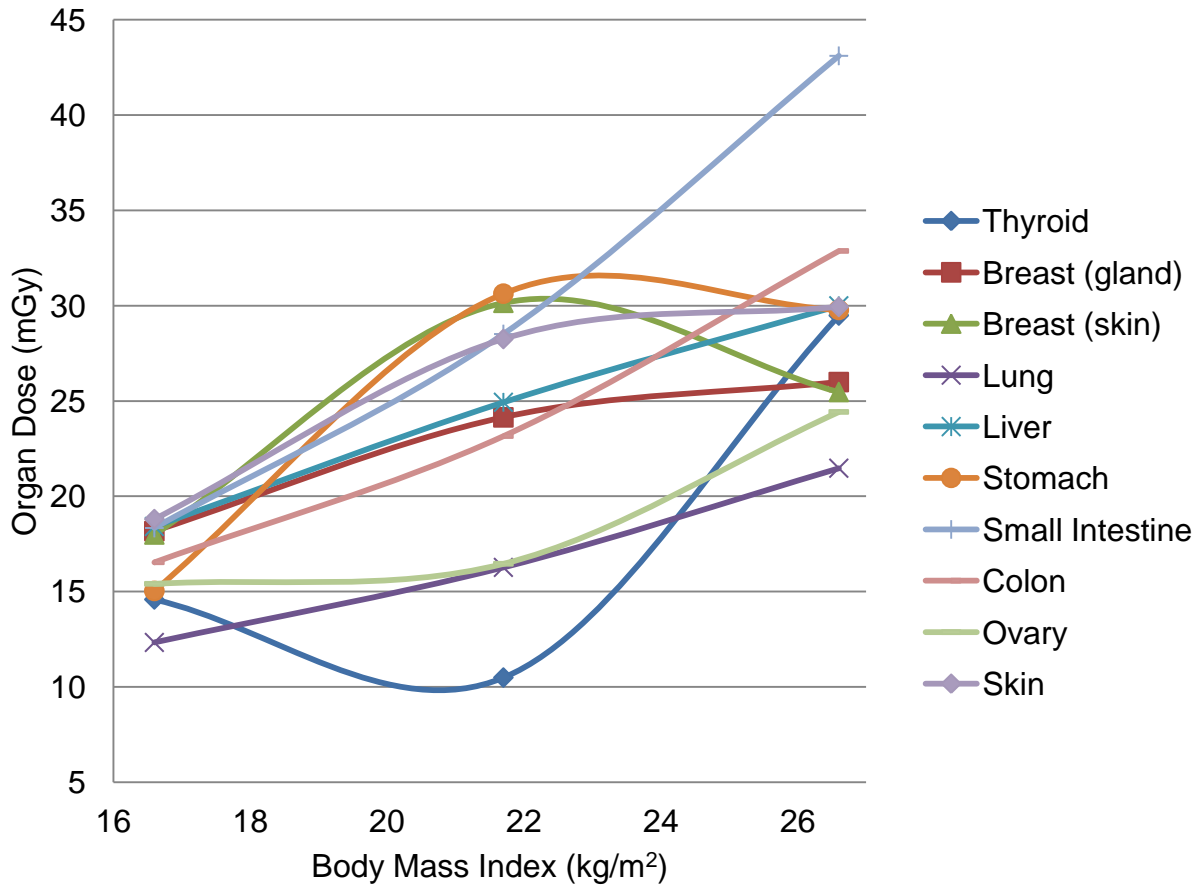


Figure 7-1. Organ dose versus BMI for CAP protocol.

Table 7-11. Organ doses for chest protocol and small subject.

	Organ Dose (mGy)			
	Max	Min	Ave	St Dev
Thyroid	--	--	8.70	--
Breast (gland)	16.01	14.66	15.42	0.69
Breast (skin)	17.19	13.03	15.52	1.71
Lung	11.42	9.35	10.72	0.93
Liver	14.35	9.03	12.23	2.23
Stomach	--	--	10.81	--
Small Intestine	--	--	0.68	--
Colon	7.49	2.11	4.80	3.81
Ovary	--	--	0.25	--
Skin	15.64	9.52	12.39	3.08

Table 7-12. Organ doses for chest protocol and medium subject.

	Organ Dose (mGy)			
	Max	Min	Ave	St Dev*
Thyroid	--	--	4.94	--
Breast (gland)	20.97	14.04	18.06	3.60
Breast (skin)	22.23	14.09	19.10	3.29
Lung	16.72	12.23	14.60	2.06
Liver	20.24	9.81	15.97	3.88
Stomach	--	--	15.68	--
Small Intestine	--	--	2.64	--
Colon	9.12	8.12	8.62	0.71
Ovary	--	--	0.58	--
Skin	22.05	14.53	17.97	3.80

Table 7-13. Organ doses for chest protocol and large subject.

	Organ Dose (mGy)			
	Max	Min	Ave	St Dev
Thyroid	--	--	22.21	--
Breast (gland)	29.56	25.76	28.38	1.33
Breast (skin)	28.61	25.13	26.65	1.71
Lung	26.26	20.84	23.17	2.29
Liver	27.92	21.20	24.94	2.79
Stomach	--	--	25.42	--
Small Intestine	--	--	4.69	--
Colon	6.42	3.71	5.07	1.92
Ovary	--	--	0.52	--
Skin	36.16	29.68	32.00	3.61

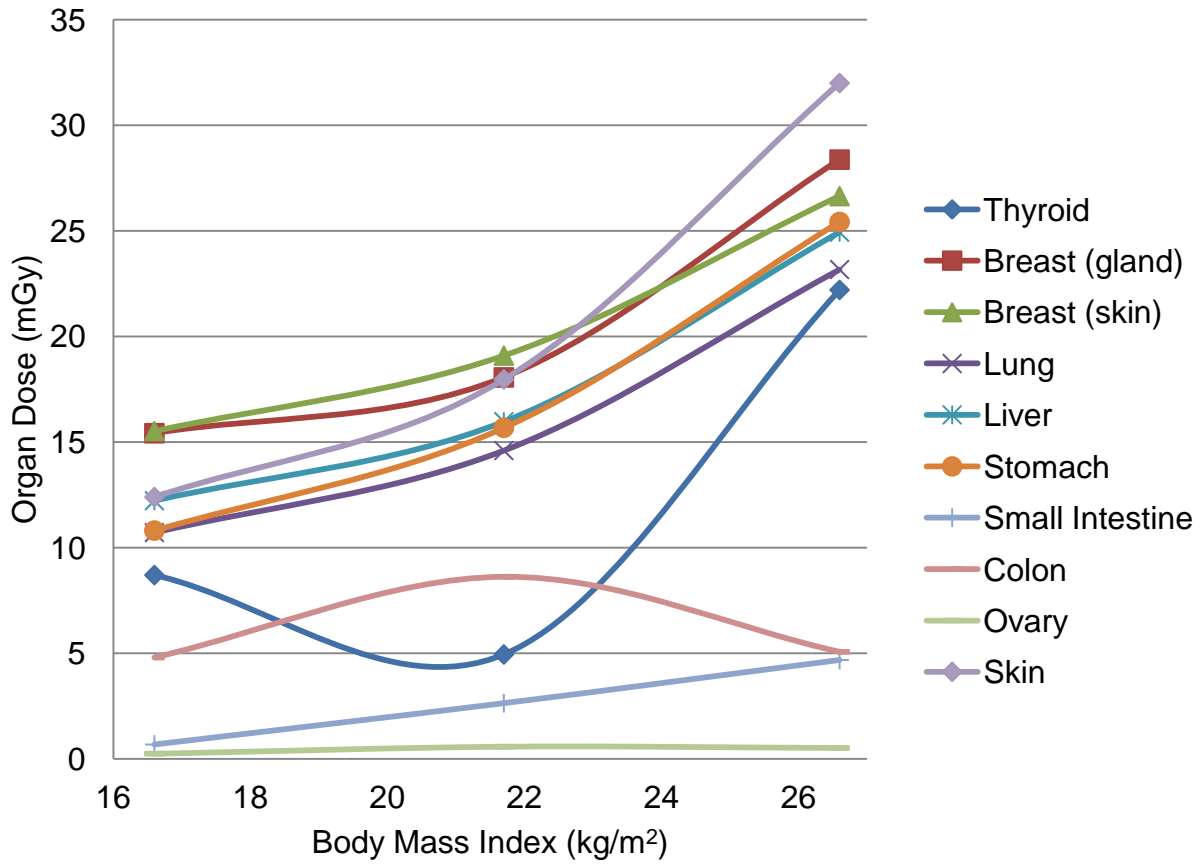


Figure 7-2. Organ dose versus BMI for chest protocol.

Table 7-14. Organ doses for abdomen protocol and small subject.

	Organ Dose (mGy)				
	Max	Min	Ave	St Dev*	St Dev (in)**
Thyroid	--	--	0.19	--	--
Breast (gland)	15.80	12.08	13.80	1.88	--
Breast (skin)	17.73	6.61	13.24	4.34	2.60
Lung	3.39	0.58	1.93	1.48	--
Liver	13.78	9.91	12.81	1.64	0.30
Stomach	--	--	12.54	--	--
Small Intestine	--	--	4.83	--	--
Colon	14.39	13.25	13.82	0.80	--
Ovary	--	--	1.13	--	--
Skin	19.26	11.51	15.81	3.95	--

\*Standard deviation is taken for all dosimeters placed in or on an organ.

\*\*Standard deviation (in) is calculated only for those organ dosimeters located within the primary x-ray beam.

Table 7-15. Organ doses for abdomen protocol and medium subject.

	Organ Dose (mGy)				
	Max	Min	Ave	St Dev*	St Dev (in)**
Thyroid	--	--	0.63	--	--
Breast (gland)	23.69	17.42	20.31	3.16	--
Breast (skin)	26.17	7.26	18.06	8.22	2.43
Lung	20.20	2.72	11.37	9.44	0.96
Liver	28.12	23.60	25.48	1.78	--
Stomach	--	--	28.16	--	--
Small Intestine	--	--	19.18	--	--
Colon	30.80	26.86	28.83	2.79	--
Ovary	--	--	3.41	--	--
Skin	30.58	25.39	27.20	2.93	--

\*Standard deviation is taken for all dosimeters placed in or on an organ.

\*\*Standard deviation (in) is calculated only for those organ dosimeters located within the primary x-ray beam.

Table 7-16. Organ doses for abdomen protocol and large subject.

	Organ Dose (mGy)				
	Max	Min	Ave	St Dev*	St Dev (in)**
Thyroid	--	--	1.36	--	--
Breast (gland)	24.55	12.38	19.85	5.55	2.35
Breast (skin)	29.54	4.54	19.89	10.13	2.76
Lung	23.00	6.20	14.04	8.90	1.85
Liver	29.04	21.70	26.08	2.80	--
Stomach	--	--	31.38	--	--
Small Intestine	--	--	31.92	--	--
Colon	30.84	29.38	30.11	1.03	--
Ovary	--	--	4.99	--	--
Skin	32.05	31.03	31.52	0.51	--

\*Standard deviation is taken for all dosimeters placed in or on an organ.

\*\*Standard deviation (in) is calculated only for those organ dosimeters located within the primary x-ray beam.

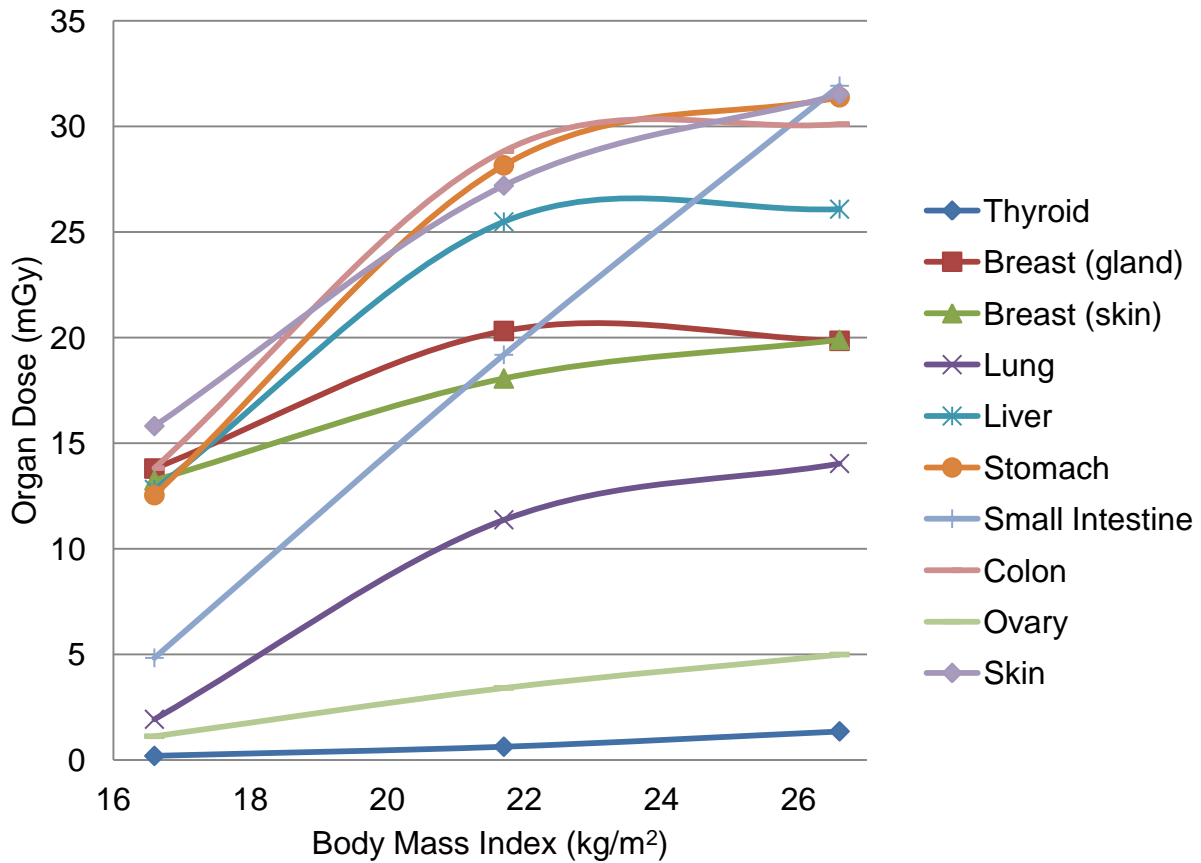


Figure 7-3. Organ dose versus BMI for abdomen protocol.

Table 7-17. Organ doses for pelvis protocol and small subject.

	Organ Dose (mGy)			
	Max	Min	Ave	St Dev
Thyroid	--	--	0.05	--
Breast (gland)	0.77	0.55	0.65	0.11
Breast (skin)	1.63	0.38	0.92	0.45
Lung	0.24	0.09	0.16	0.08
Liver	7.46	1.85	4.87	2.02
Stomach	--	--	2.70	--
Small Intestine	--	--	13.62	--
Colon	13.85	7.14	10.50	4.75
Ovary	--	--	12.66	--
Skin	18.20	12.00	15.44	3.16

Table 7-18. Organ doses for pelvis protocol and medium subject.

	Organ Dose (mGy)			
	Max	Min	Ave	St Dev
Thyroid	--	--	0.06	--
Breast (gland)	0.46	0.30	0.36	0.09
Breast (skin)	1.07	0.28	0.63	0.30
Lung	0.38	0.16	0.26	0.13
Liver	1.56	0.66	1.03	0.47
Stomach	--	--	0.95	--
Small Intestine	--	--	26.10	--
Colon	11.19	10.76	10.97	0.30
Ovary	--	--	20.69	--
Skin	31.59	27.67	29.49	1.97

Table 7-19. Organ doses for pelvis protocol and large subject.

	Organ Dose (mGy)			
	Max	Min	Ave	St Dev
Thyroid	--	--	0.05	--
Breast (gland)	0.46	0.28	0.39	0.07
Breast (skin)	1.09	0.18	0.55	0.33
Lung	0.59	0.11	0.38	0.25
Liver	1.33	0.78	1.12	0.22
Stomach	--	--	3.27	--
Small Intestine	--	--	23.29	--
Colon	24.34	5.28	14.81	13.48
Ovary	--	--	26.57	--
Skin	34.91	21.79	28.07	6.58

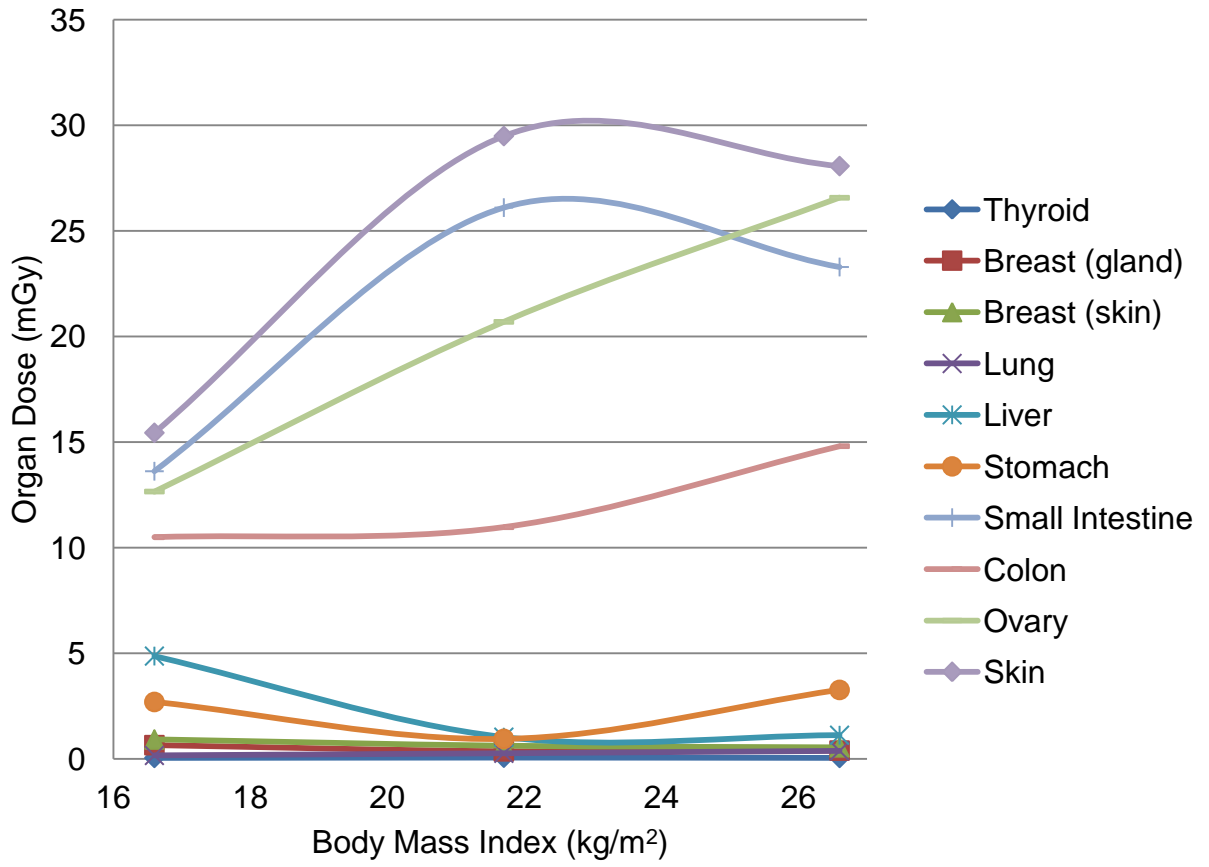


Figure 7-4. Organ dose versus BMI for pelvis protocol.

Table 7-20. Organ doses for three-phase liver protocol and small subject.

	Organ Dose (mGy)				
	Max	Min	Ave	St Dev*	St Dev (in)**
Thyroid	--	--	0.58	--	--
Breast (gland)	36.44	23.34	31.07	6.86	--
Breast (skin)	41.69	10.47	31.35	12.04	3.41
Lung	8.08	1.63	4.82	3.65	--
Liver	44.44	35.30	39.21	3.95	--
Stomach	--	--	38.86	--	--
Small Intestine	--	--	12.33	--	--
Colon	38.49	37.54	38.01	0.67	--
Ovary	--	--	2.52	--	--
Skin	41.38	26.97	34.21	7.21	--

\*Standard deviation is taken for all dosimeters placed in or on an organ.

\*\*Standard deviation (in) is calculated only for those organ dosimeters located within the primary x-ray beam.

Table 7-21. Organ doses for three-phase liver protocol and medium subject.

	Organ Dose (mGy)				
	Max	Min	Ave	St Dev*	St Dev (in)**
Thyroid	--	--	1.58	--	--
Breast (gland)	64.52	20.64	35.74	24.93	--
Breast (skin)	73.55	11.40	52.83	24.04	7.44
Lung	58.46	8.14	32.49	27.18	3.54
Liver	68.19	49.12	57.34	8.50	--
Stomach	--	--	69.79	--	--
Small Intestine	--	--	23.04	--	--
Colon	73.63	68.28	70.96	3.78	--
Ovary	--	--	4.47	--	--
Skin	76.22	49.50	64.02	13.51	--

\*Standard deviation is taken for all dosimeters placed in or on an organ.

\*\*Standard deviation (in) is calculated only for those organ dosimeters located within the primary x-ray beam.

Table 7-22. Organ doses for three-phase liver protocol and large subject.

	Organ Dose (mGy)				
	Max	Min	Ave	St Dev*	St Dev (in)**
Thyroid	--	--	4.15	--	--
Breast (gland)	60.89	29.45	53.05	14.38	6.24
Breast (skin)	78.70	11.95	58.58	26.94	7.85
Lung	70.55	17.98	42.23	27.92	6.14
Liver	88.01	71.46	79.32	6.51	--
Stomach	--	--	78.38	--	--
Small Intestine	--	--	60.06	--	--
Colon	74.98	60.26	67.62	10.41	--
Ovary	--	--	2.42	--	--
Skin	98.56	69.98	77.95	12.03	--

\*Standard deviation is taken for all dosimeters placed in or on an organ.

\*\*Standard deviation (in) is calculated only for those organ dosimeters located within the primary x-ray beam.

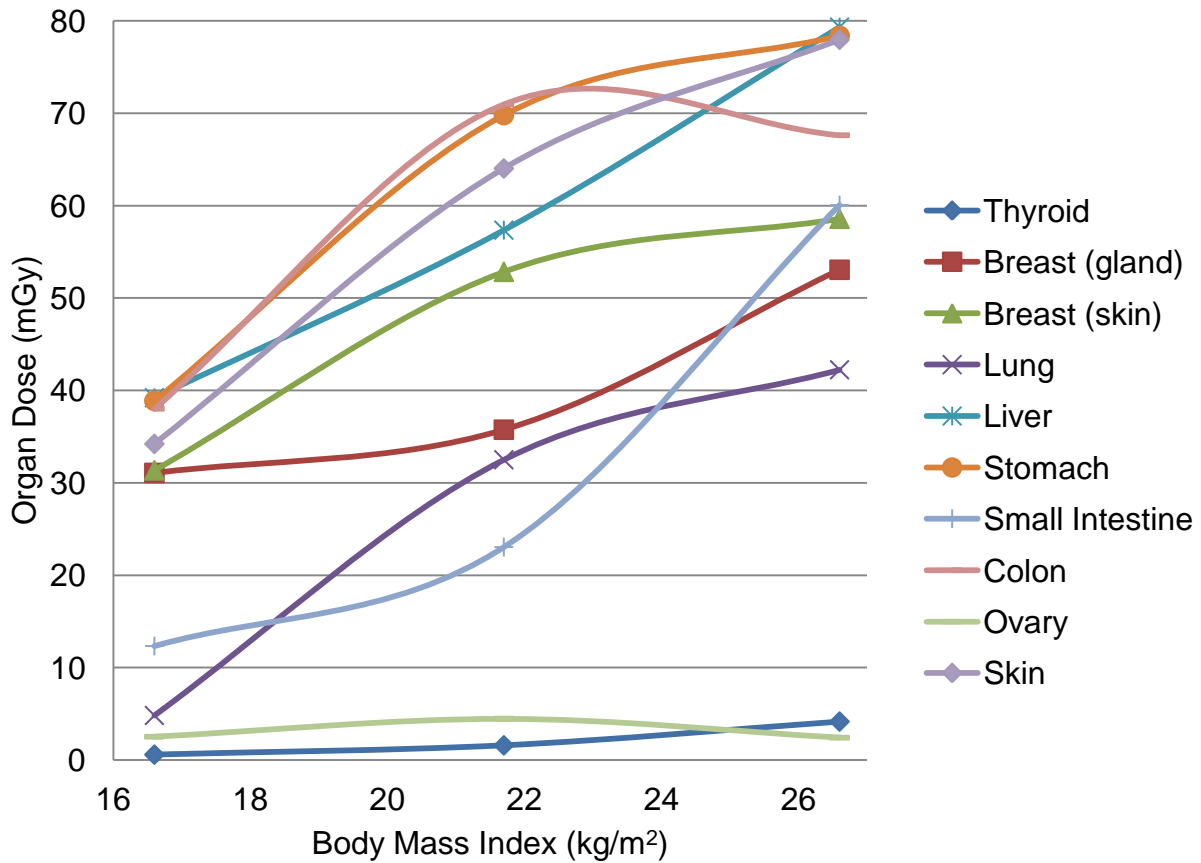


Figure 7-5. Organ dose versus BMI for three-phase liver protocol.

Table 7-23. Organ doses for helical CTA protocol and small subject.

	Organ Dose (mGy)			
	Max	Min	Ave	St Dev
Thyroid	--	--	14.93	--
Breast (gland)	36.57	32.62	34.50	1.98
Breast (skin)	42.78	20.08	33.31	9.52
Lung	33.76	32.01	33.13	0.81
Liver	26.27	7.80	13.36	7.41
Stomach	--	--	13.79	--
Small Intestine	--	--	1.34	--
Colon	5.57	4.78	5.18	0.56
Ovary	--	--	0.57	--
Skin	53.66	29.31	40.50	12.29

Table 7-24. Organ doses for helical CTA protocol and medium subject.

	Organ Dose (mGy)			
	Max	Min	Ave	St Dev
Thyroid	--	--	7.88	--
Breast (gland)	33.33	29.58	31.74	1.94
Breast (skin)	40.20	25.57	30.46	6.20
Lung	34.58	33.19	33.68	0.63
Liver	36.02	31.65	33.53	1.92
Stomach	--	--	35.57	--
Small Intestine	--	--	5.10	--
Colon	15.59	12.06	13.82	2.49
Ovary	--	--	1.06	--
Skin	46.60	30.55	38.57	11.35

Table 7-25. Organ doses for helical CTA protocol and large subject.

	Organ Dose (mGy)			
	Max	Min	Ave	St Dev
Thyroid	--	--	33.20	--
Breast (gland)	35.51	28.54	31.28	2.94
Breast (skin)	30.95	24.89	27.91	2.14
Lung	31.74	18.66	23.26	5.94
Liver	20.96	8.20	15.08	6.08
Stomach	--	--	6.86	--
Small Intestine	--	--	2.77	--
Colon	3.16	2.48	2.82	0.48
Ovary	--	--	0.25	--
Skin	37.90	30.95	34.43	4.92

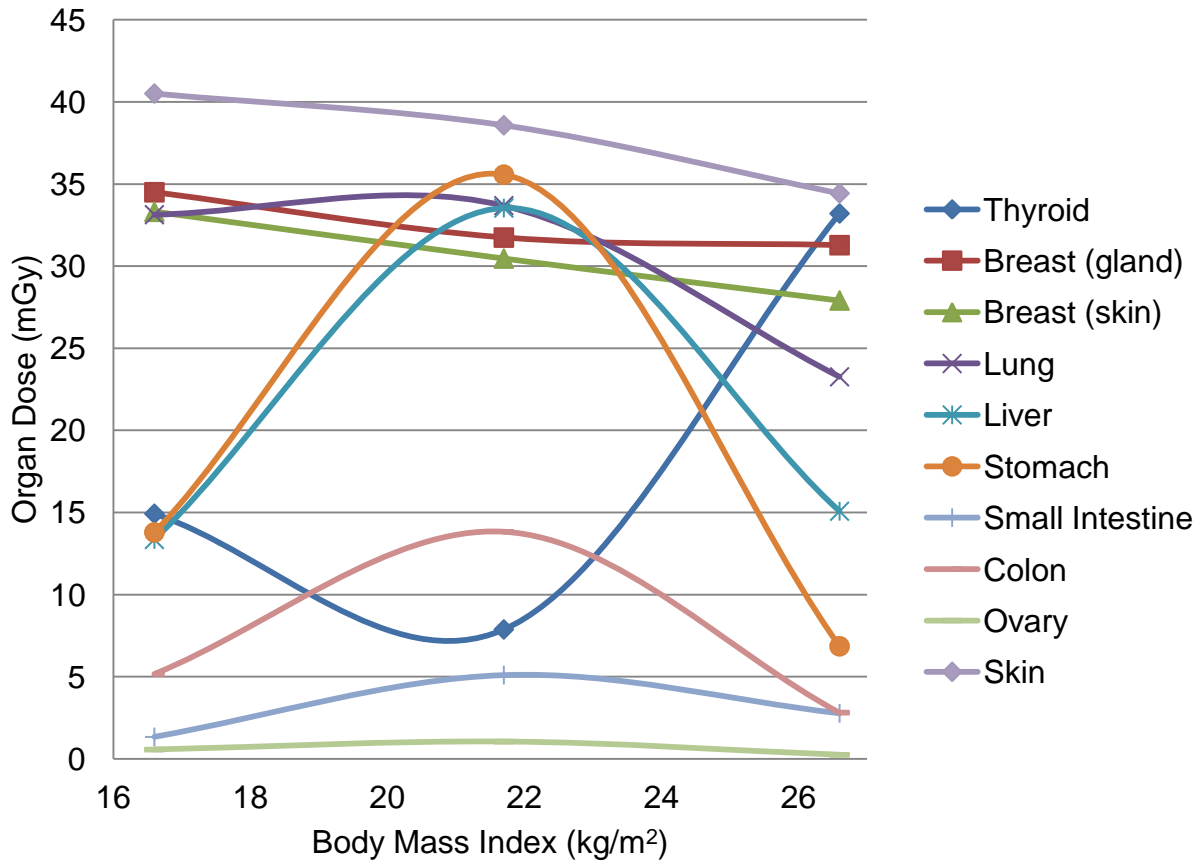


Figure 7-6. Organ dose versus BMI for helical CTA protocol.

Table 7-26. Organ doses for prospectively-gated CTA protocol and small subject.

	Organ Dose (mGy)				
	Max	Min	Ave	St Dev*	St Dev (in)**
Thyroid	--	--	2.45	--	--
Breast (gland)	17.09	15.10	15.82	1.10	--
Breast (skin)	34.52	5.67	15.74	10.95	--
Lung	19.92	4.24	12.13	8.77	0.28
Liver	8.09	3.46	4.92	1.85	--
Stomach	--	--	4.56	--	--
Small Intestine	--	--	1.17	--	--
Colon	2.69	2.04	2.37	0.46	--
Ovary	--	--	0.81	--	--
Skin	25.62	20.62	23.12	2.50	--

\*Standard deviation is taken for all dosimeters placed in or on an organ.

\*\*Standard deviation (in) is calculated only for those organ dosimeters located within the primary x-ray beam.

Table 7-27. Organ doses for prospectively-gated CTA protocol and medium subject.

	Organ Dose (mGy)				
	Max	Min	Ave	St Dev*	St Dev (in)**
Thyroid	--	--	1.56	--	--
Breast (gland)	24.63	19.01	21.24	2.98	--
Breast (skin)	19.97	5.04	14.51	5.62	2.20
Lung	14.44	10.03	12.42	1.82	--
Liver	12.33	3.52	9.10	4.32	0.10
Stomach	--	--	6.44	--	--
Small Intestine	--	--	1.91	--	--
Colon	3.09	0.77	1.93	1.64	--
Ovary	--	--	0.77	--	--
Skin	21.26	14.22	18.28	3.64	--

\*Standard deviation is taken for all dosimeters placed in or on an organ.

\*\*Standard deviation (in) is calculated only for those organ dosimeters located within the primary x-ray beam.

Table 7-28. Organ doses for prospectively-gated CTA protocol and large subject.

	Organ Dose (mGy)			
	Max	Min	Ave	St Dev
Thyroid	--	--	3.12	--
Breast (gland)	17.06	10.15	11.57	3.27
Breast (skin)	30.12	3.37	12.98	10.18
Lung	9.49	6.37	7.98	1.70
Liver	9.65	4.19	6.38	2.12
Stomach	--	--	2.55	--
Small Intestine	--	--	2.05	--
Colon	2.43	1.12	1.78	0.92
Ovary	--	--	0.25	--
Skin	30.12	28.04	29.08	0.86

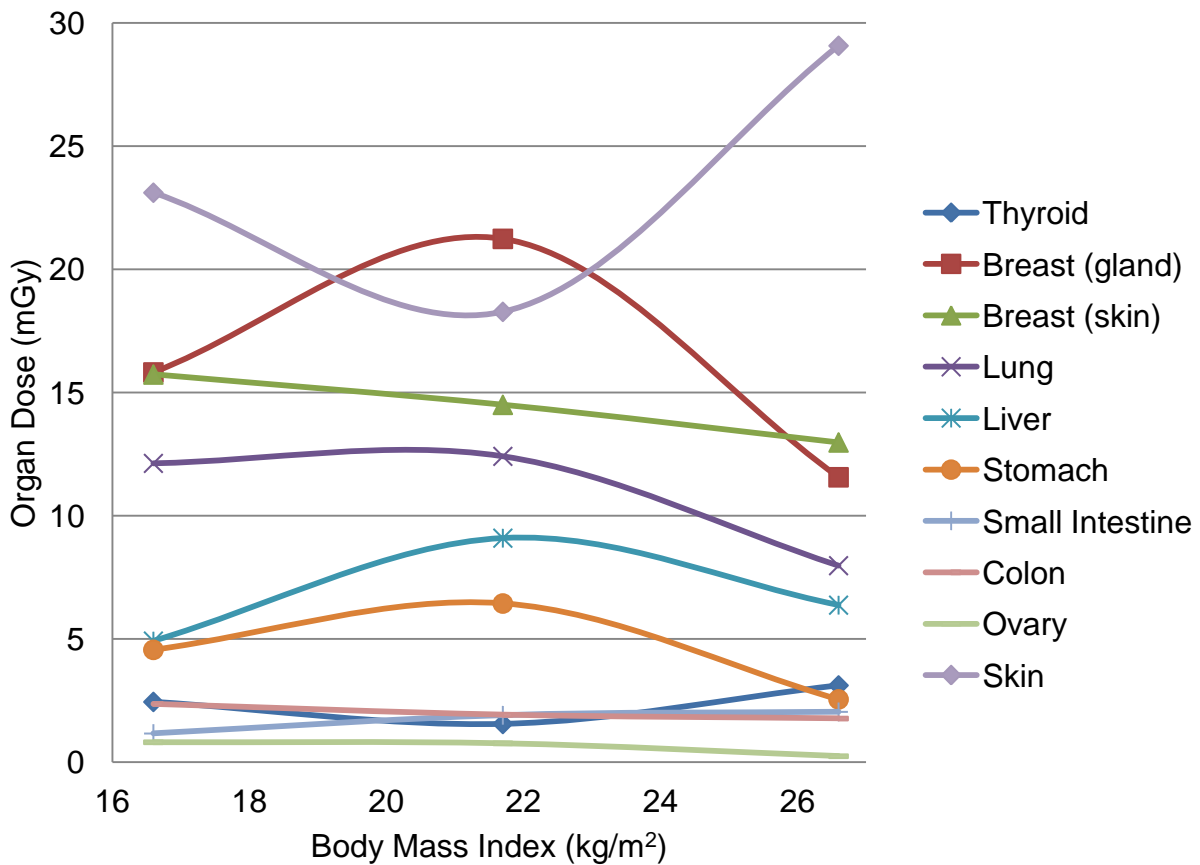


Figure 7-7. Organ dose versus BMI for prospectively-gated CTA protocol.

Table 7-29. Organ doses for cardiac functional analysis protocol without dose modulation and small subject.

	Organ Dose (mGy)				
	Max	Min	Ave	St Dev*	St Dev (in)**
Thyroid	--	--	3.68	--	--
Breast (gland)	52.95	45.61	49.81	3.78	--
Breast (skin)	74.59	15.37	42.15	21.58	--
Lung	52.80	10.48	31.54	23.53	1.28
Liver	20.32	5.56	9.62	6.08	--
Stomach	--	--	7.83	--	--
Small Intestine	--	--	1.65	--	--
Colon	4.50	4.23	4.36	0.19	--
Ovary	--	--	0.58	--	--
Skin	75.48	54.41	61.96	11.74	--

\*Standard deviation is taken for all dosimeters placed in or on an organ.

\*\*Standard deviation (in) is calculated only for those organ dosimeters located within the primary x-ray beam.

Table 7-30. Organ doses for cardiac functional analysis protocol without dose modulation and medium subject.

	Organ Dose (mGy)				
	Max	Min	Ave	St Dev*	St Dev (in)**
Thyroid	--	--	5.27	--	--
Breast (gland)	69.86	57.82	63.56	6.04	--
Breast (skin)	69.16	10.59	45.34	21.31	10.13
Lung	41.05	35.39	38.63	2.86	--
Liver	23.38	9.89	16.87	6.62	1.27
Stomach	--	--	17.65	--	--
Small Intestine	--	--	2.04	--	--
Colon	4.01	1.56	2.78	1.73	--
Ovary	--	--	0.58	--	--
Skin	70.05	42.02	59.33	15.13	--

\*Standard deviation is taken for all dosimeters placed in or on an organ.

\*\*Standard deviation (in) is calculated only for those organ dosimeters located within the primary x-ray beam.

Table 7-31. Organ doses for cardiac functional analysis protocol without dose modulation and large subject.

	Organ Dose (mGy)				
	Max	Min	Ave	St Dev*	St Dev (in)**
Thyroid	--	--	9.58	--	--
Breast (gland)	68.67	58.06	61.25	4.99	--
Breast (skin)	67.12	18.80	53.85	19.99	4.63
Lung	64.46	48.78	57.28	7.96	--
Liver	27.99	10.15	17.32	7.02	--
Stomach	--	--	9.26	--	--
Small Intestine	--	--	3.51	--	--
Colon	4.01	2.89	3.45	0.79	--
Ovary	--	--	0.54	--	--
Skin	83.59	62.25	69.42	9.65	--

\*Standard deviation is taken for all dosimeters placed in or on an organ.

\*\*Standard deviation (in) is calculated only for those organ dosimeters located within the primary x-ray beam.

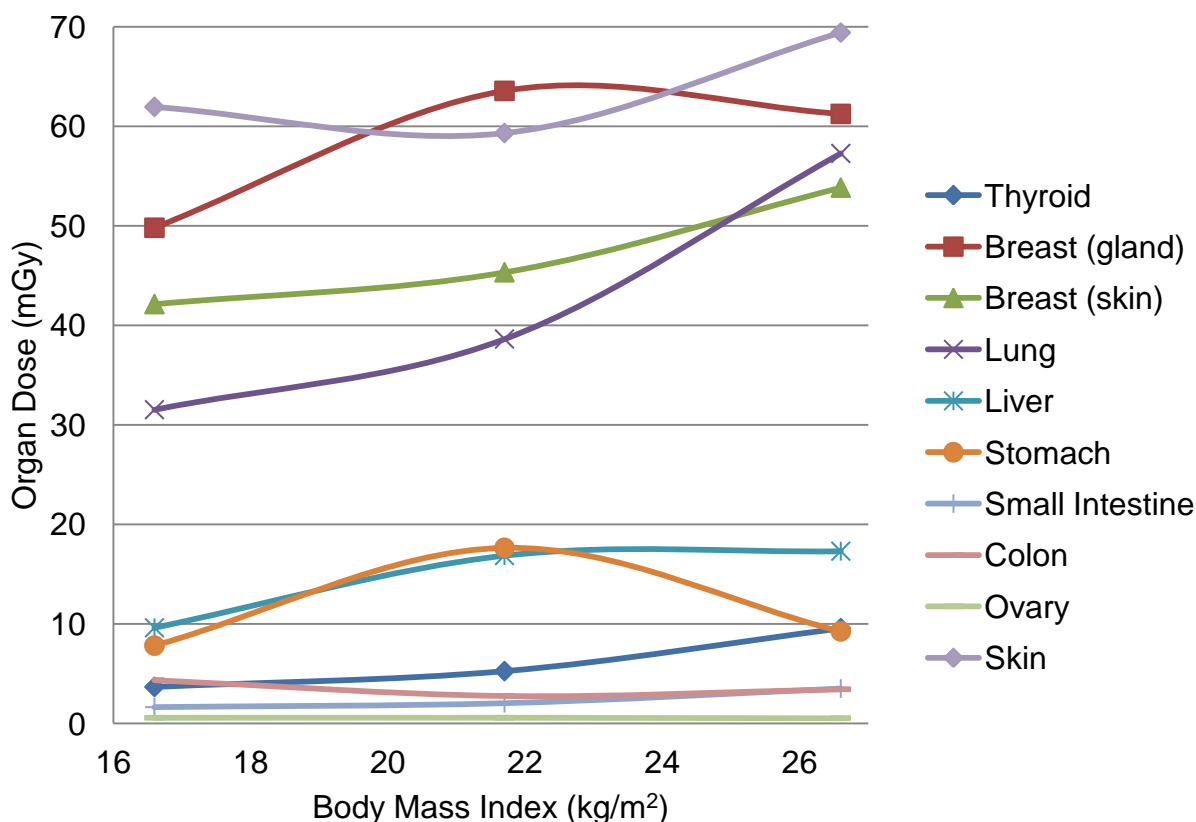


Figure 7-8. Organ dose versus BMI for cardiac functional analysis protocol without dose modulation.

Table 7-32. Organ doses for cardiac functional analysis protocol with dose modulation and small subject.

	Organ Dose (mGy)				
	Max	Min	Ave	St Dev*	St Dev (in)**
Thyroid	--	--	2.44	--	--
Breast (gland)	28.76	25.07	27.11	1.87	--
Breast (skin)	47.10	9.41	22.56	14.82	--
Lung	34.87	6.76	20.85	16.09	0.11
Liver	10.36	4.57	6.32	2.30	--
Stomach	--	--	6.61	--	--
Small Intestine	--	--	1.87	--	--
Colon	3.29	3.01	3.15	0.20	--
Ovary	--	--	0.94	--	--
Skin	38.89	31.37	35.43	3.80	--

\*Standard deviation is taken for all dosimeters placed in or on an organ.

\*\*Standard deviation (in) is calculated only for those organ dosimeters located within the primary x-ray beam.

Table 7-33. Organ doses for cardiac functional analysis protocol with dose modulation and medium subject.

	Organ Dose (mGy)				
	Max	Min	Ave	St Dev*	St Dev (in)**
Thyroid	--	--	3.15	--	--
Breast (gland)	36.39	31.72	34.62	2.53	--
Breast (skin)	38.97	6.65	26.28	12.03	5.70
Lung	28.64	22.41	24.81	2.72	--
Liver	20.75	7.59	14.07	5.82	2.25
Stomach	--	--	10.03	--	--
Small Intestine	--	--	1.88	--	--
Colon	2.98	1.06	2.02	1.36	--
Ovary	--	--	0.52	--	--
Skin	41.65	32.47	38.47	5.20	--

\*Standard deviation is taken for all dosimeters placed in or on an organ.

\*\*Standard deviation (in) is calculated only for those organ dosimeters located within the primary x-ray beam.

Table 7-34. Organ doses for cardiac functional analysis protocol with dose modulation and large subject.

	Organ Dose (mGy)			
	Max	Min	Ave	St Dev
Thyroid	--	--	6.23	--
Breast (gland)	33.96	22.29	25.47	5.13
Breast (skin)	49.25	7.92	26.28	14.98
Lung	22.54	15.29	18.89	3.84
Liver	21.22	7.83	12.66	5.30
Stomach	--	--	4.44	--
Small Intestine	--	--	2.23	--
Colon	2.37	2.22	2.29	0.10
Ovary	--	--	0.22	--
Skin	70.54	49.25	59.89	15.06

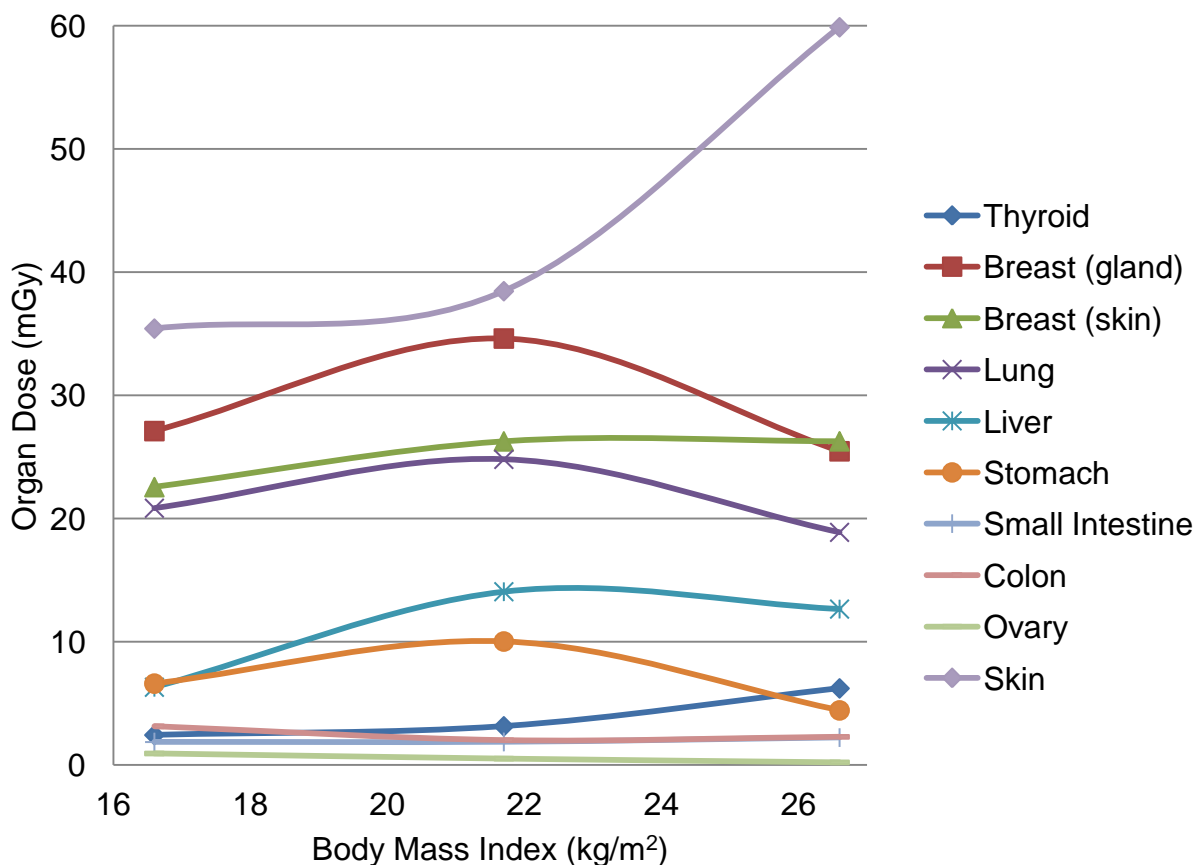


Figure 7-9. Organ dose versus BMI for cardiac functional analysis protocol with dose modulation.

Table 7-35. Comparison of organ doses (mGy) for CFA without and with dose modulation for small subject.

Organ	Protocol		
	CFA without dose modulation	CFA with dose modulation	Percent Reduction (%)
Thyroid	3.68	2.44	33.67%
Breast (gland)	49.81	27.11	45.57%
Breast (skin)	42.15	22.56	46.46%
Lung	31.54	20.85	33.89%
Liver	9.62	6.32	34.35%
Stomach	7.83	6.61	15.52%
Small Intestine	1.65	1.87	--
Colon	4.36	3.15	27.79%
Ovary	0.58	0.94	--
Skin	61.96	35.43	42.82%
Effective mAs	140	140	--
DLP (mGy*cm)	879.9	533.85	39.32%
Range (mm)	160	160	--

Table 7-36. Organ doses (mGy) for cardiac protocols and small subject.

Organ	Protocol			
	Helical CTA	Prospectively-gated CTA	CFA without dose modulation	CFA with dose modulation
Thyroid	14.93	2.45	3.68	2.44
Breast (gland)	34.50	15.82	49.81	27.11
Breast (skin)	33.31	15.74	42.15	22.56
Lung	33.13	12.13	31.54	20.85
Liver	13.36	4.92	9.62	6.32
Stomach	13.79	4.56	7.83	6.61
Small Intestine	1.34	1.17	1.65	1.87
Colon	5.18	2.37	4.36	3.15
Ovary	0.57	0.81	0.58	0.94
Skin	40.50	23.12	61.96	35.43
Effective mAs	534	140	140	140
DLP (mGy*cm)	788.55	279.6	879.9	533.85
Range (mm)	280.5	160	160	160

Table 7-37. Organ dose (mGy) comparison for volumetric cardiac protocols on Aquilion ONE for phantom measurements<sup>72</sup>, Monte Carlo (MC) simulations<sup>48</sup>, and cadaveric measurements.

Organ	Medium	Protocol		
		Prospectively-gated CTA	CFA without dose modulation	CFA with dose modulation
Thyroid	Phantom	2.50	7.81	4.61
	MC	2.76	8.12	4.88
	Cadaver*	1.56, 2.00	5.27, 6.50	3.15, 4.20
Lung	Phantom	13.94	43.77	26.07
	MC	15.21	44.76	26.90
	Cadaver*	12.42, 11.50	38.63, 44.50	24.81, 23.80
Stomach	Phantom	2.08	6.25	3.73
	MC	2.97	8.75	5.26
	Cadaver*	6.44, 5.80	17.65, 16.00	10.03, 9.00
Skin	Phantom	21.29	69.98	41.84
	MC	17.34	51.02	30.66
	Cadaver*	18.28, 20.80	59.33, 62.00	38.47, 44.00

\*Cadaveric organ doses are reported with measurements made with the medium subject (BMI 21.7), and for data extrapolated for a BMI of 23.5, consistent with the patient size used for phantom measurements and MC simulations.

Table 7-38. Organ doses for chest perfusion protocol and small subject.

	Organ Dose (mGy)				
	Max	Min	Ave	St Dev*	St Dev (in)**
Thyroid	--	--	10.43	--	--
Breast (gland)	32.01	21.79	28.29	5.65	--
Breast (skin)	95.36	10.40	30.72	36.25	--
Lung	94.46	34.13	56.65	28.81	21.68
Liver	14.82	6.65	9.71	3.06	--
Stomach	--	--	9.96	--	--
Small Intestine	--	--	3.11	--	--
Colon	5.60	4.51	5.05	0.76	--
Ovary	--	--	1.76	--	--
Skin	143.37	106.32	120.57	19.95	--

\*Standard deviation is taken for all dosimeters placed in or on an organ.

\*\*Standard deviation (in) is calculated only for those organ dosimeters located within the primary x-ray beam.

Table 7-39. Organ doses for chest perfusion protocol and medium subject.

	Organ Dose (mGy)				
	Max	Min	Ave	St Dev*	St Dev (in)**
Thyroid	--	--	7.77	--	--
Breast (gland)	96.89	76.47	89.71	11.48	--
Breast (skin)	102.73	13.24	72.59	34.54	11.10
Lung	76.90	59.28	70.03	7.68	3.37
Liver	50.38	8.46	27.41	18.00	9.29
Stomach	--	--	24.69	--	--
Small Intestine	--	--	1.30	--	--
Colon	3.40	1.52	2.46	1.33	--
Ovary	--	--	0.24	--	--
Skin	133.28	80.32	99.11	29.64	--

\*Standard deviation is taken for all dosimeters placed in or on an organ.

\*\*Standard deviation (in) is calculated only for those organ dosimeters located within the primary x-ray beam.

Table 7-40. Organ doses for chest perfusion protocol and large subject.

	Organ Dose (mGy)				
	Max	Min	Ave	St Dev*	St Dev (in)**
Thyroid	--	--	30.85	--	--
Breast (gland)	86.59	46.13	67.19	18.49	8.78
Breast (skin)	98.68	9.26	53.88	35.11	28.53
Lung	90.81	20.59	49.94	33.57	18.98
Liver	20.80	8.13	13.27	4.94	4.02
Stomach	--	--	6.62	--	--
Small Intestine	--	--	1.98	--	--
Colon	3.26	1.32	2.29	1.37	--
Ovary	--	--	0.16	--	--
Skin	125.57	98.00	112.18	13.80	--

\*Standard deviation is taken for all dosimeters placed in or on an organ.

\*\*Standard deviation (in) is calculated only for those organ dosimeters located within the primary x-ray beam.

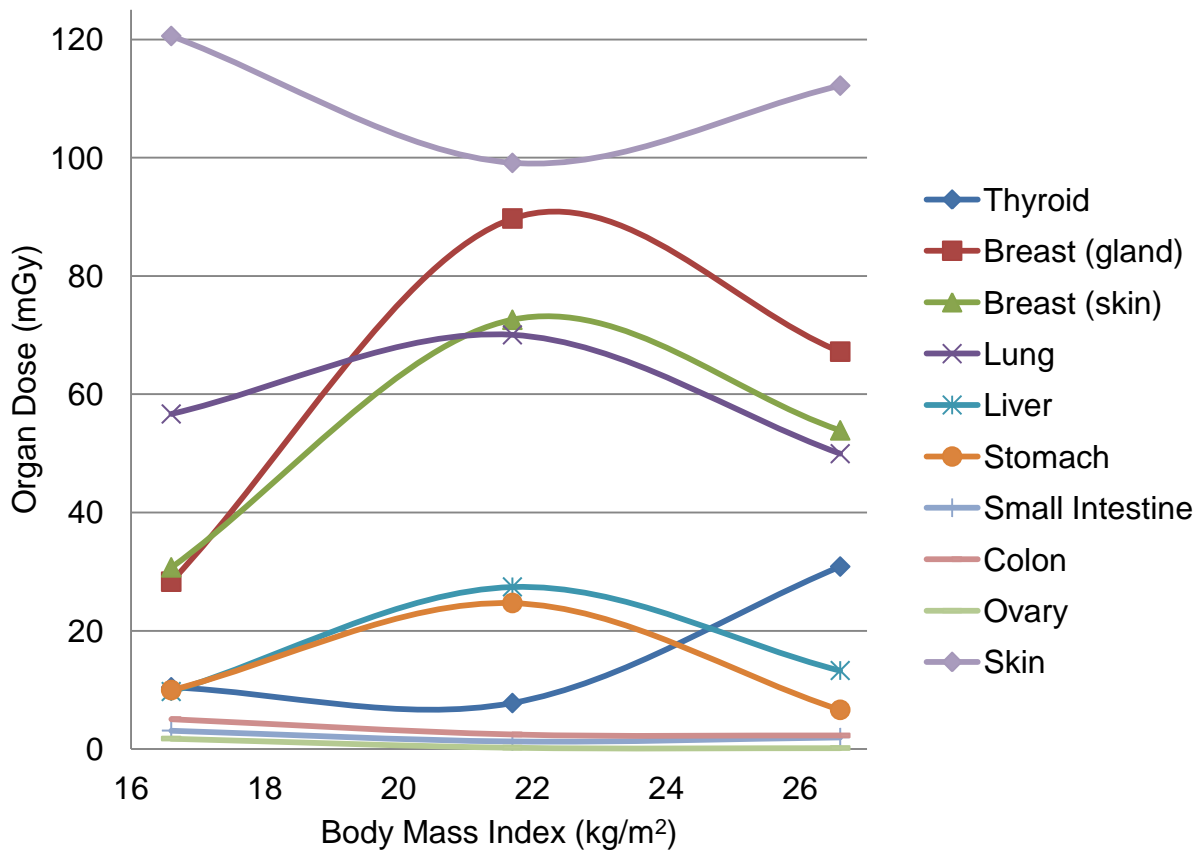


Figure 7-10. Organ dose versus BMI for chest perfusion protocol.

Table 7-41. Organ doses for liver perfusion protocol and small subject.

	Organ Dose (mGy)				
	Max	Min	Ave	St Dev*	St Dev (in)**
Thyroid	--	--	0.98	--	--
Breast (gland)	109.95	52.02	73.75	31.56	--
Breast (skin)	129.48	17.09	94.91	45.34	14.74
Lung	15.94	3.20	9.48	6.73	0.93
Liver	143.93	92.63	120.26	19.58	13.89
Stomach	--	--	105.76	--	--
Small Intestine	--	--	8.75	--	--
Colon	103.85	27.28	65.56	54.14	--
Ovary	--	--	3.27	--	--
Skin	151.28	118.19	134.16	16.57	--

\*Standard deviation is taken for all dosimeters placed in or on an organ.

\*\*Standard deviation (in) is calculated only for those organ dosimeters located within the primary x-ray beam.

Table 7-42. Organ doses for liver perfusion protocol and medium subject.

	Organ Dose (mGy)				
	Max	Min	Ave	St Dev*	St Dev (in)**
Thyroid	--	--	1.44	--	--
Breast (gland)	40.39	18.05	26.46	12.15	--
Breast (skin)	118.49	10.36	76.71	49.49	5.56
Lung	74.71	8.90	39.01	34.32	8.94
Liver	106.18	79.89	88.23	10.31	--
Stomach	--	--	106.64	--	--
Small Intestine	--	--	5.87	--	--
Colon	14.58	12.96	13.77	1.15	--
Ovary	--	--	1.51	--	--
Skin	109.16	91.76	99.03	9.04	--

\*Standard deviation is taken for all dosimeters placed in or on an organ.

\*\*Standard deviation (in) is calculated only for those organ dosimeters located within the primary x-ray beam.

Table 7-43. Organ doses for liver perfusion protocol and large subject.

	Organ Dose (mGy)				
	Max	Min	Ave	St Dev*	St Dev (in)**
Thyroid	--	--	1.41	--	--
Breast (gland)	14.64	7.69	11.05	3.11	--
Breast (skin)	27.55	2.99	10.81	9.64	--
Lung	36.79	5.58	17.90	15.14	9.41
Liver	105.02	64.50	79.79	15.47	--
Stomach	--	--	95.49	--	--
Small Intestine	--	--	18.12	--	--
Colon	59.97	12.70	36.34	33.43	--
Ovary	--	--	1.70	--	--
Skin	136.87	85.03	105.09	27.84	--

\*Standard deviation is taken for all dosimeters placed in or on an organ.

\*\*Standard deviation (in) is calculated only for those organ dosimeters located within the primary x-ray beam.

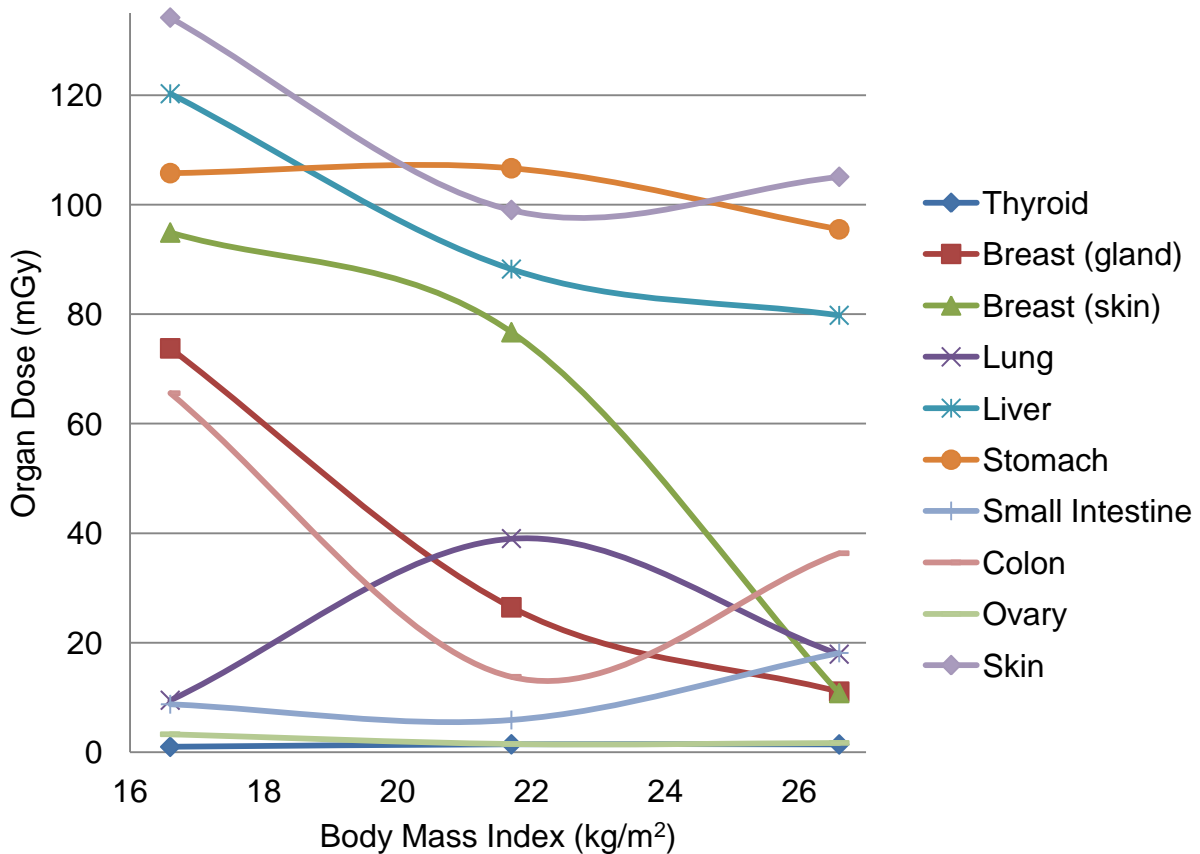


Figure 7-11. Organ dose versus BMI for liver perfusion protocol.

Table 7-44. Organ doses for pancreas perfusion protocol and small subject.

	Organ Dose (mGy)			
	Max	Min	Ave	St Dev*
Thyroid	--	--	0.53	--
Breast (gland)	25.49	16.21	20.14	4.80
Breast (skin)	88.63	10.86	32.49	31.98
Lung	6.92	1.41	4.27	2.91
Liver	94.55	74.79	83.74	7.38
Stomach	--	--	82.64	--
Small Intestine	--	--	11.79	--
Colon	60.76	48.10	54.43	8.95
Ovary	--	--	4.06	--
Skin	85.39	72.00	79.01	6.72

Table 7-45. Organ doses for pancreas perfusion protocol and medium subject.

	Organ Dose (mGy)			
	Max	Min	Ave	St Dev
Thyroid	--	--	0.70	--
Breast (gland)	15.86	9.79	11.87	3.45
Breast (skin)	85.23	4.50	27.67	32.60
Lung	26.09	4.06	14.63	11.94
Liver	67.14	45.76	57.84	9.32
Stomach	--	--	77.85	--
Small Intestine	--	--	5.96	--
Colon	16.35	14.35	15.35	1.42
Ovary	--	--	1.26	--
Skin	88.63	65.54	73.87	12.82

Table 7-46. Organ doses for pancreas perfusion protocol and large subject.

	Organ Dose (mGy)				
	Max	Min	Ave	St Dev*	St Dev (in)**
Thyroid	--	--	0.24	--	--
Breast (gland)	2.23	1.44	1.90	0.37	--
Breast (skin)	4.37	0.60	2.06	1.39	--
Lung	4.72	0.86	2.58	1.91	--
Liver	11.92	6.59	9.80	2.09	0.45
Stomach	--	--	30.85	--	--
Small Intestine	--	--	68.62	--	--
Colon	67.44	60.17	63.81	5.14	--
Ovary	--	--	6.02	--	--
Skin	81.30	72.80	75.72	4.83	--

\*Standard deviation is taken for all dosimeters placed in or on an organ.

\*\*Standard deviation (in) is calculated only for those organ dosimeters located within the primary x-ray beam.

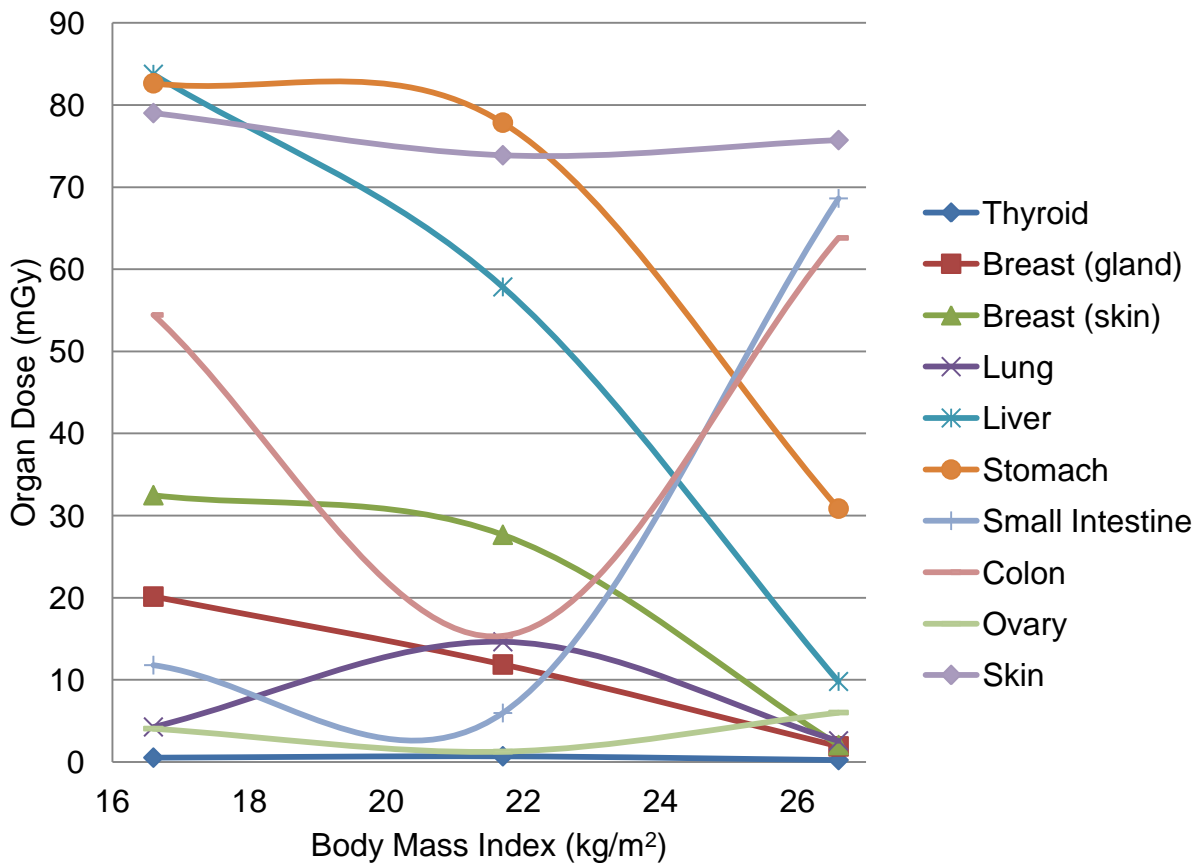


Figure 7-12. Organ dose versus BMI for pancreas perfusion protocol.

## CHAPTER 8 SUMMARY AND CONCLUSIONS

### **8.1 Summary**

The main goal of this research project was to develop a methodology that would allow direct measurement of radiation doses within a human body. Successfully attaining this goal would result in the ability to accurately and directly measure organ dose data from CT exams without estimation or simulation, something that has previously been accomplished. To this extent, the project has been a success, and a total of twelve separate CT exams have been investigated utilizing three cadaveric subjects of varying sizes. The organ doses measured for each exam and each subject have been measured and reported herein.

The methodology created and utilized for this project was relatively straightforward. From the beginning, it was known that OSL nanoDot dosimeters (Landauer, Glenwood IL) were going to be utilized to make dose measurements, as this dosimetry system had already been fully characterized for use with CT dosimetry.<sup>72</sup> It was also certain that the Aquilion ONE scanner (Toshiba America Medical Systems, Newport Beach, CA) was the CT scanner to be investigated, as it represents the current state-of-the-art in CT technology, and has the ability to perform both helical and broad beam image acquisitions. Although both the nanoDots and Aquilion ONE had been the subject of much previous research, what separates this project from all others is the manner in which living patients were represented. Rather than using a physical phantom or computational data sets, this project diverged from current standards by using cadaveric subjects to represent live patients.

The first major issue was, therefore, to determine a way to place the dosimeters inside a cadaver. After much trial and error, a dosimetry placement system consisting of an outer placement tube and an inner dosimeter holder was developed and tested. The placement tube would be inserted into the subject at a predetermined position. Once the positioning was deemed appropriate, the placement tube was affixed and remained stationary for the remainder of the project. The dosimeter holder would allow the dosimeters to be inserted into the placement tube prior to scanning, and would be withdrawn after the CT scan was completed. This system also allowed validation of the dose measurement positions by use of a system of verification tubes, which were constructed with metal fiducial markers in place of the dosimeters. If there was ever a question or concern about where the dosimeter was being placed, or if the placement tube shifted position, the verification tubes were inserted and scanned. This allowed consistent placement of the dosimeters for all CT exams.

Once the placement system was finished, embalmed cadaveric subjects were acquired. Whole body CT exams were performed to visualize the anatomy and assist in tube placement planning. The first specimen was used to investigate the number of measurements and scans necessary to obtain accurate average organ doses. This optimization proved fruitful, as it greatly reduced the number of placement tubes, dosimeters, and repeat CT exams.

In all, three embalmed female cadavers were utilized to make organ dose measurements. Twelve separate CT exams were performed on each subject. All organ doses were adjusted via energy and scatter correction factors, and doses were reported for each subject-exam combination. Doses as a function of BMI were also reported to

illustrate the impact that patient size has for different exams. While it was expected that larger patients receive more exposure, this was only partly true, especially for exams with limited scanning ranges.

Comparison of organ doses from various exams proved simple and effective once the doses were reported. It was easy to see that, for cardiac exams, the two volumetric protocols (prospectively-gated CTA and CFA with dose modulation) are the exams that should be performed, depending on whether or not functional data is required. These two exams resulted in much lower organ doses than their competing exams (helical CTA and CFA without dose modulation, respectively). While in-depth comparisons between all exams was not performed within the context of this project, the organ dose values reported here could (and should) be used in future studies and comparisons of CT protocols. In this way, these directly measured organ doses represent the most accurate and reliable dose metric both for CT protocol optimization, as well as for risk versus benefit analysis and the related appropriateness criteria.

## **8.2 Future Work**

### **8.2.1 Benchmark for Phantoms and Simulations**

The major impulse that brought about the idea for this work was the thought that, even though much time and energy has gone into producing tomographic and computational phantoms, no study has been performed to actually determine how closely these mimic live patients. It was always thought that the results from this project could be used as a benchmark to compare the results of other work using phantoms and simulations. In this way, it would be possible for those working with phantom measurements to have a known degree of certainty in their dose results, and to possibly create correction factors that convert phantom doses to patient doses.

The main problem with comparing the cadaver/patient doses to those measured from simulations are the differences in anatomy from patient to patient. Physical phantoms only represent “standard” or “average” patients and are generally constructed using the data set from one patient. Computational phantoms are also modeled after an average patient size, but as computing power increases, the simulated patients may be morphed to fit various patient sizes and organ positions. It would be worthwhile, in the author’s mind, to create either a computational or physical phantom (or both) based on a CT data set from the medium subject used in this project. The validation tubes show the exact dose measurement locations within each organ, and would allow one-to-one comparison of results. In this manner, it would be possible to determine what corrections (if any) would need to be made to simulated/estimated doses to provide accurate and reliable patient doses.

### **8.2.2 Size-specific Dose Estimates**

The purpose of using three various-sized subjects in this project was to allow comparison of doses as the body size changed. Recently, a task group of the American Association of Physicists in Medicine (AAPM) released their preliminary report concerning patient size-specific dose estimates (SSDEs) from CT scans.<sup>79</sup> This report utilized research performed by four different medical physics groups, each utilizing different methodologies to estimate CT doses. While their work is impressive, it suffers from the same condition that plagues other current estimates, namely there is no way to tell how closely their results represent the dose to actual patients. For this reason, it would be extremely interesting to research their suggestion for calculating SSDEs and comparing their results to those obtained in this project.

### **8.2.3 Additional Cadaveric Subjects**

Since a large part of this project entailed the creation of a methodology and placement system to allow dose measurements within a cadaver, it stands to reason that this methodology could be used in additional ways. More organ dose data could be acquired using the optimized methodology on additional subjects. These subjects could be of larger or smaller body size, and any results could be utilized in addition to those for the three subject BMIs in this project. In addition, it would also be worthwhile to have an organ dose comparison based upon gender. This would require two subjects of very similar BMIs and body sizes, but the anatomical differences would create differences in the organ doses in unknown ways.

### **8.2.4 Further Analysis**

A brief overview of Chapter 7 makes it obvious that there is a large amount of data that has been collected and reported during this project. Due to time restrictions (and attempting to keep this project from turning into two or three separate dissertations), the data has by no means been analyzed exhaustively. For this reason, it would be possible to look further into the reported organ doses, especially as they relate to both the effective mAs and DLP values. An apparent correlation between DLP and dose to organs in the primary beam was determined and commented upon for volumetric cardiac studies. It is the author's belief that if there existed a means by which to convert DLP values (reported by the CT scanner) into realistic, meaningful organ doses, it could greatly impact how dose is reported in CT imaging.

## **8.3 Final Thoughts**

The organ dose data collected during this research project represents information never before seen. Nowhere in the body of scientific literature is there evidence of

directly measured organ doses within a human body, living or otherwise. As such, this project has resulted in an original, unique, straightforward, and extremely useful methodology that allows direct organ dose measurement. This is of great importance at the current time, when CT imaging technology and application is growing at great speed. Accurate organ doses allow proper determination of the risks that arise from a CT exam. CT scans allow radiologists to diagnose disease and save lives but still need to be optimized to minimize risk while maximizing benefit. To that end, this research project has created a way to properly determine the risks, and thereby assess CT scans appropriately.

## LIST OF REFERENCES

1. Brenner DJ, Hall EJ. Computed tomography--an increasing source of radiation exposure. *N Engl J Med* 2007;357:2277-84.
2. Bogdanich W. Radiation Overdoses Point Up Dangers of CT Scans. *New York Times* 2009;Sect. A13.
3. Bogdanich W. At Hearing on Radiation, Calls for Better Oversight. *The New York Times* 2010;Sect. A12.
4. Neale T. CT Scan Radiation May Lead to 29,000 Cancers, Researchers Warn. In: December 15, 2009 ed. *medpagetoday.com: ABC News*; 2009.
5. Medical Radiation: An Overview of The Issues. In: Committee on Energy and Commerce. Washington, DC; 2010.
6. Modality Benchmark Reports. <http://www.imvinfo.com>, 2007. (Accessed April 5, 2011, at
7. IMV Medical Information Division I. IMV Benchmark Reports. In: IMV Medical Information Division, Des Plaines, IL; 2006.
8. Measurements NCoRPa. Ionizing Radiation Exposure of the Population of the United States. In; 2009.
9. Mettler FA, Thomadsen BR, Bhargavan M, et al. Medical radiation exposure in the U.S. in 2006: preliminary results. *Health Phys* 2008;95:502-7.
10. Inc. CoRCPD. Nationwide evaluation of x-ray trends (NEXT) 2000-2001 survey of patient radiation exposure from computed tomography in the United States. In; 2007.
11. Heiken JP, Peterson CM, Menias CO. Virtual colonoscopy for colorectal cancer screening: current status. *Cancer Imaging* 2005;5 Spec No A:S133-9.
12. Naghavi M, Falk E, Hecht HS, et al. From vulnerable plaque to vulnerable patient--Part III: Executive summary of the Screening for Heart Attack Prevention and Education (SHAPE) Task Force report. *Am J Cardiol* 2006;98:2H-15H.
13. Brenner D, Elliston C, Hall E, Berdon W. Estimated risks of radiation-induced fatal cancer from pediatric CT. *AJR Am J Roentgenol* 2001;176:289-96.
14. Shrimpton PC JD, Hillier MC, Wall BF, LeHeron JC, Faulkner K. Survey of CT practice in the UK. 2. Dosimetric aspects. In. Chilton, England: National Radiological Protection Board; 1991.

15. Berrington de González A, Darby S. Risk of cancer from diagnostic X-rays: estimates for the UK and 14 other countries. *Lancet* 2004;363:345-51.
16. Abrams HL, McNeil BJ. Medical implications of computed tomography. *N Engl J Med* 1978;298:255-61.
17. Lu J, Zhang M, Cao Y, et al. Three-dimensional whole-brain perfused blood volume imaging with multimodal CT for evaluation of acute ischaemic stroke. *Clin Radiol* 2011.
18. Brenner DJ, Elliston CD. Estimated radiation risks potentially associated with full-body CT screening. *Radiology* 2004;232:735-8.
19. Herman GT. *Image Resconstruction from Projections: The Fundamentals of Computerized Tomography*. New York, NY: Academic Press, Inc; 1980.
20. Bushberg JT, Siebert JA, Leidholdt Jr EM, Boone JM. *The Essential Physics of Medical Imaging*. Second ed. Philadelphia, PA: Lippincott Williams & Wilkins; 2002.
21. Mahesh M. Search for isotropic resolution in CT from conventional through multiple-row detector. *Radiographics* 2002;22:949-62.
22. Rubin GD, Napel S. Increased scan pitch for vascular and thoracic spiral CT. *Radiology* 1995;197:316-7.
23. Wright AR, Collie DA, Williams JR, Hashemi-Malayeri B, Stevenson AJ, Turnbull CM. Pulmonary nodules: effect on detection of spiral CT pitch. *Radiology* 1996;199:837-41.
24. Taylor SA, Halligan S, Bartram CI, et al. Multi-detector row CT colonography: effect of collimation, pitch, and orientation on polyp detection in a human colectomy specimen. *Radiology* 2003;229:109-18.
25. Toshiba Aquilion ONE: Volume Scanning. (Accessed April 18, 2011, at [www.medical.toshiba.com](http://www.medical.toshiba.com).)
26. Kalra MK, Maher MM, Toth TL, et al. Techniques and applications of automatic tube current modulation for CT. *Radiology* 2004;233:649-57.
27. Mulkens TH, Bellinck P, Baeyaert M, et al. Use of an automatic exposure control mechanism for dose optimization in multi-detector row CT examinations: clinical evaluation. *Radiology* 2005;237:213-23.
28. Iball GR, Brettle DS, Moore AC. Assessment of tube current modulation in pelvic CT. *Br J Radiol* 2006;79:62-70.

29. Tack D, De Maertelaer V, Gevenois PA. Dose reduction in multidetector CT using attenuation-based online tube current modulation. *AJR Am J Roentgenol* 2003;181:331-4.
30. McCollough CH, Bruesewitz MR, Kofler JM. CT dose reduction and dose management tools: overview of available options. *Radiographics* 2006;26:503-12.
31. Kalra MK, Rizzo S, Maher MM, et al. Chest CT performed with z-axis modulation: scanning protocol and radiation dose. *Radiology* 2005;237:303-8.
32. Papadakis AE, Perisinakis K, Damilakis J. Automatic exposure control in pediatric and adult multidetector CT examinations: a phantom study on dose reduction and image quality. *Med Phys* 2008;35:4567-76.
33. Shope TB, Gagne RM, Johnson GC. A method for describing the doses delivered by transmission x-ray computed tomography. *Med Phys* 1981;8:488-95.
34. US Food and Drug Agency. 21 CFR I 1020.33. In.
35. Leitz W, Axelsson B, Szendro G. Computed tomography dose assessment: a practical approach. *Radiation Protection Dosimetry* 1995;57:377-80.
36. American Association of Physicists in Medicine. Standardized Methods for Measuring Diagnostic X-ray Exposures; 1990.
37. McCollough CH. It is time to retire the computed tomography dose index (CTDI) for CT quality assurance and dose optimization. Against the proposition. *Med Phys* 2006;33:1190-1.
38. Buzug TM. *Computed Tomography: From Photon Statistics to Modern Cone-Beam CT*. Berlin: Springer-Verlag; 2008.
39. Dixon RL. A new look at CT dose measurement: beyond CTDI. *Med Phys* 2003;30:1272-80.
40. Boone JM. The trouble with CTD100. *Med Phys* 2007;34:1364-71.
41. International Commission on Radiological Protection. The 2007 Recommendations of the International Commission on Radiological Protection. ICRP Publication 103. *Ann. ICRP* 37 (2-4). 2007.
42. International Committee on Radiological Protection. 1990 Recommendations of the International Committee on Radiological Protection. ICRP Publication 60. *Ann. ICRP* 21 (1-3). 1991.
43. International Committee on Radiological Protection. Recommendations of the International Committee on Radiological Protection. ICRP Publication 26. *Ann. ICRP* 1 (3). 1971.

44. Lee C, Lee J-K. Computational Anthropomorphic Phantoms for Radiation Protection Dosimetry: Evolution and Prospects. *Nuclear Engineering and Technology* 2006;38.
45. Lee C, Lodwick D, Bolch WE. NURBS-based 3-D anthropomorphic computational phantoms for radiation dosimetry applications. *Radiat Prot Dosimetry* 2007;127:227-32.
46. Bolch W, Lee C, Wayson M, Johnson P. Hybrid computational phantoms for medical dose reconstruction. *Radiat Environ Biophys* 2010;49:155-68.
47. Li X, Samei E, Segars WP, et al. Patient-specific radiation dose and cancer risk estimation in CT: part I. development and validation of a Monte Carlo program. *Med Phys* 2011;38:397-407.
48. Ghita M. Computer simulations to estimate organ doses from clinically validated cardiac, neuro, and pediatric protocols for multiple detector computed tomography scanners. In. [Gainesville, Fla.]: University of Florida; 2009.
49. Maltz JS, Gangadharan B, Bose S, et al. Algorithm for X-ray scatter, beam-hardening, and beam profile correction in diagnostic (kilovoltage) and treatment (megavoltage) cone beam CT. *IEEE Trans Med Imaging* 2008;27:1791-810.
50. Liu H, Gu J, Caracappa PF, Xu XG. Comparison of two types of adult phantoms in terms of organ doses from diagnostic CT procedures. *Phys Med Biol* 2010;55:1441-51.
51. Lee C, Williams JL, Bolch WE. The UF series of tomographic computational phantoms of pediatric patients. *Med Phys* 2005;32:3537-48.
52. Winslow JF, Hyer DE, Fisher RF, Tien CJ, Hintenlang DE. Construction of anthropomorphic phantoms for use in dosimetry studies. *J Appl Clin Med Phys* 2009;10:2986.
53. Jones AK, Hintenlang DE, Bolch WE. Tissue-equivalent materials for construction of tomographic dosimetry phantoms in pediatric radiology. *Med Phys* 2003;30:2072-81.
54. Chew FS, Relyea-Chew A, Ochoa ER. Postmortem computed tomography of cadavers embalmed for use in teaching gross anatomy. *J Comput Assist Tomogr* 2006;30:949-54.
55. Trapped Charge Dating. 2007. (Accessed May 11, 2011, at [http://rses.anu.edu.au/research/ee/resources/index.php?p=trapped\\_charge.](http://rses.anu.edu.au/research/ee/resources/index.php?p=trapped_charge.))
56. Gorken IB, Kentli S, Alanyali H, Karagüler Z, Kinay M. Evaluation of contralateral breast skin doses by thermoluminescent dosimeters of patients receiving adjuvant radiotherapy for breast cancer. *J BUON* 2002;7:351-4.

57. Ho P, Cheng SW, Wu PM, et al. Ionizing radiation absorption of vascular surgeons during endovascular procedures. *J Vasc Surg* 2007;46:455-9.
58. Horowitz YS, Oster L, Datz H. The thermoluminescence dose-response and other characteristics of the high-temperature TL in LiF:Mg,Ti (TLD-100). *Radiat Prot Dosimetry* 2007;124:191-205.
59. Sulieman A, Theodorou K, Vlychou M, et al. Radiation dose measurement and risk estimation for paediatric patients undergoing micturating cystourethrography. *Br J Radiol* 2007;80:731-7.
60. Knoll GF. *Radiation Detection and Measurement*. Third ed. United States of America: John Wiley & Sons, Inc; 2000.
61. McKeever SWS, Akselrod MS, Colyott LE, Agersnap Larsen N, Polf JC, Whitley V. Characterisation of Al<sub>2</sub>O<sub>3</sub> for Use in Thermally and Optically Stimulated Luminescence Dosimetry. *Radiation Protection Dosimetry* 1999;84:163-6.
62. McKeever SW, Moscovitch M. On the advantages and disadvantages of optically stimulated luminescence dosimetry and thermoluminescence dosimetry. *Radiat Prot Dosimetry* 2003;104:263-70.
63. Magne S, Auger L, Bordy JM, et al. Multichannel dosimeter and Al<sub>2</sub>O<sub>3</sub>:C optically stimulated luminescence fibre sensors for use in radiation therapy: evaluation with electron beams. *Radiat Prot Dosimetry* 2008;131:93-9.
64. Pradhan AS, Lee JI, Kim JL. Recent developments of optically stimulated luminescence materials and techniques for radiation dosimetry and clinical applications. *J Med Phys* 2008;33:85-99.
65. Viamonte A, da Rosa LA, Buckley LA, Cherpak A, Cygler JE. Radiotherapy dosimetry using a commercial OSL system. *Med Phys* 2008;35:1261-6.
66. Yukihiro EG, McKeever SW. Optically stimulated luminescence (OSL) dosimetry in medicine. *Phys Med Biol* 2008;53:R351-79.
67. Yukihiro EG, Ruan C, Gasparian PB, Clouse WJ, Kalavagunta C, Ahmad S. An optically stimulated luminescence system to measure dose profiles in x-ray computed tomography. *Phys Med Biol* 2009;54:6337-52.
68. American National Standards Institute I. *American National Standard for Dosimetry - Personnel Dosimetry Performance - Criteria for Testing*; 2009.
69. Landauer I. *microStar Dosimeter: The Power of the Dot*. In: [http://www.landauer.com/uploadedFiles/Healthcare\\_and\\_Education/Products/Dosimeters/nanoDot%20Spec%20Sheet.pdf](http://www.landauer.com/uploadedFiles/Healthcare_and_Education/Products/Dosimeters/nanoDot%20Spec%20Sheet.pdf). Glenwood, IL; 2008.

70. Landauer I. InLight Complete Dosimetry System Solution: microStar Dosimetry Reader. In: [http://www.landauer.com/uploadedFiles/Healthcare\\_and\\_Education/Products/Readers/1814LAND\\_inLight\\_microStar\\_v5pdf](http://www.landauer.com/uploadedFiles/Healthcare_and_Education/Products/Readers/1814LAND_inLight_microStar_v5pdf). Glenwood, IL; 2010.
71. Griglock T. Comparison of Radiation Dose from Spinal Surgery: Fluoroscopic Guidance versus Intra-Operative Computed Tomography. In: University of Florida; 2009.
72. Lavoie LK. Organ dose measurements from multiple-detector computed tomography using a commercial dosimetry system and tomographic, physical phantoms. In. [Gainesville, Fla.]: University of Florida; 2009.
73. Jursinic PA. Characterization of optically stimulated luminescent dosimeters, OSLDs, for clinical dosimetric measurements. *Med Phys* 2007;34:4594-604.
74. Bellomi M, Viotti S, Preda L, D'Andrea G, Bonello L, Petralia G. Perfusion CT in solid body-tumours. Part II: Clinical applications and future development. *Radiol Med* 2010;115:858-74.
75. Kambadakone AR, Sahani DV. Body perfusion CT: technique, clinical applications, and advances. *Radiol Clin North Am* 2009;47:161-78.
76. Petralia G, Preda L, D'Andrea G, et al. CT perfusion in solid-body tumours. Part I: Technical issues. *Radiol Med* 2010;115:843-57.
77. Spira D, Vogel W, Bares R, Horger M. Volume-perfusion CT as an adjunct to whole-body contrast-enhanced CT for monitoring response to therapy in lymphoma. *Br J Haematol* 2010;151:293.
78. Tognolini A, Schor-Bardach R, Pinykh OS, Wilcox CJ, Raptopoulos V, Goldberg SN. Body tumor CT perfusion protocols: optimization of acquisition scan parameters in a rat tumor model. *Radiology* 2009;251:712-20.
79. American Association of Physicists in Medicine. Size-Specific Dose Estimates (SSDE) in Pediatric and Adult Body CT Examinations. College Park, MD; 2011.

## BIOGRAPHICAL SKETCH

Thomas Griglock was born and raised in West Pittston, Pennsylvania. He performed his undergraduate work at the University of Scranton, where he earned his a Bachelor of Science degree in physics under the guidance of Professor John Kalafut. He received his master's degree in physics from Lehigh University prior to beginning his studies at the University of Florida, where he earned his second master's degree in Nuclear Engineering Sciences. He continued his studies at the University of Florida, eventually earning his Doctor of Philosophy degree in Biomedical Engineering with a concentration in medical physics. He currently lives in Gainesville, FL, with his wife, Angela, their beloved dog, Laurel, and their two insane yet entertaining cats, Finnegan and Sophie.